Excitation Transfer in Highly Excited Calcium Atoms Through Thermal Collisions with Argon

by

Rizwan Ahmad Qureshi

A Thesis Presented to the

FACULTY OF THE COLLEGE OF GRADUATE STUDIES

KING FAHD UNIVERSITY OF PETROLEUM & MINERALS

DHAHRAN, SAUDI ARABIA

In Partial Fulfillment of the
Requirements for the Degree of

MASTER OF SCIENCE

In

PHYSICS

April, 1996

INFORMATION TO USERS

This manuscript has been reproduced from the microfilm master. UMI films the text directly from the original or copy submitted. Thus, some thesis and dissertation copies are in typewriter face, while others may be from any type of computer printer.

The quality of this reproduction is dependent upon the quality of the copy submitted. Broken or indistinct print, colored or poor quality illustrations and photographs, print bleedthrough, substandard margins, and improper alignment can adversely affect reproduction.

In the unlikely event that the author did not send UMI a complete manuscript and there are missing pages, these will be noted. Also, if unauthorized copyright material had to be removed, a note will indicate the deletion.

Oversize materials (e.g., maps, drawings, charts) are reproduced by sectioning the original, beginning at the upper left-hand corner and continuing from left to right in equal sections with small overlaps. Each original is also photographed in one exposure and is included in reduced form at the back of the book.

Photographs included in the original manuscript have been reproduced xerographically in this copy. Higher quality 6" x 9" black and white photographic prints are available for any photographs or illustrations appearing in this copy for an additional charge. Contact UMI directly to order.

UMI

A Bell & Howell Information Company
300 North Zeeb Road, Ann Arbor MI 48106-1346 USA
313/761-4700 800/521-0600

EXCITATION TRANSFER IN HIGHLY EXCITED CALCIUM ATOMS THROUGH THERMAL COLLISIONS WITH ARGON

BY

Rizwan Ahmad Qureshi

A Thesis Presented to the

FACULTY OF THE COLLEGE OF GRADUATE STUDIES

KING FAHD UNIVERSITY OF PETROLEUM & MINERALS

DHAHRAN, SAUDI ARABIA

In Partial Fulfillment of the
Requirements for the Degree of

MASTER OF SCIENCE

In

PHYSICS

April, 1996

EXCITATION TRANSFER IN HIGHLY EXCITED CALCIUM ATOMS THROUGH THERMAL COLLISIONS WITH ARGON

Rizwan Ahmad Qureshi

PHYSICS

April, 1996

KING FAHD UNIVERSITY OF PETROLEUM AND MINERALS
DHAHRAN 31261, SAUDI ARABIA

COLLEGE OF GRADUATE STUDIES

This thesis, written by Rizwan Ahmad Qureshi under the direction of his Thesis Advisor and approved by his Thesis Committee, has been presented to and accepted by the Dean of the College of Graduate Studies, in partial fulfillment of the requirements for the degree of MASTER OF SCIENCE in PHYSICS.

Thesis Committee:

Dr. M. Aslam Khan
Chairman of the Thesis Committee

Dr. F. Al-Adel
Co-Chairman of the Thesis Committee

Dr M. A. Gondal
Member

Dr. H. A. Mavromatis
Member

Dr. M. Rafique
Member

Department Chairman

Dean, College of Graduate Studies

4/6/96
Date

COLLEGE OF GRADUATE STUDIES

DEDICATED TO MY
LATE MOTHER

"MY LORD! BESTOW ON THEM YOUR
MERCY AS THEY DID BRING ME UP WHEN I
WAS SMALL."

Contents

List of Figures vii

List of Tables xv

Acknowledgement xvii

Abstract (English) xviii

Abstract (Arabic) xix

1 Introduction 1

1.1 Possible Atomic Processes 4

1.1.1 Two-Step Resonant Laser Excitation of Atoms 4

1.1.2 Superelastic Heating of Electrons 5

1.1.3 Collisional Excitation and Ionization of Atoms by Superelastically Heated Electrons 5

1.1.4 Energy Pooling Collisions between Excited Atoms 6

1.1.5 Associative Ionization 6

1.1.6 Spontaneous Radiative Emission and Reabsorption of Emitted Radiation 7

1.1.7 "Thermal" Collisions with Ar Atoms 7

1.1.8 Recombination of a Free Electron with Ions 8

1.2 Singlets, Triplets and Doubly-Excited States 8

1.3 Organization of the Thesis 9

2 Theoretical Background **11**

2.1 Introduction 11

2.2 Photon Absorption and Emission 12

2.3 Physics of Collisions 14

2.3.1 Kinetic Collisions and Optical Collisions 15

2.3.2 Electron Collisions with Atoms 18

2.3.3 Excitation Exchange and Quenching 19

2.3.4 Scattering and Deactivation of Metastables 21

2.3.5 Electron and Photon Collisions with Metastables 22

2.3.6 Collision Cross-sections and Rate Coefficients 22

2.4 A Simple Kinetic Model for Calculating Rate Constants 25

3 Experimental setup and Experimental Procedures **31**

3.1 The Laser Systems 31

3.1.1 Nd:YAG Laser DCR 2A(20) 32

3.1.2 Dye Laser (PDL-2) 39

3.1.3 XeCl Excimer Laser (Lambda Physik EMG 203 MSC) 44

3.1.4 Synchronization of the Laser Pulses 53

3.2 The Heat Pipe Oven 55

3.3 Data Acquisition and Data Processing System 56

3.4 The Monochromator and Photomultiplier 59

3.5 Experimental Procedure 59

4 Experimental Results 62

4.1 Introduction 62

4.2 Energy Transfer Through Collisions 63

4.3 A Broad Overview of Strong Collision Channels 65

4.4 Time-Resolved Kinetics 69

4.4.1 Parent State $3d4p\ ^1D_2$ 69

4.4.2 Parent State $3d4p\ ^3F_2$ 69

4.4.3 Parent State $3d4p\ ^3D_1$ 72

4.5 Wavelength-Resolved Spectra 75

4.5.1 Parent State $3d4p\ ^1D_2$ 81

4.5.2 Parent State $3d4p\ ^3F_4$ 88

4.5.3 Parent State $3d4p\ ^3F_2$ 88

4.5.4 Parent State $4s5p\ ^3P_2$ 95

4.5.5 Parent State $3d4p\ ^3D_1$ 102

4.6 State-to-state rate constant 107

5 Computer Model Calculations & Comparison with Experimental Results 116

5.1 Introduction 116

5.2 The Computer Code 117

5.3 The Rate Equations 123

5.3.1 Instantaneous Population Densities of Excited States 123

5.3.2 Electron Density 125

5.3.3 Electron Energy 125

5.3.4 Normalization 126

5.3.5 The Actual Rates Used 126

5.4 Line Intensities 127

5.5 Results on the Population Densities 133

5.5.1 Parent State 3d4p $^1D_2$ 133

5.5.2 Parent State 3d4p ^3F 133

5.5.3 Parent State 4s5p ^3P 134

5.5.4 Parent State 3d4p ^3D 134

5.6 Results on Line Intensity Ratios and Calculation of Rate Constants . 139

5.6.1 Parent State 3d4p $^1D_2$ 139

5.6.2 Parent State 4s5p ^3P 142

5.6.3 Parent State 3d4p ^3F 144

5.6.4 Parent State 3d4p ^3D 146

6 Conclusion and Discussions 148

6.1 Some Suggestions for Future Work 150

Bibliography 151

List of Figures

1.1 The energy-level diagram of Ca. 10

2.1 Schematic representation of (a) Kinetic collision and (b) optical collision. 17

2.2 Partial energy level diagram for the calcium atom showing the laser-excited parent state 3d4p $^1D_2$, the predominant product states (4s5p $^3P_1$, 3d4p $^3F_2$, 4s5p $^1P_1$) populated by collisions with Argon, and fluorescent transitions observed. 26

3.1 Simplified energy levels of Nd:YAG 34

3.2 Nd:YAG laser system showing the optical schematic. 36

3.3 Flashlamp and Q-switch timing schematic. 37

3.4 The internal timing sequence of the built in master oscillator. 40

3.5 Schematic of Quanta-Ray PDL-2 pulsed dye laser. 42

3.6 Typical energy levels for a dye in solution. The singlet and triplet levels are shown in separate columns. 43

3.7 PDL-2 Oscillator Design 44

3.8 Schematic potential energy diagram illustrating the electronic structure of the rare rare gas monohalides (XeCl). 46

3.9 Block diagram of the Excimer Laser. 50

3.10 Schematic of the FL 2002 with the pump-beam path. 51

3.11 Typical tuning curves for the dyes used in this experiment. 52

3.12 Delay between the pulses from the two lasers. 54

3.13 Schematic diagram of the heatpipe oven. 55

3.14 The heat pipe oven together with its peripheral devices. 57

3.15 Schematic diagram of the experimental setup. 60

4.1 A simplified energy level diagram for calcium, showing the laser prepared states together with the levels populated by collision and important radiative pathways. 64

4.2 Relative intensities emitted from the upper states of the fluorescing transitions when different parent states were prepared by the second laser as indicated in the legend. 68

4.3 Time resolved fluorescence traces of the 3d4p $^1D_2 \rightarrow$ 4s3d $^1D_2$ transition at 7148 Å, with 70 mbar Ar pressure. 70

4.4 Deactivation plot for the transition 3d4p $^1D_2 \rightarrow$ 4s3d $^1D_2$ at 7148 Å. 71

4.5 Deactivation plot for the transition 3d4p $^3F_2 \rightarrow$ 4s3d $^1D_2$ at 7202 Å. . 73

4.6 Deactivation plot for the transition 3d4p $^3D_1 \rightarrow$ 4s3d $^3D_1$ at 5598 Å. 74

4.7 A typical spectrum of the 3d4p $^3F_2 \rightarrow$ 4s3d $^1D_2$ transition of Ca I at 7202Å. 77

4.8 Fluorescent spectrum in the 6436 to 6487.34Å region when the $4s5p$ $^3P_2$ state was prepared by step-wise excitation. Here the Ar pressure was 10 mbar. 78

4.9 Fluorescent spectrum in the 6436 to 6487.34Å region when the $4s5p$ $^3P_2$ state was prepared by step-wise excitation. Here the Ar pressure was 20 mbar. 79

4.10 Fluorescent spectrum in the 6436 to 6487.34Å region when the $4s5p$ $^3P_2$ state was prepared by step-wise excitation. Here the Ar pressure was 40 mbar. 80

4.11 Partial energy level diagram for the calcium atom showing the laser - excited 3d4p $^1D_2$ state, the predominant product states (4s5p $^3P_1$, 3d4p $^3F_2$, 4s5p $^1P_1$) populated by collisions with Argon, and fluorescent transitions observed. 83

4.12 Fluorescence yield from the 4s5p $^1P_1 \rightarrow$ 4s3d $^1D_2$ at 6717 Å at different Argon densities, when the 3d4p $^1D_2$ state of calcium was prepared with the help of the step-wise laser excitation process. 84

4.13 Fluorescence yield from the 3d4p $^3F_2 \rightarrow$ 4s3d $^1D_2$ at 7202 Å at different Argon densities, when the 3d4p $^1D_2$ state of calcium was prepared with the help of the step-wise laser excitation process. 85

4.14 Fluorescence yield from the 4s5p $^3P_2 \rightarrow$ 4s3d $^3D_2$ at 6169 Å at different Argon densities, when the 3d4p $^1D_2$ state of calcium was prepared with the help of the step-wise laser excitation process. 86

4.15 Fluorescence yield from the 3d4p $^1D_2 \rightarrow$ 4s3d $^1D_2$ at 7148 Å at different Argon densities, when the 3d4p $^1D_2$ state of calcium was prepared with the help of the step-wise laser excitation process. 87

4.16 Partial energy level diagram for the calcium atom showing the laser - excited 3d4p $^3F_4$ state, the predominant product states (4s5p $^3P_1$, 3d4p $^1D_2$, 4s5p $^1P_1$) populated by collisions with Argon, and fluorescent transitions observed. 89

4.17 Fluorescence yield from the 3d4p $^3F_2 \rightarrow$ 4s3d $^1D_2$ at 7202 Å at different Argon densities, when the 3d4p $^3F_4$ state of calcium was prepared with the help of the step-wise laser excitation process. 90

4.18 Fluorescence yield from the 4s5p $^1P_1 \rightarrow$ 4s3d$^1D_2$ at 6717 Å at different Argon densities, when the 3d4p $^3F_4$ state of calcium was prepared with the help of the step-wise laser excitation process. 91

4.19 Fluorescence yield from the 3d4p $^1D_2 \rightarrow$ 4s3d $^1D_2$ at 7148 Å at different Argon densities, when the 3d4p $^3F_4$ state of calcium was prepared with the help of the step-wise laser excitation process. 92

4.20 Fluorescence yield from the 3d4p $^1D_2 \rightarrow$ 4s3d $^1D_2$ at 7148 Å at different Argon densities, when the 3d4p $^3F_2$ state of calcium was prepared with the help of the step-wise laser excitation process. 93

4.21 Fluorescence yield from the 3d4p $^3F_2 \rightarrow$ 4s3d $^1D_2$ at 7202 Å at different Argon densities, when the 3d4p $^3F_2$ state of calcium was prepared with the help of the step-wise laser excitation process. 94

4.22 Partial energy level diagram for the calcium atom showing the laser - excited 4s5p $^3P_2$ state, the predominant product states (3d4p $^1D_2$, 3d4p $^3F_2$, 4s5p $^1P_1$) populated by collisions with Argon, and fluorescent transitions observed. 96

4.23 Fluorescence yield from the 3d4p $^1D_2 \rightarrow$ 4s3d $^1D_2$ at 7148 Å at different Argon densities, when the 4s5p $^3P_2$ state of calcium was prepared with the help of the step-wise laser excitation process. 97

4.24 Fluorescence yield from the 3d4p $^3F_2 \rightarrow$ 4s3d $^1D_2$ at 7202 Å at different Argon densities, when the 4s5p $^3P_2$ state of calcium was prepared with the help of the step-wise laser excitation process. 98

4.25 Fluorescence yield from the 4s5p $^1P_1 \rightarrow$ 4s3d$^1D_2$ at 6717 Å at different Argon densities, when the 4s5p $^3P_2$ state of calcium was prepared with the help of the step-wise laser excitation process. 99

4.26 Fluorescence yield from the 4s4d $^3D_3 \rightarrow$ 4s4p $^3P_2$ at 4454 Å at different Argon densities, when the 4s5p $^3P_2$ state of calcium was prepared with the help of the step-wise laser excitation process. 100

4.27 Fluorescence yield from the 3d4p $^1D_2 \rightarrow$ 4s3d $^3D_1$ at 6449 Å at different Argon densities, when the 4s5p $^3P_2$ state of calcium was prepared with the help of the step-wise laser excitation process. 101

4.28 Partial nergy level diagram for the calcium atom showing the laser - excited 3d4p $^3D_1$ state, the predominant product states (4s4d $^3D_3$, 3d4p $^3P_2$, 4p^2 $^3P_2$) populated by collisions with Argon, and fluorescent transitions observed. 103

4.29 Fluorescence yield from the 3d4p $^3P_2 \rightarrow$ 4s3d $^3D_3$ at 5270 Å at different Argon densities, when the 3d4p $^3D_1$ state of calcium was prepared with the help of the step-wise laser excitation process. 104

4.30 Fluorescence yield from the 4s4d $^3D_3 \rightarrow$ 4s4p $^3P_2$ at 4454 Å at different Argon densities, when the 3d4p $^3D_1$ state of calcium was prepared with the help of the step-wise laser excitation process. 105

4.31 Fluorescence yield from the 4p^2 $^3P_2 \rightarrow$ 4s4p $^3P_2$ at 4302 Å at different Argon densities, when the 3d4p $^3D_1$ state of calcium was prepared with the help of the step-wise laser excitation process. 106

4.32 A plot of the state-to-state rate constant for energy transfer from 3d4p $^1D_2 \rightarrow$ 3d4p$^3F_2$ as a function of the Argon pressure. The line is a weighted least-squares fits to the data, the intercept is taken to be the state-to-state rate constant. 110

4.33 A plot of the state-to-state rate constant for energy transfer from 3d4p $^1D_2 \rightarrow$ 4s5p $^1P_1$ as a function of the Argon pressure. The line is a weighted least-squares fits to the data, the intercept is taken to be the state-to-state rate constant. 111

4.34 A plot of the state-to-state rate constant for energy transfer from 3d4p $^1D_2 \rightarrow$ 4s5p $^3P_2$ as a function of the Argon pressure. The line is a weighted least-squares fits to the data, the intercept is taken to be the state-to-state rate constant. 112

4.35 A plot of the state-to-state rate constant for energy transfer from 3d4p $^3F_2 \rightarrow$ 3d4p $^1D_2$ as a function of the Argon pressure. The line is a weighted least-squares fits to the data, the intercept is taken to be the state-to-state rate constant. 113

5.1 Variation of population density of selected states of Ca with time. . . 130

5.2 Variation of electron temperature with time. 131

5.3 Variation of electron density with time. 132

5.4 Variation of population density of some selected states (see the legend) of Ca with time. Here the parent state is the 3d4p $^1D_2$ state of Ca. . 135

5.5 Variation of population density of some selected states of Ca with time. Here the parent state is the 3d4p ^3F state of Ca. 136

5.6 Variation of population density of some selected states of Ca with time. Here the parent state is the 4s5p ^3P state of Ca. 137

5.7 Variation of population density of some selected states of Ca with time. Here the parent state is the 3d4p ^3D state of Ca. 138

5.8 Computed line intensities of two transitions as obtained by the computer model. Parent state is 3d4p $^1D_2$. 140

5.9 Computed line intensity of the transition as obtained by the computer model. Parent state is 3d4p $^1D_2$. 141

5.10 The computed line intensities of various transitions as obtained by the computer model. Parent state is the 4s5p ^3P state of Ca. 143

5.11 The computed line intensities of various transitions as obtained by the computer model. Parent state is the 3d4p ^{3}F state of Ca. 145

5.12 The computed line intensities of various transitions as obtained by the computer model. Parent state is the 3d4p ^{3}D state of Ca. 147

List of Tables

3.1 Specifications of the dyes used in the experiment. For the above dyes methanol is used as the solvent. 52

4.1 Energy defect (cm^{-1}) between the parent and the product state. . . . 65

4.2 Intensities (arbitrary units) of various transitions observed when different parent states were prepared. 67

4.3 Total quenching rates for the parent states.(see text for further explanation) 72

4.4 The actual transitions corresponding to different lines in Figures 4.8 to 4.10. 76

4.5 Atomic data for the observed transitions for rate constant measurements. 107

4.6 The forward rate constant for the parent state 3d4p $^3F_2$ induced by Ar collisions. 108

4.7 The forward rate constant for the parent state 3d4p $^1D_2$ induced by Ar collisions. 109

4.8 The forward rate constant for the parent state 4s5p $^3P_2$ induced by Ar collisions. * Rate constant calculated via detailed balance using results of Hale and Leone (see text). 115

5.1 The states alongwith their energies and statistical weights 120

5.2 Comparison of line intensity ratios obtained experimentally with those calculated by using the computer model. Parent state is the 3d4p $^1D_2$ state of Ca. Q is the multiplicative factor with k_{1j}. 139

5.3 Comparison of line intensity ratios obtained experimentally with those calculated by using the computer model. Parent state is the 4s5p ^3P state of Ca. Q is the multiplicative factor with k_{1j}. *Rate constant calculated via detailed balance using results of Hale and Leone (see Chap 4). 142

5.4 Comparison of line intensity ratios obtained experimentally with those calculated by using the computer model. Parent state is the 3d4p ^3F state of Ca. Q is the multiplicative factor with k_{1j}. 144

5.5 Comparison of line intensity ratios obtained experimentally with those calculated by using the computer model. Parent state is the 3d4p ^3D state of Ca. Q is the multiplicative factor with k_{1j}. 146

Acknowledgement

Thanks to ALLAH for giving me the opportunity and health to conduct this work. Acknowledgement is due to King Fahd University of petroleum and Minerals for support of this research.

In particular, I would like to thank the Physics Department and the Laser Research Laboratory for making all their facilities available to me.

I would like to express my deep appreciation to my thesis advisor, Dr. Mohammad Aslam Khan for his patient guidance and his generous support for this research.

I would like to express my gratefulness to the Co-chairman of the Comittee Dr. Fida Al-Adel, and the other committee members Dr. M. A. Gondal, Dr. H. A. Mavromatis and Dr. M. Rafique for their valuable suggestions.

Special thanks are to Mr. Hamid Rais of the Laser Atomic Spectroscopy group whose valuable assistance is appreciated.

ABSTRACT

NAME: Rizwan Ahmad Qureshi

TITLE: EXCITATION TRANSFER IN HIGHLY EXCITED CALCIUM ATOMS THROUGH THERMAL COLLISIONS WITH ARGON

MAJOR: PHYSICS

DATE: April, 1996.

Energy transfer between 4p3d (^{1}D, ^{3}P, ^{3}F, ^{3}D), 4s5p ^{3}P, 4s4d ^{3}D and 4p^2 ^{3}P states of Ca was investigated following a two-step selective excitation of specific atomic states using pulsed lasers. Transfer of population to nearby states was monitored as a function of Ar pressure through a systematic study of fluorescence. The main channels of decay were identified and information on the rate constants for Ca-Ar collisions was obtained. The experimental results together with a computer model developed to simulate the experiment is presented.

MASTER OF SCIENCE DEGREE

KING FAHD UNIVERSITY OF PETROLEUM AND MINERALS

DHAHRAN, SAUDI ARABIA

April, 1996

ABSTRACT (Arabic)

خلاصة الرسالة

اسم الطالب الكامل رضوان أحمد قريشي

عنوان الدراسة إنتقال الطاقة في ذرات الكالسيوم عاليةالاثارة من خلال التصادم الحراري مع ذرات غاز الأرجون

التخصص فيزياء

تاريخ الشهادة ابريل ١٩٩٦م

لقد تم دراسة انتقال الطاقة بين مستويات الكالسيوم :

$4p3d(^1D,^3P,^3F,^3D),4s5p^3P,4s4d^3D$ and $4p^2\ ^3P$

المنتقاة بعد اثارة ثنائية التدرج باستخدام الليزر النبضي. ولقد تم مراقبة تغير انتقال التجمعات الذرية الى المستويات القريبة مع تغير ضغط غاز الأرجون، وذلك من خلال الدراسة المنظم للانبعاثات لهذه المستويات.

كما تم التعرف على القنوات الرئيسية لفقدان قوة الانبعاث والحصول على معلومات عن معدل ثوابت التصادمات لذرات الأرجون والكالسيوم. وتعرض هذه الأطروحة النتائج التجريبية مع نموذج حسابي مطور ليماثل النموذج التجريبي.

درجة الماجستير في العلوم

جامعة الملك فهد للبترول و المعادن

الظهران ، المملكة العربية السعودية

ابريل ١٩٩٦م

Chapter 1

Introduction

Tunable lasers provide the most efficient method for creating large populations of atoms in specific excited states through resonant pumping. For reaching highly excited states, step-wise resonant excitation using two or more different wavelengths may be used.

An atom in an excited state de-excites through spontaneous decay and through collisional 'quenching' [1] or it can be further excited and ionized through absorption of additional energy, e.g. in collisions with other excited atoms or energetic electrons. However, in the context of the present studies, the interacting particles are not accelerated as in conventional accelerators or any other auxiliary fields, and are essentially considered thermal since they do not have directed motion. The basic processes involved can be characterized by analyzing the emitted radiation or through measurements on the electrons or ions produced as a result of ionizing events [2, 3, 4, 5, 6, 7, 8].

The rate of collisional ionization of a particular excited state depends on several

physical parameters such as binding energy of the state, the local conditions such as the temperature and density which control the probabilities of various collisional energy transfer mechanisms; as well as the radiative lifetime which may permit the upward collisional processes to meaningfully compete or, in some cases, to even surpass the downward radiative decay. Similarly, transfer to nearby states is controlled by the density and the nature of the collision partners and the energy gap between the states. These processes can also compete with others under some conditions.

The problem of collisional energy transfer is very important particularly in the design and development of new laser sources [9, 10, 11]. For example, it may be a loss mechanism for the energy deposited in the system which needs to be controlled. On the other hand, it may be fruitfully exploited in the indirect but efficient pumping of some otherwise inaccessible states where direct transitions are forbidden by the selection rules of quantum mechanics, and where population inversions as well as laser action may be excited. Furthermore, fluorescence lifetimes of some optically inaccessible states can be measured [12]. This is in addition to the purely academic interest in the physics of collisions.

Energy transfer through collisions has been investigated in varying detail in numerous previous publications [13, 14, 15, 16]. However, for highly excited atomic states, only some isolated reports exist even though the availability of tunable lasers in recent years has enabled us to prepare large populations of highly excited atoms in specific atomic states. For example, in the particular case of Ca, while many reports of energy transfer in lower excited states have been published [17, 18, 19, 20, 21], there are only two previous papers [22, 23] on higher excited states where only one state the

4s5p ^{1}P state [22] or 4s5s $^1S_0$ [23] was prepared in a two-photon nonlinear excitation. However, the same group reported studies involving a similar state in strontium [24], and more recently, two papers on barium [20, 21] have been published.

We have investigated five different levels of Ca viz 4s5s ^{3}S, 4s5p ^{3}P, 3d4p ^{3}D, 3d4p ^{1}D and 3d4p ^{3}F prepared through step-wise resonant laser excitations where the efficiency is much higher. Furthermore, we would like to compare the probability of further excitation (and ionization) through energy pooling collisions and other inelastic collisions where large scale energy transfer is involved, with the transfer to nearby states where the energy transfer is limited to the thermal energies of the colliding particles.

Our interest in this work began when Khan et al. [6] reported the excitation of 4p $^2P_{3/2,1/2}$ states of Ca II (singly ionized calcium atom) following resonant pumping of the 4s4p $^3P_1$ metastable state of Ca I (neutral calcium). In a subsequent paper Khan et al. [7] reported that some selected intermediate states of Ca I have a significant influence on the collisional excitation of the 4p $^2P_{3/2,1/2}$ states of Ca II. In particular, the 3d4p $^1D_2$ state had the strongest influence. Here up to fifteen times enhancement in the intensity of fluorescence from the 4p ^{2}P states was observed, when the 3d4p $^1D_2$ state was selectively prepared by a second laser. However, for the 3d4p ^{3}F states which are very close to 3d4p $^1D_2$, the effect was much less pronounced (only a factor of two increase or less). One of the objectives of the present study was to explain this discrepancy. We are particularly interested in the transfer of population between the laser-prepared state and other nearby states. It is obvious that the presence of Argon (buffer gas) could easily mix the populations through thermal collisions.

We used a simple kinetic model to obtain the rates of population transfer from the information on fluorescence. A detailed computer model previously developed by Khan et al. [25] for studying population inversions in laser-pumped Ca vapor was modified to simulate the experiments presented in this thesis. Subsequently the rate constants obtained from the simple Kinetic model were cross-checked with the help of this more detailed computer model. However, before entering into the details of the work carried out in this thesis, it is appropriate to introduce the basic atomic processes involved.

1.1 Possible Atomic Processes

Several collisional and radiative processes occur in a laser pumped vapor as described below in the context of Ca vapor excited in a step-wise manner.

1.1.1 Two-Step Resonant Laser Excitation of Atoms

When the laser is tuned to the specific energy $h\nu_1$ where h is the Planck's constant and ν_1 is the frequency which corresponds to an atomic resonance, the atom is resonantly excited i.e.

$$A(4s^2) + h\nu_1 \longrightarrow A^* \tag{1.1}$$

where $A(4s^2)$ represents a ground state Ca atom and A^* represents an excited Ca atom.

The second step involves exciting A^* to a higher level A^{**}.

$$A^* + h\nu_2 \longrightarrow A^{**} \tag{1.2}$$

where ν_2 is the appropriate resonant frequency.

1.1.2 Superelastic Heating of Electrons

Some electrons can be generated by various processes like multiphoton ionization, associative ionization, Penning ionization occurring in the laser-pumped vapor, or through simple thermionic emission. These electrons can gain energy in superelastic collisions with laser excited atoms, i.e.

$$A^* + e \longrightarrow A + e^* \tag{1.3}$$

$$A^{**} + e \longrightarrow A^* + e^* \tag{1.4}$$

$$A^* + e^* \longrightarrow A + e^{**} \tag{1.5}$$

$$A^{**} + e \longrightarrow A + e^{**} \tag{1.6}$$

where e, e^* and e^{**} represent electrons with kinetic energy of zero, $h\nu_1$ or $h\nu_2$, and $h(\nu_1 + \nu_2)$ respectively above the thermal energy. It should be noted that in these processes (1.3,1.5,1.6) 100% transfer of the energy between the excited atom and the electron is assumed to take place. However, we may also have a part of the energy transferred provided that discrete atomic levels are considered (process 1.4).

1.1.3 Collisional Excitation and Ionization of Atoms by Superelastically Heated Electrons

The laser-excited atoms could be further excited to higher energy states or they could even be ionized [26, 27, 28, 29, 30, 31] through collisions with superelastically heated

electrons discussed in 1.1.2 above. Thus

$$A^* + e^* \longrightarrow A^{**} + e \tag{1.7}$$

$$A^{**} + e^* \longrightarrow A^+ + e + e \tag{1.8}$$

$$A^* + e^{**} \longrightarrow A^+ + e + e \tag{1.9}$$

Where A^+ represents an ion and A** is an atom in a higher excited state.

1.1.4 Energy Pooling Collisions between Excited Atoms

Excited atoms can collide and pool their energies through the processes given below [32].

$$A^* + A^* \longrightarrow A^{**} + A \tag{1.10}$$

$$A^{**} + A^* \longrightarrow A^+ + A + e \tag{1.11}$$

$$A^{**} + A^{**} \longrightarrow A^+ + A^* + e \tag{1.12}$$

1.1.5 Associative Ionization

Excited atoms upon collision could form a molecule which readily ionizes to form a molecular ion $(A_2)^+$ and an electron i.e.

$$A^* + A^* \longrightarrow (A_2)^+ + e \tag{1.13}$$

Collision between a ground state atom and a highly excited atom can also give an ionized molecule

$$A^{**} + A \longrightarrow (A_2)^+ + e \tag{1.14}$$

1.1.6 Spontaneous Radiative Emission and Reabsorption of Emitted Radiation

An excited atom could return to a lower state or the ground state by emission of frequency ν' or ν'' which may be different from ν_1 or ν_2, i.e.

$$A^* \longrightarrow A + h\nu' \tag{1.15}$$

$$A^{**} \longrightarrow A^* + h\nu'' \tag{1.16}$$

These photons could be reabsorbed by another excited or unexcited atom. For example, a highly excited atom could be ionized. Thus,

$$h\nu' + A^{**} \longrightarrow A^+ + e \tag{1.17}$$

1.1.7 "Thermal" Collisions with Ar Atoms

In our experiments we used Ar as a buffer gas. Excited atoms could be transferred to nearby states in thermal collisions with Ar atoms (X).

$$A^{**} + X \longrightarrow A^* + X \pm \Delta E \tag{1.18}$$

where ΔE is the energy defect. The maximum energy defect will be limited over here to the total thermal energies of collision partners. Ar is an inert gas and its first excited state is at 11.49 eV above its ground state, which is too high for the present experiments. Therefore the only exchange of energy is through thermal collisions.

1.1.8 Recombination of a Free Electron with Ions

A free electron can recombine with an ion forming a neutral atom with the emission of a photon

$$A^+ + e \longrightarrow A^{**} + h\nu \ (Radiative\ Recombination) \tag{1.19}$$

Another possibility lies in the fact that no photon is emitted but rather the excess energy is carried by another electron i. e.

$$A^+ + e + e \longrightarrow A^{**} + e^* \ (Three-body\ Recombination) \tag{1.20}$$

A** can be an atom in one of the excited states or even the ground state.

1.2 Singlets, Triplets and Doubly-Excited States

The Ca atom belongs to the Group IIA of the Periodic Table, which have two valence electrons outside an inert core. The spins of the two valence electrons can be anti-parallel ($S = 0$) or parallel ($S = 1$). Consequently, the case $S = 0$ will lead to Singlet states and $S = 1$ to Triplet states. However, we can also have some compound states where both of the valence electrons are in excited states. These will be the so called "doubly excited states". We shall be dealing with all these three categories in our work presented here. We shall be using the state designations corresponding to the $L - S$ or the Russel-Saunders coupling scheme. Accordingly $^{2S+1}X_J$ will describe a term of total angular momentum J with X indicating the total orbital angular momentum according to the convention: If $L = 0, 1, 2, 3, 4, 5.....$ then $X = S, P, D, F, G, H.....$. Figure 1.1 shows the energy level diagram for Ca where the singlet, triplet and doubly

excited states (complex/displaced terms) are indicated in separate groups [33]. The doubly excited states located above the first ionization limit are the autoionizing states [34].

1.3 Organization of the Thesis

The work presented in this thesis is arranged as follows.

Chapter 2 deals with the theoretical background particularly the physics of collisions. A kinetic model for extracting information on rate coefficients of the collision processes of interest is also presented in this chapter. The details of the experimental set-up and the experimental procedures used are described in chapter 3. Experimental results are presented in chapter 4. Information on the rate constants obtained with the help of the simple kinetic model of chapter 2, is also presented in chapter 4. In chapter 5 we present the detailed computer model. The results obtained with this computer model are compared with the results from chapter 4. The conclusions are presented in chapter 6 where some suggestions for further work are also listed.

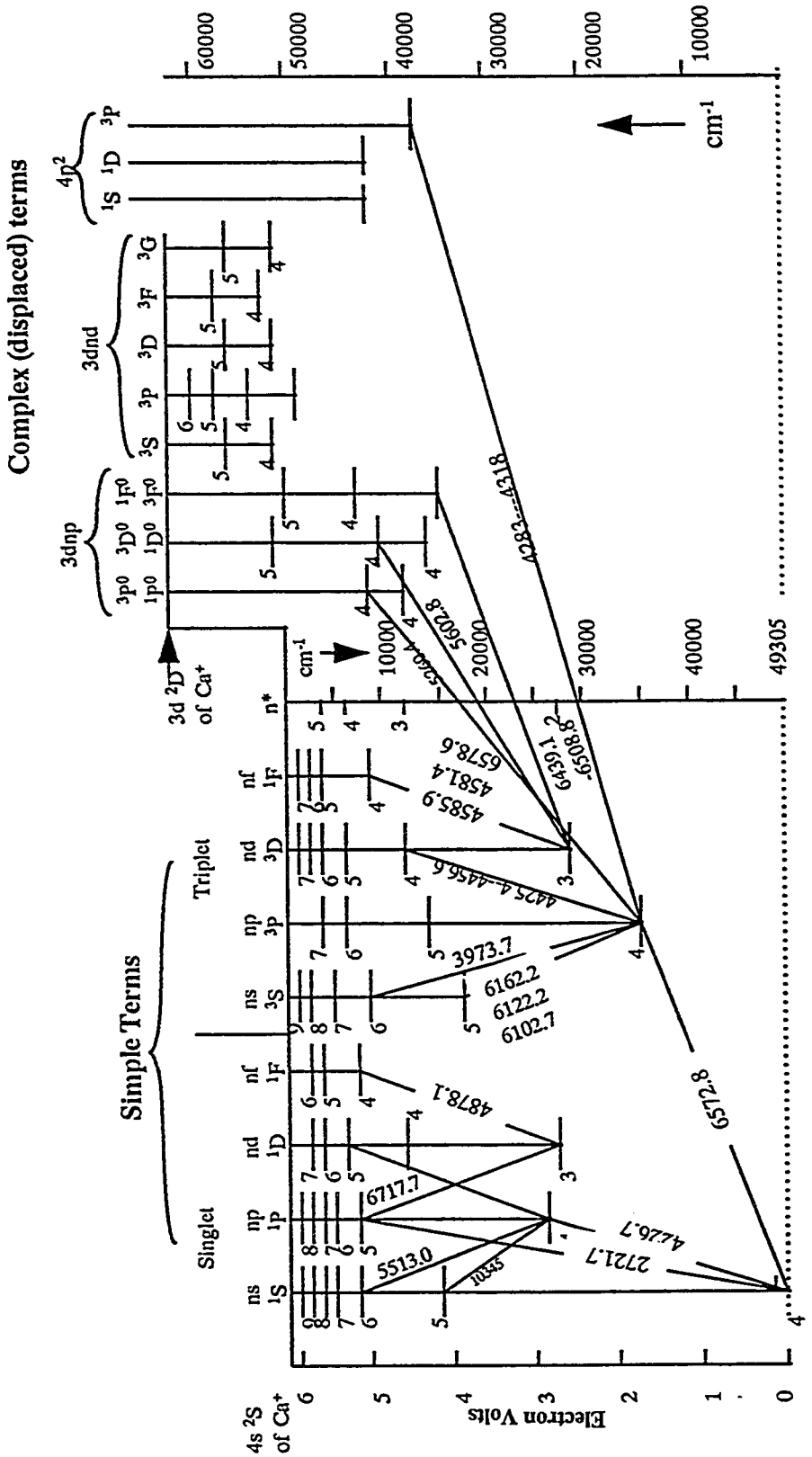

Figure 1.1: The energy-level diagram of Ca.

Chapter 2

Theoretical Background

2.1 Introduction

State-changing collisions between excited metal atoms and rare gases continue to provide insight into the dynamics of atomic collisions [13, 14, 15, 16, 22, 23, 35, 36, 37, 38]. Due to the lack of quantitative information on potential curves, a complete understanding is usually hampered. The specificity of the population transfer suggests that some systems may be worthy of extended experimental and theoretical study. A significant amount of work has already been done in the case of alkaline earth metals, a two-electron system, which possess a challenging degree of complexity in their atomic structure [39, 40, 41, 42]. The quantitative knowledge of these deactivating collisional transfer (rate constants) can provide us with some useful information for the identification of the main decay channels of a particular state, i.e. the states to which maximum collisional energy transfer takes place relative to other nearby states. Hence new techniques may be developed for the indirect pumping of states which are

otherwise inaccessible i.e. where direct transitions are forbidden by the selection rules of quantum mechanics.

2.2 Photon Absorption and Emission

The interaction of an electromagnetic wave with an atomic system is to a first approximation the interaction with the electric dipole moment.

The energy intensity $\Im_\nu$ (watts) of a spectral line spontaneously emitted in all directions from a unit volume of gas at a frequency $\nu_{nm} = E_{nm}/h$ corresponding to the downward transition from level n to level m is given by

$$\Im = n_n h \nu_{nm} A_{nm} \tag{2.1}$$

where the emitted energy $E_{nm} = E_n - E_m$, and n_n and n_m are the densities of atoms in states n and m. Note that ν is here expressed as a frequency and not a wavenumber; A_{nm} is the Einstein A coefficient, or transition probability of spontaneous transition by one atom in one second [43]. A typical value of A_{nm} for an electric dipole transition is 10^8 sec^{-1}. A number N_{0n} of atoms in state n decays (in the absence of collisions) according to the equation

$$N_n(t) = N_{0n} \exp\left(-\frac{t}{\tau}\right) \tag{2.2}$$

with

$$\tau = \sum_m \tau_{nm} = \sum_m A_{nm}^{-1} \tag{2.3}$$

The width of the spectral line is denoted by Γ, and the lifetime

$$\tau = \frac{h}{\Gamma} \tag{2.4}$$

Thus broad lines correspond to short lifetimes [44].

A typical lifetime τ_{nm} for an excited state decaying by a single quantum electric dipole transition is $\sim 10^{-8}$ sec [45, 46, 47], but metastable states have long lifetimes, e.g. $\sim 10^{-3}$ sec (magnetic dipole) and ~ 1 sec (electric quadrupole). Lifetimes may be shortened by the application of electric fields [48] or through collisions.

For a parallel beam of light of constant intensity between frequencies ν and $\nu + d\nu$ (e.g.; laser light of finite line width in our case), the absorption in a path dx through gas containing densities of excited atoms n_n and n_m is

$$d\left(\Im_\nu d\nu\right) = \Im_\nu h\nu_{nm} dx \left(n_m B_{mn} - n_n B_{nm}\right) \tag{2.5}$$

where $\Im_\nu$ is the intensity of the equivalent isotropic radiation for which the Einstein B coefficients are defined. The product $B_{mn}\Im_\nu$ is the probability of an upward transition $m \rightarrow n$ per second per atom exposed to radiation of intensity $\Im_\nu$. This is the transition probability of absorption. B_{nm} is related to A_{nm} and depends on the atom. The product $B_{nm}\Im_\nu$ is the probability of stimulated downward transition $n \rightarrow m$ per second per atom exposed to radiation of intensity $\Im_\nu$. The transition probability of stimulated emission is of fundamental importance in the understanding of lasers. However, in our discussions, we will assume that initially the upper level population is negligible and therefore the stimulated emission process can be neglected.

Resonance radiation emitted in the transition from an excited state to the ground state, will not emerge from a mass of gas unattenuated by absorption followed by re-radiation. The progress of radiation through a gas by this means is known as radiative transfer. It was first discovered by Milne (1924), while numerous research papers on

the subject have been published [49, 50]. In the case of not-so-dense gases, the problem of radiation trapping or self-absorption can be easily handled using Holstein's Escape Factor approximation [51, 52].

2.3 Physics of Collisions

The detailed discussion of the theory of atomic and electronic collisions is not possible in this thesis. Several excellent books are available for that purpose [33, 53, 54, 55]. We will very briefly describe what is meant by a collision. This will be followed by some examples of collisions. Subsequently we will describe the collision probabilities and the rate coefficients. We will also present an overview of techniques which could help us in obtaining some insights about the physics of collisions. A simple kinetic model will then be presented which deals with the particular problem of thermal collisions between excited atoms and buffer gases [56].

A two-body collision is said to have taken place when any physical change can be detected after the distance between two particles has first decreased and then increased. Such physical changes include angular deflection or change in magnitude of momentum vectors (within the limits of uncertainty principle), changes in kinetic or internal energy, chemical changes, and the gain or loss of electrons. Collisions involving only the exchange of kinetic energy are termed "elastic"; collisions in which kinetic energy is converted into internal energy are termed "inelastic", and when the internal energy is converted into kinetic energy, the collision is termed "superelastic" or a "collision of the second kind". When the colliding particles do not have directed

motion as in accelerated particle beams etc., we have thermal collisions. These collisions can be particularly important in high temperature metallic vapors where large populations of highly excited atoms can be selectively prepared using step-wise laser excitation [57, 58, 59, 60]. Here a number of other states exist which are quite close to the "parent state" on energy scale.

In a three-body inelastic collision, a third particle, sometimes termed the "chaperon", influences the collision process, usually by the removal of excess internal energy as kinetic energy; the physical change taking place in the two-body process is affected by the temporary presence of the third body. Two-body inelastic collision processes will be discussed in the following sections.

2.3.1 Kinetic Collisions and Optical Collisions

The primary condition for a bi-atomic process is close approach of two atoms, which in normal terminology is called a collision. The "closeness" of approach is a variable term and depends on the nature of interaction between the two colliding partners. For ground state atoms, the collisions are defined in simple terms by gas kinetic theory based on a hard sphere model. The number of collisions per second between unlike atoms A and B and between atoms of the same kind are respectively [54]

$$\left[\frac{8\pi RT}{\mu}\right]^{1/2} r_{AB}^2[A][B] \tag{2.6}$$

and

$$2\left[\frac{\pi RT}{M_A}\right]^{1/2} r_A^2[A]^2 \tag{2.7}$$

where,

μ is the reduced mass and M_A is the atomic weight of A,

$r_{AB} = r_A + r_B$ is the sum of the radii of atoms A and B and defines the collision cross-section σ_K $(= \pi r_{AB}^2)$, when two spheres are in contact.

If the average distance between nuclear centers at closest approach is greater than the sum of the radii of the two colliding atoms, then such a collision is termed as an optical collision. On the other hand, for the kinetic collisions, the two colliding partners are in contact with each other during the collision process as illustrated in Figure 2.1. Thus for an atom in the excited state, direct contact between two interacting partners may not be necessary and effective cross-section for optical collisions may be much larger than those for kinetic collisions.

The effective cross-section σ_o $(= \pi R_{AB}^2)$ for optical collisions is proportional to the square of the distance R_{AB} over which the excited atom can interact with another atom to bring about a physical or chemical change. In some instances the effect of a foreign gas on the spectrum lines of a given element is to give very broad lines and large optical cross-sections. In favorable cases optical cross-section may be 10 to 100 times the kinetic cross-section. This is interpreted to mean that even at great distances another gas atom may act on the radiating atom strongly enough to change the phase of the oscillation. This approach is normally used for atomic gases and vapors which will be discussed here, because it has provided a wealth of information about the mode of excited state interactions.

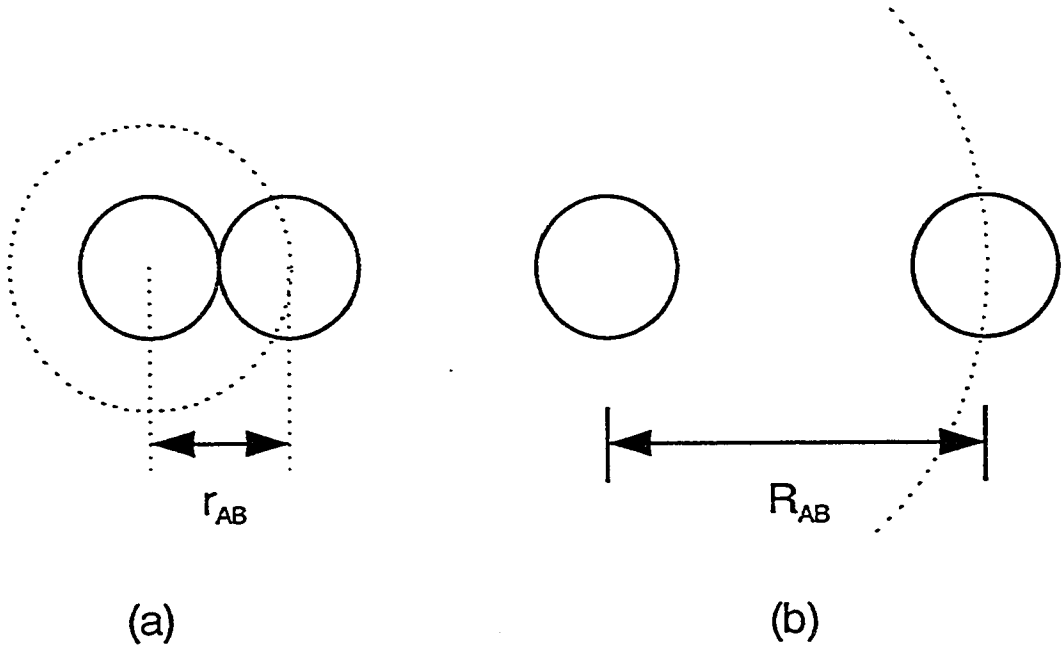

Figure 2.1: Schematic representation of (a) Kinetic collision and (b) optical collision.

2.3.2 Electron Collisions with Atoms

The elastic scattering of electrons is important in situations where only electrons and gas are present, so it is possible for electrons to escape from the relatively sluggish ion motion. In atomic gases, the electron velocity distribution is strongly influenced by the momentum loss experienced in elastic collisions; but inelastic processes can dominate in molecular gases

The passage of electron beams through gases is strongly influenced by elastic collisions. Electrons of energy much greater than that of the outer atomic electrons are scattered in collision with atoms through very small angles or through angles close to 180^0. Slow electrons are scattered more isotropically (centre-of-mass and laboratory angles are almost identical). Classically, if the electron impact velocity v decreases, the total scattering cross-section should increase as v^{-1}. The total scattering cross-section defined in terms of finite lateral deflection Δx from pre-collision path would have no limit in classical mechanics except the limit of resolution of the apparatus used for its measurement. In quantum mechanics, however, from the Heisenberg's principle

$$\Delta x \Delta v_e \simeq \frac{h}{m_e} \tag{2.8}$$

limits the resolution which is significant in theory, placing a finite limit upon the cross-section.

2.3.3 Excitation Exchange and Quenching

Excited atoms in collision with their own species can readily exchange the excitation, allowing the radiation to diffuse through the gas. In collision with a different species, the process can occur frequently when the energy defect is sufficiently small [61], but for larger energy defect the probability of its occurrence is slight. In collisions of excited atoms with molecules, the likelihood of occurrence of a small energy defect is often large, the molecule being left with vibrational - rotational excitation; hence the radiation from excited atoms is readily quenched by molecular impurities. Similar considerations apply to collisions of metastable atoms; deactivation of the metastables by excitation exchange with molecules will often occur. The excitation exchange process is known as sensitized fluorescence. Excitation exchange between unlike gases is an important process in the optical pumping of at least two gas-lasers [62].

Information about these processes is mostly obtained from experiments at thermal energies. The collision process, in which an excited atom in collision with a ground state atom falls to the ground state without radiation, whilst raising the second atom to an excited state, was first proposed by Franck in 1922 [63]. It is not essential that either atom should pass into or out of its ground state, but this is the most common situation.

When the process is exothermic, of energy defect ΔE, internal energy is converted into kinetic energy and distributed amongst the collidants, so their velocities would be [53]

$$\frac{1}{2}m_1 v_1^2 = \frac{\Delta E m_2}{m_1 + m_2} \tag{2.9}$$

and

$$\frac{1}{2}m_2v_2^2 = \frac{\Delta E m_1}{m_1 + m_2} \tag{2.10}$$

assuming zero ante - collision velocity. The velocities of the radiating atoms give rise to Doppler frequency shifts $\Delta\nu$

$$\frac{\Delta\nu}{\nu} = \frac{v}{c}\cos\phi \tag{2.11}$$

where ϕ is the angle between the line of observation of the radiation and the velocity vector v. For thermally agitated atoms, an average value of $\cos\phi$ is appropriate.

The first experiments upon excitation exchange (sensitized fluorescence) were conducted by Cario and Franck [64, 65], who irradiated mixed vapors of mercury and thallium with a mercury resonance lamp and measured the emission of the thallium lines. It was shown that the excitation exchange process is most probable for the smallest energy defect. For excitation transfer between alkali metal states, Franck [65] formulated the empirical rule $\sigma \propto \Delta E^{-\alpha}$, for energy defect ΔE, and α a constant.

Quenching collisions are those which destroy the resonance radiation from discharges when small quantities of another gas are added. The state in which the second gas finds itself after the collision is not specified and depends on the nature of collision partners and the experimental conditions. Resonance states are destroyed by excitation exchange collisions which even at thermal energies compete with spontaneous emission. Resonance radiation can hardly be quenched at all by the addition of atomic gases, since conversion of internal energy to kinetic energy is a very inefficient process in thermal energy collisions between atomic systems. The quenching

is related to the ratio of the intensities I and I_0 of resonance radiation, respectively with and without the foreign gas; from this quantity the collision cross-section can be calculated.

2.3.4 Scattering and Deactivation of Metastables

Metastables are those atomic species whose lifetimes are relatively long [27, 29, 66, 67]. The selection rules of quantum mechanics determine which states are unable to pass spontaneously to a lower state by electric dipole transitions. Thus a metastable state is sufficiently long-lived to enable them to undergo collision processes in atomic vapors.

Since the symmetrical resonance excitation transfer collision of a metastable atom in its own gas is indistinguishable from elastic scattering except in angle and polarization, both processes are included in the scattering cross - section and the diffusion cross - section; the total and diffusion cross - sections are as usual [53]

$$\sigma = 2\pi \int_0^{\pi} \frac{d\sigma}{d\Omega}(\theta) \sin\theta d\theta \tag{2.12}$$

and

$$\sigma_d = 2\pi \int_0^{\pi} \frac{d\sigma}{d\Omega}(\theta) (1 - \cos\theta) \sin\theta d\theta \tag{2.13}$$

The diffusion of metastables is similar to the diffusion of ions in their own gases; the inelastic process results in scattering through a large polar scattering angle, while in the elastic process θ is small.

2.3.5 Electron and Photon Collisions with Metastables

Excitation cross-section of excited atoms by electrons can achieve enormous peak values, but the peaks are extremely sharp, and even the thermal velocity distributions of thermionic electrons are sufficiently broad for the excitation rates to be much reduced.

Collisions of the second kind between electrons and metastables are also of importance. These are processes resulting in downward transitions in which the internal energy is converted into kinetic energy of the electron [66, 67]. Ionization of metastables by electron collisions is of importance in ionized gases, since the formation of a proportion of the ions can take place in a two stage process as outlined in section 1.1.3 above (see Eq. 1.7, to 1.9).

As regards photon absorption by metastables, the absorption of radiation of suitable wavelengths is one of the methods by which metastable densities can be monitored [53].

2.3.6 Collision Cross-sections and Rate Coefficients

Collision Cross-section in relation to Mean Free Path: A simplified visualization

The measure of the probability of a collision process is the collision cross-section denoted by the symbol σ. Let us consider a hard spherical gas atom of radius r moving with velocity v among similar atoms which are at rest. In time dt, it moves a distance vdt and encounters any atoms whose centres lie within a cylinder of radius 2r

and length vdt; i.e., it makes $\pi n(2r)^2/vdt$ collisions, where n is the gas atom density (atoms cm^{-3}). The mean distance l_f between collisions is therefore given by

$$l_f = \frac{1}{4\pi r^2 n} = \frac{1}{\sigma n} \tag{2.14}$$

where

$$\sigma = 4\pi r^2 \tag{2.15}$$

is the cross-sectional area of the atomic or molecular sphere. A more careful analysis due to Maxwell includes the relative motions of all the atoms, and leads to a factor $\sqrt{2}$ in the denominator [53].

The hard-sphere concept, whilst surprisingly effective, is only an approximation to an interatomic potential with a strongly repulsive core and weakly attractive skin.

Rate Coefficients

Inelastic collision probabilities are often defined in terms of "rate coefficients" rather than cross - sections. In a reaction between two particles, converting them into different species, the rate of change of number density n_1 of the first is

$$\frac{dn_1}{dt} = -kn_1n_2 \tag{2.16}$$

where k is the rate constant or coefficient, defined in units of cm^3 sec^{-1} $(particle)^{-1}$; the bracketed term is usually omitted. The rate coefficient is the integrated product of cross - section, impact velocity and normalized velocity distribution

$$k = \int_0^\infty v_r \sigma(v_r) f(v_r) dv_r \tag{2.17}$$

where $f(v_r)$ is the fraction of encounters in which the relative velocity v_r of impact lies between v_r and $v_r + dv_r$ [53]. Under some circumstances, the velocity distribution $f(v_r)$ may be replaced by a mean velocity $\bar{v}_r$, so that

$$k = \sigma \bar{v}_r \tag{2.18}$$

Equation 2.18 is often an excessively crude approximation, the calculation of k from equation 2.17 when $\sigma(v_r)$ and $f(v_r)$ are known is straightforward, but will usually require a computer.

Three - body collisions are conveniently considered in terms of three - body rate coefficients k_3, defined by the relation

$$\frac{dn_1}{dt} = -k_3 n_1 n_2 n_3 \tag{2.19}$$

and measured in units of $cm^6\ sec^{-1}$. Three - body rate coefficient are typically 10^{-27} to $10^{-31}\ cm^6\ sec^{-1}$, compared with two - body electron rate coefficients of 10^{-7} to $10^{-12}\ cm^3\ sec^{-1}$ [68].

At gas pressures in excess of 1 Torr, three - body collision processes become important, even dominant. The role of the third body, which can either be a gas atom or molecule, is usually to remove the excess energy that could otherwise only be liberated as electromagnetic radiation (an inefficient process). Another possible role of the third body is to stabilize collisionally an unstable state, which could otherwise undergo a transition preventing the inelastic collision process under consideration.

In our work, however, we will deal with the calculation of the two-body rate coefficient only, with the help of the following kinetic model. The actual application of the model to the experimental data for the retrieval of some rate constants will

be shown in chapter containing the experimental results. More specifically, we will consider the collisions of Ca atoms excited to a particular state and Ar buffer gas. One result of collisions is transfer of Ca atoms to nearby states which could be monitored, for example, through a study of fluorescence from these states.

2.4 A Simple Kinetic Model for Calculating Rate Constants

Of particular interest in the work discussed in this thesis is the study of energy transfer from the 3d4p $^1D_2$, 3d4p $^3F_4$, 4s5p $^3P_2$, 3d4p $^3D_1$ and 4s5s $^3S_1$ states of calcium atoms to nearby states of calcium through collisions with Ar.

A typical energy level diagram illustrating the states involved and the monitored fluorescent transitions is shown in Figure 2.2. After a particular "parent" state has been prepared by step - wise laser excitation the rate of change of instantaneous population of a state 'i' is given by

$$\frac{dn_i}{dt} = \left(\Gamma_i + \sum MK_{ij}\right) n_i + \sum MK_{ji} n_j \qquad (2.20)$$

where

K_{ij} is the state-to state rate constant for population transfer from state i to j.

M is the rare gas density.

n_i is the time dependent density of the i_{th} state.

Γ_i is the total radiative rate of state i.

The only non-zero initial population is that of the laser-excited parent state n_1.

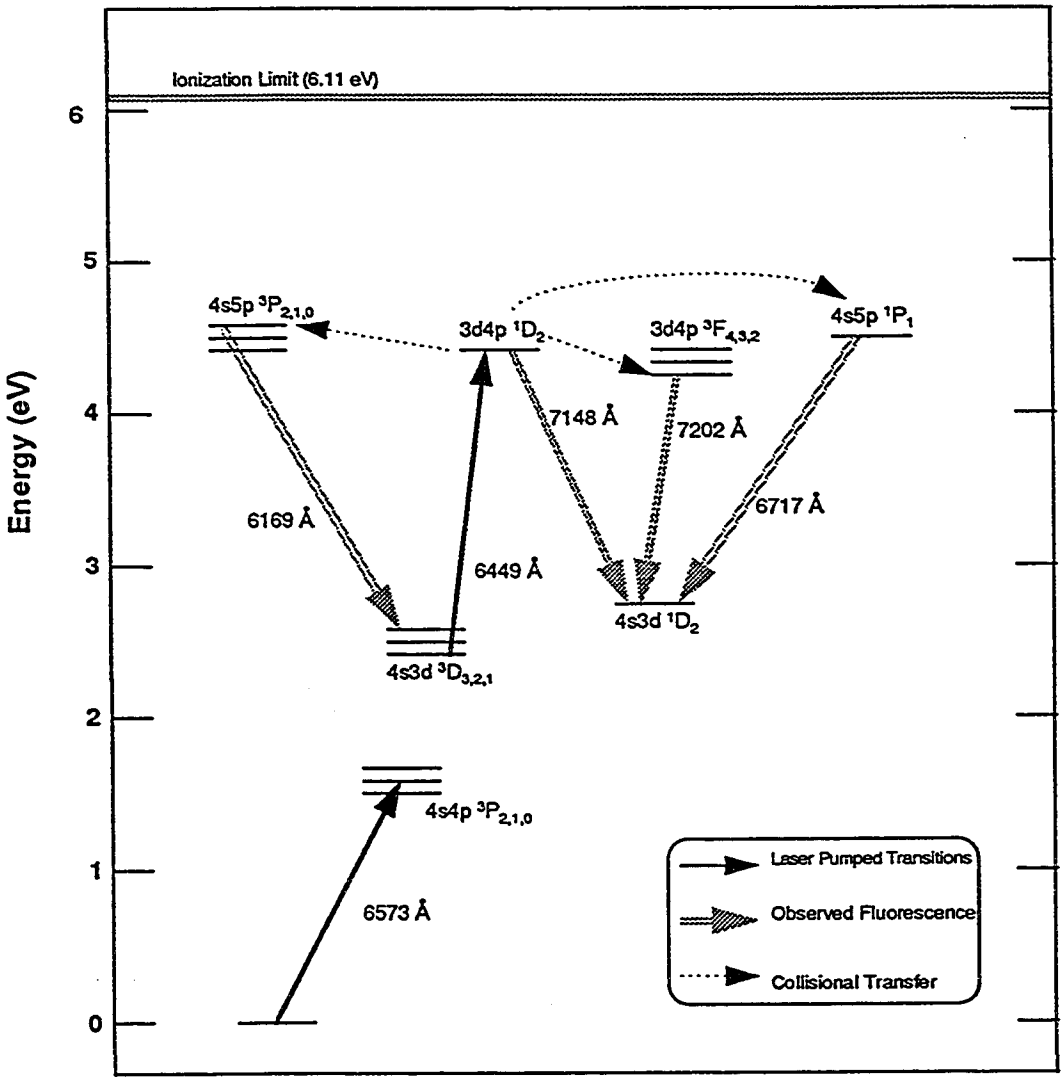

Figure 2.2: Partial energy level diagram for the calcium atom showing the laser-excited parent state 3d4p $^1D_2$, the predominant product states (4s5p $^3P_1$, 3d4p $^3F_2$, 4s5p $^1P_1$) populated by collisions with Argon, and fluorescent transitions observed.

Experiments on intermultiplet transfer have been carried out using similar kinetic models [69, 70]. The kinetic scheme can be simplified through the empirical observation, firstly that the radiative rates of the product states are relatively large compared to the radiative rate of the parent state. And secondly, with the ability to limit and control the collision rates K_{ji} by keeping the rare gas density "low". This results in a system of equations where secondary collisions which repopulate the parent state are ignored ($K_{ji} = 0$). Then equation 2.20 reduces to the form

$$\frac{dn_1}{dt} = -\left(\Gamma_1 + \sum MK_{1j}\right) n_1 \tag{2.21}$$

where $\frac{dn_1}{dt}$ is the rate of change of the population of the parent state (which is negative in this case because of depopulation).

The product states, on the other hand, are only populated by transfer from the initial (parent) state and are depopulated only through radiation. Thus

$$\frac{dn_j}{dt} = MK_{1j}n_1 - \Gamma_j n_j \tag{2.22}$$

where $\frac{dn_j}{dt}$ is the rate of change of the population of the product state. Integrating equation 2.21 yields

$$n_1(t) = n_1^o e^{-(K_d M + \Gamma_1)t} = n_1^o e^{-K_{eff}t} \tag{2.23}$$

where K_d is the deactivation rate constant defined as

$$K_d = \sum K_{1j} \tag{2.24}$$

and K_{eff} is the effective decay time.

Substituting equation 2.23 in 2.22 gives us

$$n_j(t) = \frac{K_{1j} M n_1^o}{\Gamma_j - K_d M - \Gamma_1} \left[e^{-(K_d M + \Gamma_1)t} - e^{-\Gamma_j t} \right] \tag{2.25}$$

To determine K_d, we plot the inverse exponential decay times ($1/K_{eff}$) for time-resolved emission of the parent state as a function of rare gas density and extract the slope. On the other hand, K_{1j} can be found by wavelength-resolved emission spectra of the product states using a boxcar integrator.

Integrating equation 2.22 (product states) over the gate width of the boxcar and setting the boxcar such that the initial and final populations of each level is zero we get

$$K_{1i} M N_1 = \Gamma_i N_i \tag{2.26}$$

or

$$K_{1i} = \frac{\Gamma_i N_i}{M N_1} \tag{2.27}$$

This equation enables us to find the individual state-to-state rate constants directly from the integrated emission spectra (where Γ_i is known). The emission signal for a particular product state is

$$S_i = A_{ik} N_i E F(\lambda_i) \tag{2.28}$$

Thus,

$$N_i = \frac{S_i}{A_{ik}} \frac{1}{EF(\lambda_i)} \tag{2.29}$$

where,

S_i is the integrated voltage signal of a product state emission line,

A_{ik} is the Einstein A coefficient for the transition from state i to state k,

N_i is the time integrated population density for state i,

E is an electronics factor which accounts for the boxcar gate, input impedance, and scale settings,

$F(\lambda_i)$ is an optical detection factor which includes the solid angle of light collection, the transmission/reflection coefficient of the collection optic, the monochromator transmission function, and the photomultiplier responsivity.

Using equation 2.27 for the forward rate constant K_{1i}, which relates to the population transfer from the parent state to the product state i, and substituting for the time integrated populations N_1 and N_i using equation 2.29 gives

$$K_{1i} = \Gamma_i \frac{1}{M} \frac{S_i}{S_1} \frac{A_1 F(\lambda_1)}{A_{ik} F(\lambda_i)} \tag{2.30}$$

which is the equation used to determine the K_{1i} from the experimental data. Thus in the limit that the model is exact, the rate constant is proportional to the ratio of normalized emission signals from the product state and the parent state, with a proportionality constant of the radiative rate of the product state times the rare gas density.

Qualitatively, one can rationalize this kinetic scheme by supposing that due to the large radiative rates of the product states, population does not build up significantly enough at low rare gas density to allow atoms to be transferred back to the parent state before radiation has removed virtually all of the excited calcium atoms. Also, were secondary collisions significant the exponential decay of emission from the parent state would be noticeably nonexponential.

Chapter 3

Experimental setup and Experimental Procedures

The experiments were carried out at the Laser Research Laboratory of the Energy Resources Division in the Research Institute. The experimental setup consists of three main systems:

- The laser systems
- The heat pipe oven
- The detection and signal processing system

The three systems are briefly discussed below.

3.1 The Laser Systems

Two different laser systems were used for the experiments discussed in this thesis.

- Nd:YAG Laser [Quanta Ray DCR 2A(20)] pumped Dye Laser (PDL-2) system
- Excimer Laser (EMG 203 MSC) pumped Dye Laser (FL 2002E) system

3.1.1 Nd:YAG Laser DCR 2A(20)

The ND:YAG Laser is the most versatile solid state laser system. It can operate as a cw laser, a pulsed laser with both long pulse (spiking mode) or Q-switched outputs and as a mode-locked laser. The laser consists of a pump source, usually a flashlamp, and a Laser rod contained in an elliptical reflector structure. The laser resonator with components such as a Q-switch, polarizer, and etalon complete the optical system. The flashlamp is driven by a discharge current that is usually switched from a storage capacitor. The capacitor is charged from a pulse charging power supply. The power supply package is completed with a timing circuit, a Q-switch circuit and a water circulation system for cooling the lamps and the laser rod.

The Nd:YAG Laser rod consists of a host material which is the YAG crystal (*Yttrium aluminum garnet* $Y_3Al_{15}O_{12}$) and an active lasing ion which is the Nd^{+3} ion. It is a four level laser system. Flash lamp energy is absorbed in the pump bands that are centered toward the red end of the visible spectrum. The absorbed energy is rapidly transferred to the upper laser level with a spontaneous lifetime of 230 microseconds. Thus the flash lamp can be operated for pulse duration of upto 200 microseconds and still pump the upper laser level efficiently. This long upper level lifetime is an important factor in this laser. It allows slow pumping and in this way avoids the complexity of fast pulsed electronics. Long lamp discharge pulses increase

the lamp lifetime and more efficiently couple the flashlamp output into the Nd:YAG upper level.

A simplified energy-level scheme for Nd:YAG is shown in Fig. 3.1 These levels arise from transitions of the three inner shell 4f electrons of the Nd^{+3} ion in the field of the YAG crystal. Since these electrons are screened by eight outer electrons ($5s^2$ and $5p^6$), the energy levels involved are only weakly influenced by the crystal field and the corresponding transition frequencies are relatively sharp. E1 represents the ground state of the Nd^{+3} ion, E2 is the lower laser level, E3 is a metastable state representing the upper laser level and E4 represents an absorption band. The excitation energy, absorbed from the flash lamp, raises the system from E1 to E4. Then, the system rapidly decays nonradiatively into the metastable state E3. Thus, a population inversion is established between E3 and E2, and hence, lasing action can take place between these two levels.

The Nd:YAG laser system DCR 2A(20) consists of an oscillator and an amplifier. The oscillator consists of a 100% mirror, Q-switch, polarizer, the laser head containing the oscillator rod, etalon and the output mirror. The temperature controlled intra-cavity etalon is an optional accessory which narrows the linewidth to less than 0.2 cm^{-1} at the 1064 nm wavelength. A 10 % reduction in the output energy is possible when using this accessory so provision is made for inserting or removing the etalon. The oscillator is shown in Figure 3.2. Q-switching is discussed briefly in the following section.

The amplifier consists of the laser head in which the Nd:YAG amplifier rod is housed. The laser head (oscillator and amplifier) is cooled with distilled water which

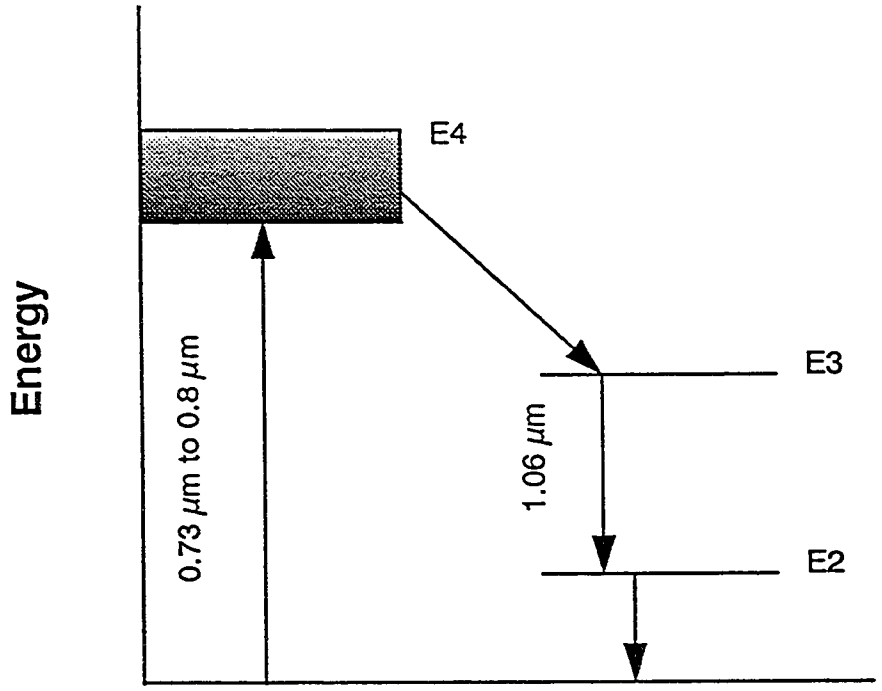

Figure 3.1: Simplified energy levels of Nd:YAG

circulates around the rod to remove excessive heat from the system. Dry nitrogen is used to keep the optical surfaces clean from dust. The oscillator and amplifier output energies increase with increasing flashlamp energy. At approximately 60-70 lamp joules the output of the oscillator begins to saturate. Increased energies can in principle be obtained by the addition of successive amplifiers.

Q-switching

The long upper level lifetime also allows energy to be stored and then rapidly released by Q-switching the laser oscillator. In Q-switched operation the laser energy is released in a few cavity round trips or in a pulse width of approximately 10 nanoseconds for a 60 cm long cavity in the present system. When operated at two times above the threshold of oscillations, more than 80% of the energy stored in the laser rod is extracted in the Q-switched pulse. Thus very high peak powers are obtained.

Q-switching is accomplished by using a KD*P (*potassium dihydrogen phosphate*) crystal as an electro-optic switch within the laser resonator. A high voltage is applied to this crystal in a Pockel's cell configuration which rotates the plane of polarization of an incident wave. The usual configuration is to use a polarizer, Q-switch crystal and a cavity mirror in sequence (see Figure 3.2). In this arrangement, only a one-quarter wave retardation is required of the electro-optic crystal to make the cavity have a high loss. Light transmitted by the polarizer passes through the quarter wave retardation, Q-switch crystal, reflects from the mirror and returns through the quarter wave retardation which is equivalent to a total of half-wave retardation. A quarter-wave plate rotates the incident polarization by 90° and thus causes the polarizer to

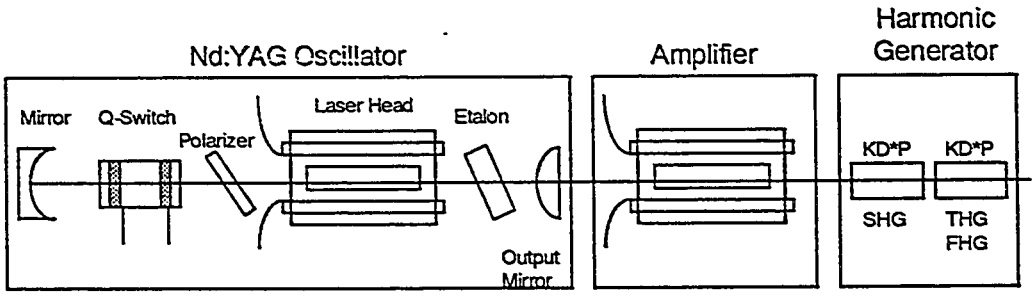

Figure 3.2: Nd:YAG laser system showing the optical schematic.

reject the reflected wave. To actuate the Q-switch, high voltage of the order of 3400V is rapidly shorted to ground potential causing the KD*P crystal to become a null-wave plate. Incident light can now be transmitted at low loss in the optical cavity.

The electro-optic Q-switch changes from high loss to low loss in approximately 10 ns. The laser medium has already been pumped to a high gain state by the flashlamp. Upon reaching a low loss condition, the laser field rapidly builds up to a high peak power pulse. The build up time from the opening of the Q-switch to emission of the Q-switched pulse is a function of laser gain or flashlamp energy. Figure 3.3 shows the timing of the emission of the Q-switch pulse delay and pulse width vs. input flashlamp energy.

Normally, the laser is operated at maximum output pulse energy which corresponds to a minimum Q-switch pulse width of 9 ns.

The timing stability of the Q-switch pulse is dependent upon the gain stability of the laser. For well engineered Nd:YAG oscillators, such as the Quanta- Ray system, the Q-switch pulse is emitted within ± 1 ns after the delay time of 40 ns from the

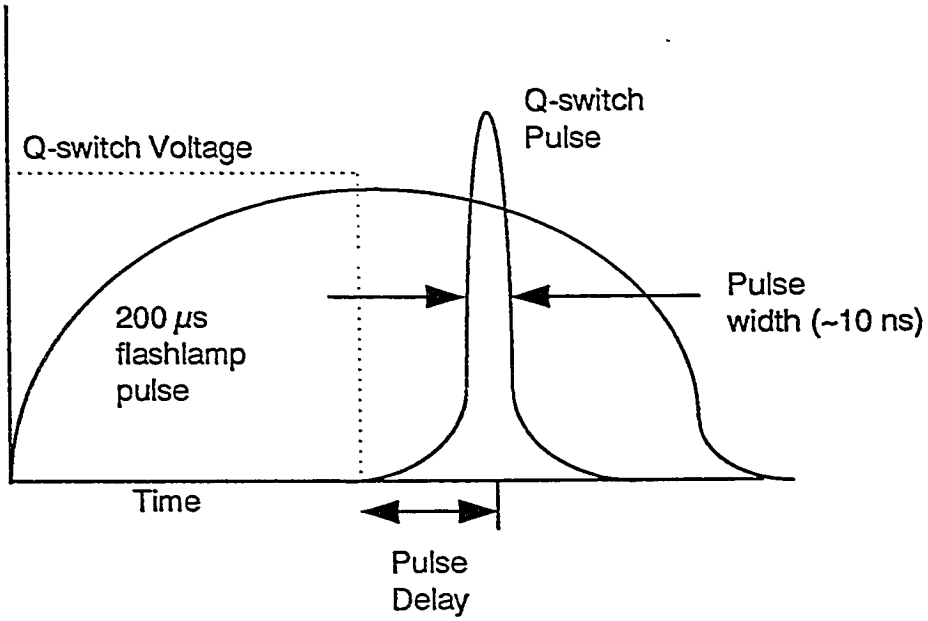

Figure 3.3: Flashlamp and Q-switch timing schematic.

opening of the Q-switch.

The Q-switch pulse delay time can be electronically adjusted within the flashlamp pulse duration. This property is useful for timing the laser to other events. A delay in the Q-switch pulse to delay the flashlamp pulse is also a convenient way to lower the laser output energy at constant flashlamp input energy conditions and thus at constant thermal loading of the laser rod. Although the primary 1064 nm Nd:YAG transition can be efficiently converted by harmonic generation and stimulated Raman scattering, to provide a wide range of fixed frequencies, tunable radiation is essential in most applications.

The system specifications of our Nd:YAG laser are: pulse repetition rate of 20 Hz with average power output of over 6 watts at 532 nm at 20 Hz operation and a

pulse width of 6-7 ns. Pulse to pulse energy stability is ±3 %, while long term power stability is ±5 % per 10 hrs at 355 nm.

Internal Timing Sequence of the Master Oscillator

An adjustable control knob provides the possibilities of obtaining laser pulses at a fixed frequency (10, 20 or 30 Hz), or at a variable frequency. The laser pulse repetition frequency (PRF) is controlled by an internal master (electronic) oscillator. If the Q-switch function control E is also at the NORM position for normal Q-switched operation, the following timing sequence occurs (see Fig. 3.4).

1. The master oscillator generates the oscillator sync out pulse.

2. The master oscillator also triggers the closing of a high voltage relay which applies the hold-off voltage to the Pockels cell.

3. Approximately 3 ms after the oscillator sync out pulse, the flashlamps are triggered and the flashlamp sync out pulse is generated.

4. After a delay of approximately 210 μs which is adjusted for maximum output, the Q-switch voltage is reduced to zero in approximately 10 ns and the Q-switch sync out pulse is generated.

5. Approximately 50 ns after the Q-switch sync out pulse, the laser light pulse occurs.

6. A variable sync out pulse is available which may be adjusted from 680 ns preceding the Q-switch sync out pulse to 1000 ns following the Q-switch sync out

pulse.

7. Approximately 6.5 ms after the oscillator sync out pulse, the high voltage relay opens and the voltage on the Q-switch reduces to zero.

HG-2 Harmonic Generator

Using the harmonic generator HG-2 which contains the KD*P (*potassium dihydrogen phosphate*) crystal, the emitted laser radiation 1064 nm is frequency doubled to obtain radiation at 532 nm. The 532 nm radiation is separated from the fundamental wavelength of 1064 nm using a dichroic separator. The emitted laser light is in the form of pulses with a pulse width of 10 ns and a pulse repetition rate of 20 Hz. This laser light is within the visible region, and thus, is very useful for the pumping of tunable dye lasers which are widely employed in laser atomic spectroscopy. Provisions also exists for obtaining third harmonic radiation at 355 nm, but this was not used in the present experiment. A continuous flow of dry nitrogen (purge) was also maintained through the HG-2 housing in order to keep the dust away from the optical surfaces.

3.1.2 Dye Laser (PDL-2)

Dye lasers are optically pumped lasers. A schematic diagram of the PDL-2 system in our laboratory is given in Figure 3.5. In the standard configuration, the PDL-2 consists of an oscillator, a preamplifier and a final amplifier which may be either side-pumped or end-pumped, and pump beam distribution optics. A small fraction of the pump beam (~10%) is split off to excite the oscillator; a similar fraction may

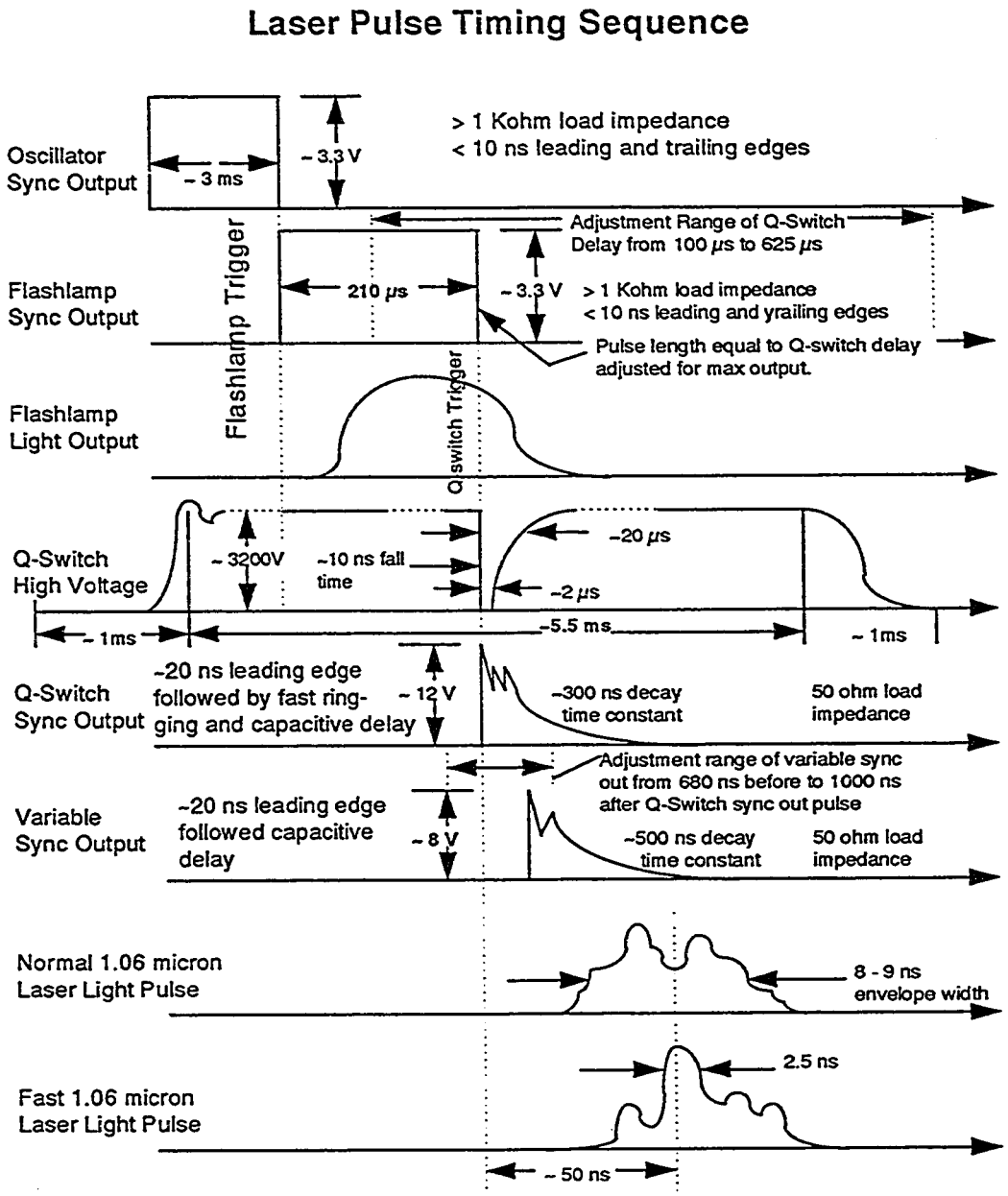

Figure 3.4: The internal timing sequence of the built in master oscillator.

be used for the preamplifier if desirable, and the remainder excites the amplifier. By splitting the energy, optical losses incurred in the dispersive oscillator have minimal effect on the overall efficiency of the PDL-2. The main component consists of an organic dye dissolved in a suitable liquid. The dye solution is circulated through oscillator and preamplifier while a more diluted solution (1:3) is circulated through the amplifier. When the dye solution is irradiated by a laser or a flashlamp, the molecules will be excited from the ground state into one of the rotational vibrational states of a particular electronic level. First, we recall that the selection rules require that $\Delta S = 0$. Hence singlet-singlet transitions are allowed, whereas singlet-triplet transitions are forbidden. Therefore, the interaction with electromagnetic radiation can raise the molecule from the ground level S_0 to one of the vibrational levels of S_1 state. Then the molecules decay by stimulated emission into one of the rotational-vibrational levels of the ground state.

The light thus emitted by the dye laser has a longer wavelength than the pump light source or the pump laser. Since there are a large number of rotational-vibrational states, a wide band is obtained within the fluorescent spectrum of the dye. This feature makes dye lasers very useful for atomic and molecular spectroscopy because they can be tuned throughout the emission range of the dye. In our present work the quanta-Ray PDL-2 pulsed dye laser was pumped by the second harmonic of Nd:YAG laser. Two different dyes were used. These are: DCM dye, which can be tuned from 605-680 nm and Rhodamine R590 which can be tuned from 550-590 nm. The optical layout of the oscillator is shown in Figure 3.7.

The oscillator is a precision monochromator coupled to a gain medium, and con-

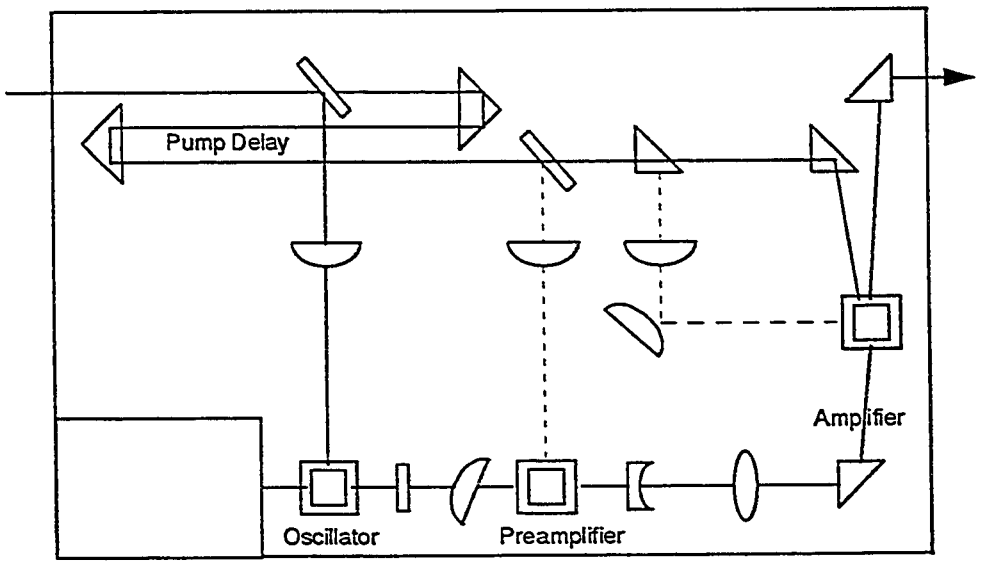

Figure 3.5: Schematic of Quanta-Ray PDL-2 pulsed dye laser.

sists of an output coupler, a dye cell, a prism beam expander, and a grating placed in the Littrow configuration. This design has the advantage of high efficiency and broad tuning range with a single grating. The grating disperses the light. Depending on the orientation of the grating, emission over only a narrow wavelength band will be reflected back into the oscillator cavity, providing the required feedback to achieve lasing. The absolute wavelength and wavelength band (line width) are therefore a function of the grating angle. By using different orders of the grating and different dyes, the dye laser can be tuned from 380 nm to 960 nm. Rotating the grating for tuning can be accomplished by a stepping motor. The precision sine bar, used to drive the grating, are carefully designed and temperature compensated to assure both scan linearity and wavelength readout.

For lower-gain dyes, an optical preamplifier is inserted between the oscillator and

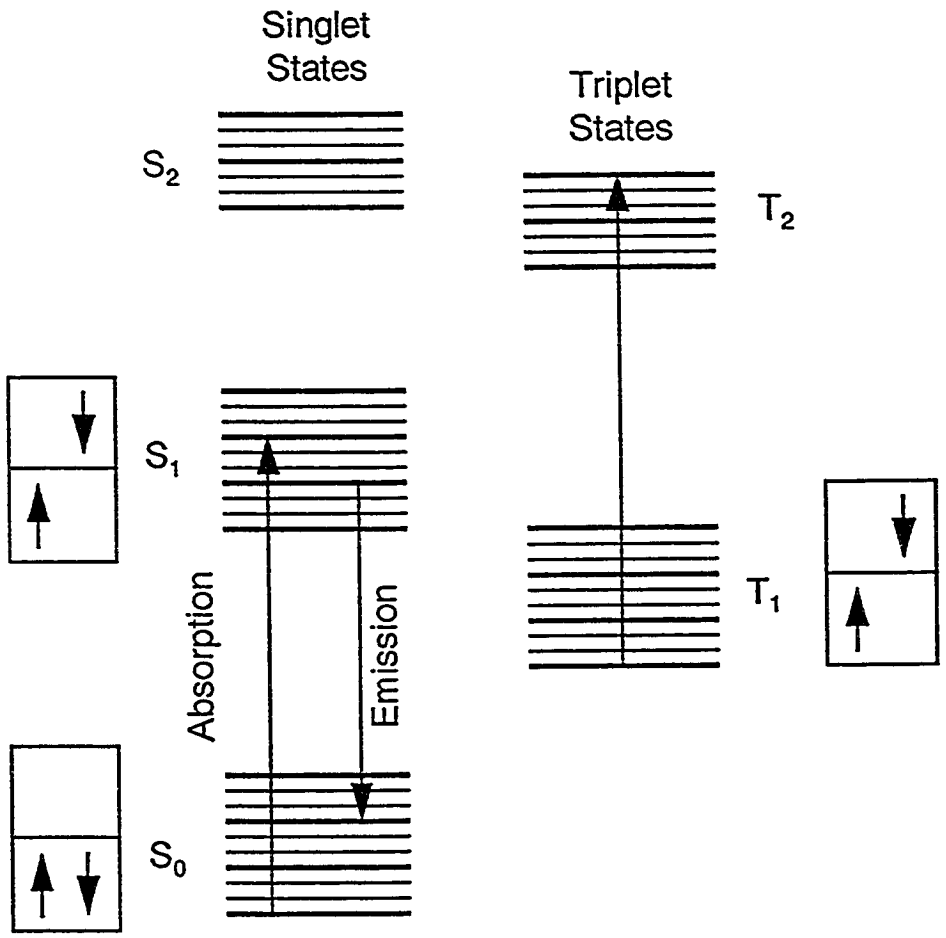

Figure 3.6: Typical energy levels for a dye in solution. The singlet and triplet levels are shown in separate columns.

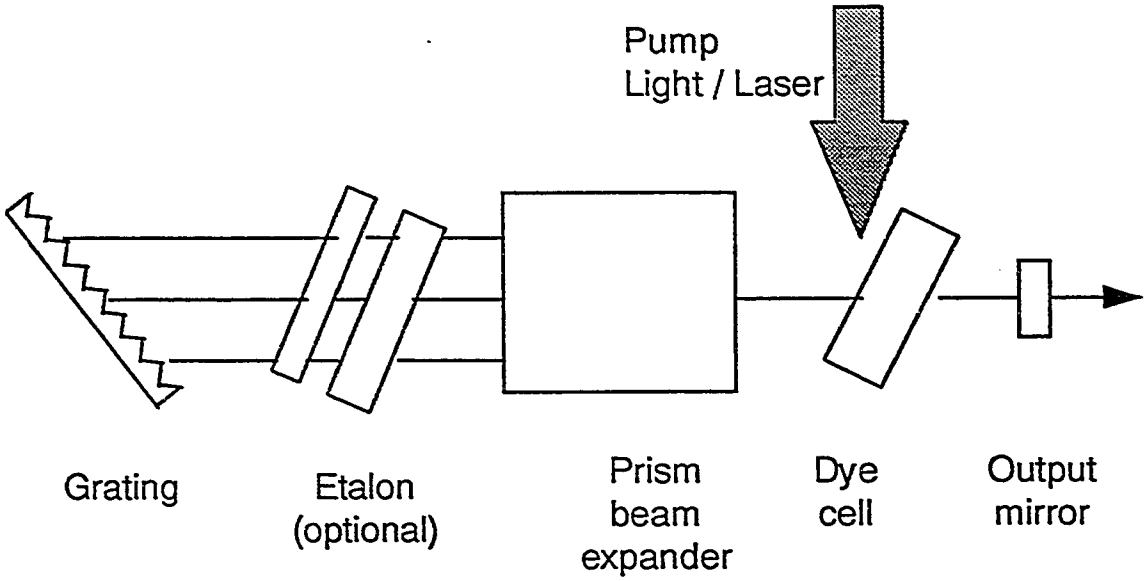

Figure 3.7: PDL-2 Oscillator Design

final amplifier. Both the oscillator and preamplifier dye cells are transversely pumped. A variable beam-expanding telescope expands the beam after the preamplifier to match the pump beam in the final amplifier. The final amplifier is configured such that it can be pumped either longitudinally (end-pumped) or transversely (side-pumped).

Typical pulses from our PDL-2 dye laser were 10 ns in width and the energy per pulse was of the order of 5 mJ. The line width without using the etalon was 0,12 cm^{-1}.

3.1.3 XeCl Excimer Laser (Lambda Physik EMG 203 MSC)

Excimers are molecules which do not have a stable (bound) ground state but exist in an excited state. The simplest excimer (excited dimer) is formed through bonding of

an excited atom with a ground state atom. Excimers are excellent sources of Laser radiation because it is very easy to excite population inversion in them. The XeCl molecule is of the rare gas monohalide species which exhibits stimulated emission and oscillates rather efficiently.

The general structure of the rare gas halide molecules is shown in Figure 3.8. The ground state correlates to the ground state ^1S rare gas and ^2P halogen atoms at infinite internuclear separation [71]. Because of the P character of the halogen atom (net orbital momentum of one), the ground state manifold consists of two states. Of these, the $^2\sum$, has the lowest energy since in this configuration the singly occupied halogen orbital is directed toward the rare gas atom. Since it forms the ground state, this state is referred to as the X state. This state is generally nearly flat or at most weakly bound (255 cm^{-1} in XeCl [72]).

The upper laser level is an ionically bound, charge - transfer state correlating to the ^2P rare gas positive ion and ^1S halogen negative ion at infinite inter - nuclear separation. Beginning at an energy equal to the ionization potential of the rare gas less the electron affinity of the halogen, the potential of this state follows a Coulomb curve which crosses, in a diabatic sense, the covalent curves correlating to excited states of the rare gas and halogen atoms. At close inter - nuclear separation, the potential energy curve splits into $^2\sum$ and $^2\Pi$ states as indicated. The ionic species which form the upper laser level have ^1S (halogen ion) and ^2P (rare gas ion) character, like the ground state species, but with the rare gas and halogen atom roles reversed. Thus, the structure of the ionic upper level manifold is similar to that of the ground state manifold, with the $^2\sum$ state lying lowest. By convention this is referred to as the

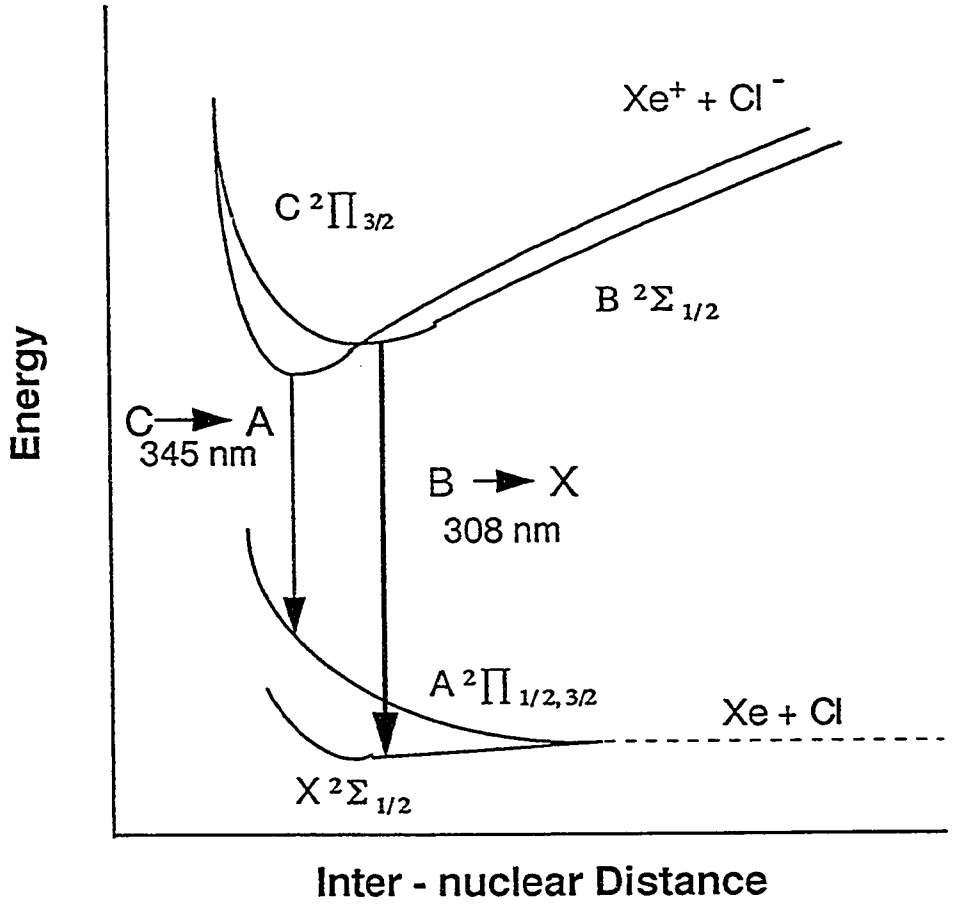

Figure 3.8: Schematic potential energy diagram illustrating the electronic structure of the rare rare gas monohalides (XeCl).

B state. In the interesting cases, the Coulomb curve crosses all the excited covalent curves, and the ionic state forms the lowest excited state (aside from the A state, which correlates to ground state atoms). Thus the lasing action is obtained from C to A at 345 nm and B to X at 308 nm. However, the peak at 308 nm is much more intense and sharp as compared at 345 nm. Our system is optimized for the 308 nm radiation.

The result of electrical excitation of predominantly rare gas mixtures is to produce both excited rare gas atoms and rare gas ions. Both these products lead very rapidly to excited rare gas halides. The excited species do this by direct reaction, for example,

$$Xe^* + Cl_2 \rightarrow XeCl^* + Cl \tag{3.1}$$

Reactions of this type occur with large cross sections, and frequently have near unit efficiency for producing excited products, [73]with rate coefficients generally of the order of 10^{-9} cm^3 sec^{-1}.

The mechanism for forming excited rare gas halides from ions and electrons begins with dissociative attachment of the electrons to the halogen to form negative ions. This is followed by three - body recombination of the negative halogen ions with the positive rare gas ions, for example

$$e^- + Cl_2 \rightarrow Cl^- + Cl \tag{3.2}$$

$$Cl^- + Xe^+ + Ar \rightarrow XeCl^* + Ar \tag{3.3}$$

Exothermic dissociative attachment reactions such as (3.2) are frequently very rapid, with rate coefficients as large as 10^{-7} cm^3 sec^{-1} at room temperature, but decreasing

somewhat at elevated electron temperatures [74, 75]. The three body recombination of ions (3.3) is likewise extremely rapid.

Pumping of the Rare Gas Halide Lasers

The gas mixture containing the rare gases and the Halogens in the presence of a buffer gas for a XeCl laser are pumped by a discharge. The discharges offer the potential for high pumping efficiency and high average laser power output. The reason for the high pumping efficiency is that it is possible, using a carefully controlled discharge, to pump the metastable levels of the rare gases directly by electron impact with very high efficiency. Basically in rare gas discharges the low energy electrons suffer only elastic encounters with the rare gas atoms, in which they lose very little energy. Thus, as they drift along the electric field they increase in energy until they reach the threshold for excitation of the first excited state of the rare gas atoms. Above this energy they experience inelastic collisions in which the rare gas atom is left in an excited state while the electron returns to a low energy.

To obtain the highest efficiency it is desirable to operate at the highest electric field. However, the extent to which this can be done is limited by discharge stability. The best way to achieve large pulse energy and high discharge efficiency is to use discharges which are stabilized by electron beam preionization or UV preionization. The purpose of the ionizing radiation (UV or electron beam) is to make up the difference between the rate of the ionization due to the discharge and the rate of electron loss due to dissociative attachment and recombination. In this way, it is possible to achieve absolute discharge stability [76] and the electron density and electric field

may be separately controlled to optimize performance.

The currently used excimer laser employes the thyratron (EMG 203 MSC). Thyratrons have been operated at high repetition frequencies, but they have some difficulty handling the large currents and short rise times required by fast discharge rare gas halide lasers. Energy from 20 - 100 J is stored inside a large storage capacitor. The typical requirements of the triggerable switch is peak currents of 5 - 30 kA, hold off voltage 30 kV and a rise current of 10^{10} - 10^{12} A/s. For an excimer laser discharge the breakdown voltage is around 30 kV with a current density of 500 A/cm^2. The discharge in this case is of 50 ns duration and dissipated energy from 10 - 50 J. The laser operation and several other functions such as gas filling, voltage and energy output are controlled by a small computer called ILC (Intelligent Laser Control). The block diagram of the system is shown in figure 3.9.

A mixture of different gases are needed for the laser operation depending on the wavelength required. The gases are mixed inside the gas handling system. In our present experiment Xenon, HCl (5 % in Argon) and Neon (buffer gas) are used with a purity of 99.99 % in the ratio of 60:80:2760 at a total pressure of 2900 mbar. Cooling water is required to cool the discharge system and the laser gases. The water flow rate depends on the repetition rate used and the temperature of the cooling water. An interlock turns the high voltage off, if the water flow rate falls below a minimum level. Typical laser energy per pulse is about 400 mJ while the pulse repetition rate is upto 250 Hz and the pulse width is 22 ns.

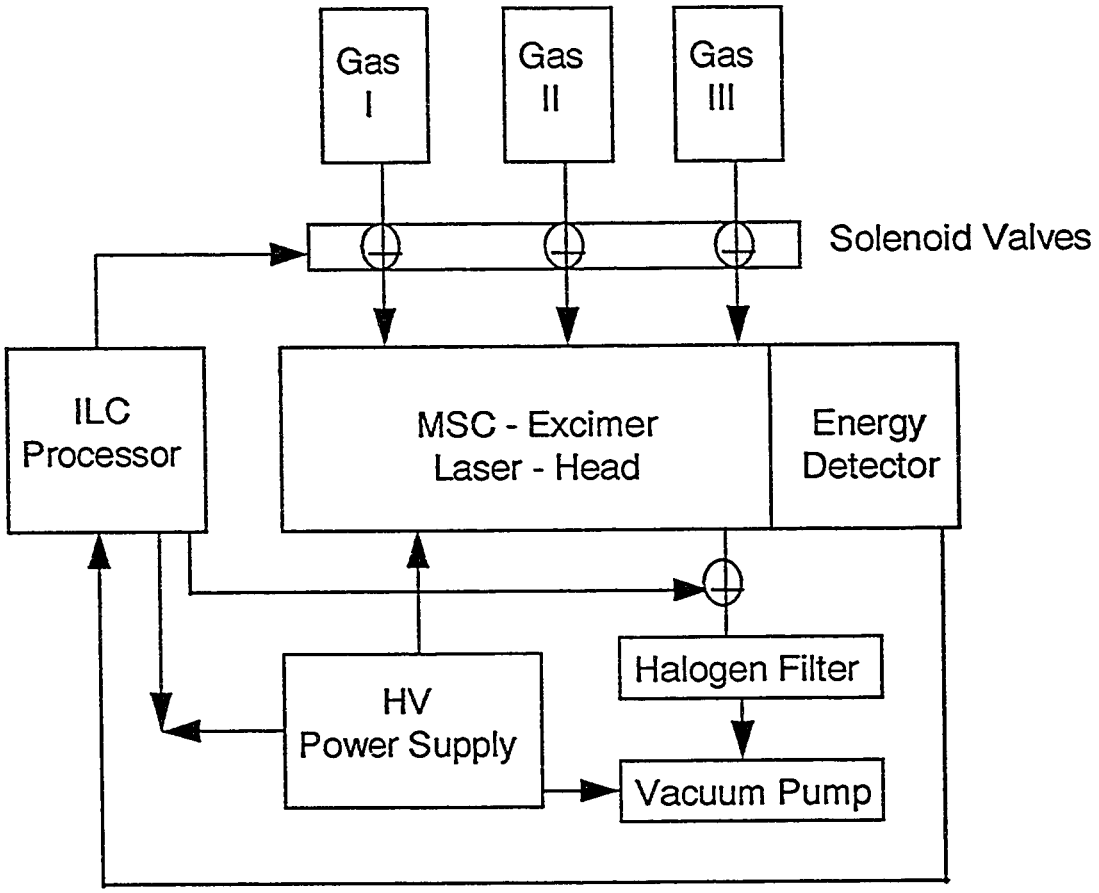

Figure 3.9: Block diagram of the Excimer Laser.

FL 2002E Dye Laser

The output of the excimer laser EMG 203 MSC is used to pump a tunable dye laser (Lambda Physik 2002E). The main parts of the FL 2002 dye laser are the oscillator, preamplifier and amplifier. The pump-beam path is as shown in Figure 3.10. The oscillator comprises of the dye flow cell and pump optics, the tuning block and the cavity end mirror. The tuning block contains components which determine the wavelength of the oscillator radiation. The grating can be tilted between Litrrow angles of 42.5^0 and 72.5^0. In the dye cell Rhodamine 101 (Lambda Chrome 6400) was used as the dye.

The specifications of the dyes used in this experiment are listed in Table 3.1, while typical tuning curves of the dyes used in the present experiment are shown in Figure 3.11. The FL 2002 dye laser gives an output energy upto 50 mJ at 623 nm using Rhodamine 101 dye.

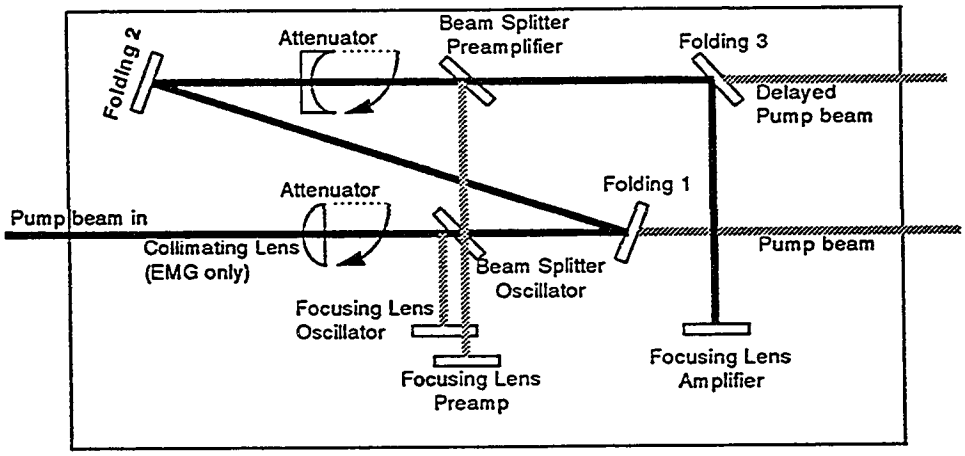

Figure 3.10: Schematic of the FL 2002 with the pump-beam path.

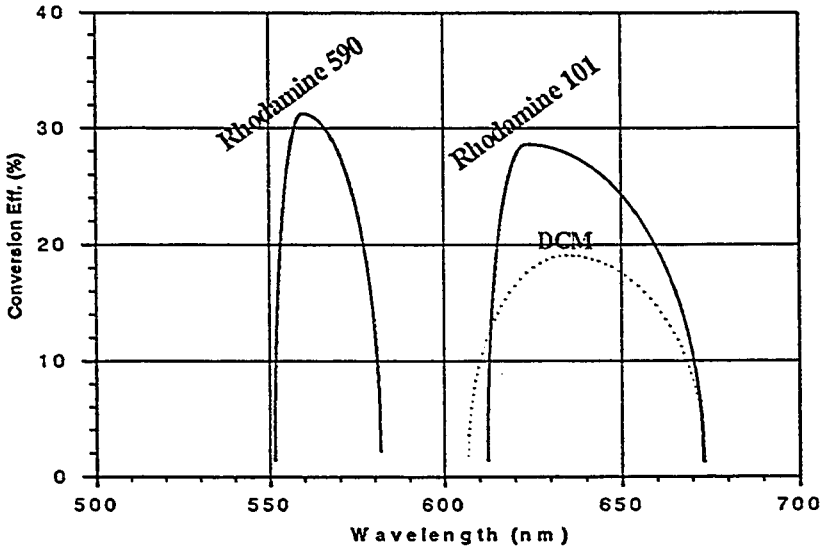

Figure 3.11: Typical tuning curves for the dyes used in this experiment.

Pump Source	Pump Source Wavelength (nm)	Dye	Peak (nm)	Tuning Range (nm)
Excimer (XeCl)	308	Rhodamine 101	623	614 - 672
Nd:YAG	532	Rhodamine 590	560	552 - 580
Nd:YAG	532	DCM	642	604 - 672

Table 3.1: Specifications of the dyes used in the experiment. For the above dyes methanol is used as the solvent.

3.1.4 Synchronization of the Laser Pulses

The laser pulses from the excimer laser and the Nd:YAG laser were synchronized through the delayed triggering technique [77]. More specifically, the synchronous output pulse from the internal master electronic oscillator of the Nd:YAG laser, which preceded its laser pulse by approximately 3.3 ms, was used to trigger a four-channel digital delay generator (Stanford Research SRS 535). After a specified delay, the excimer laser was triggered with a pulse from this delay generator to obtain a laser pulse from the excimer laser prior to the appearance of the laser pulse from the YAG laser. Note that the excimer laser pulse appeared about 1 μs after being triggered. In this arrangement, the appearance of the YAG laser pulse was fixed in time. However, to increase the delay between the pulses from the two lasers, the excimer laser had to be triggered at a specified earlier time before the appearance of the YAG laser pulse, allowing an adjustable maximum delay of the order of 3.3 ms. Figure 3.12 shows the delay between the pulses from the two lasers.

The two nearly coaxial laser beams originating from the two laser systems (Nd:YAG pumped dye laser system and Excimer pumped dye laser system) were adjusted to spatially overlap precisely in the central region of the heatpipe oven as shown in Figure 3.15. This was done by optically projecting the overlap region on a screen using a mirror. Subsequently fine controls employing micrometer adjustments were used for optimum results seen through enhanced signals displayed on the oscilloscope.

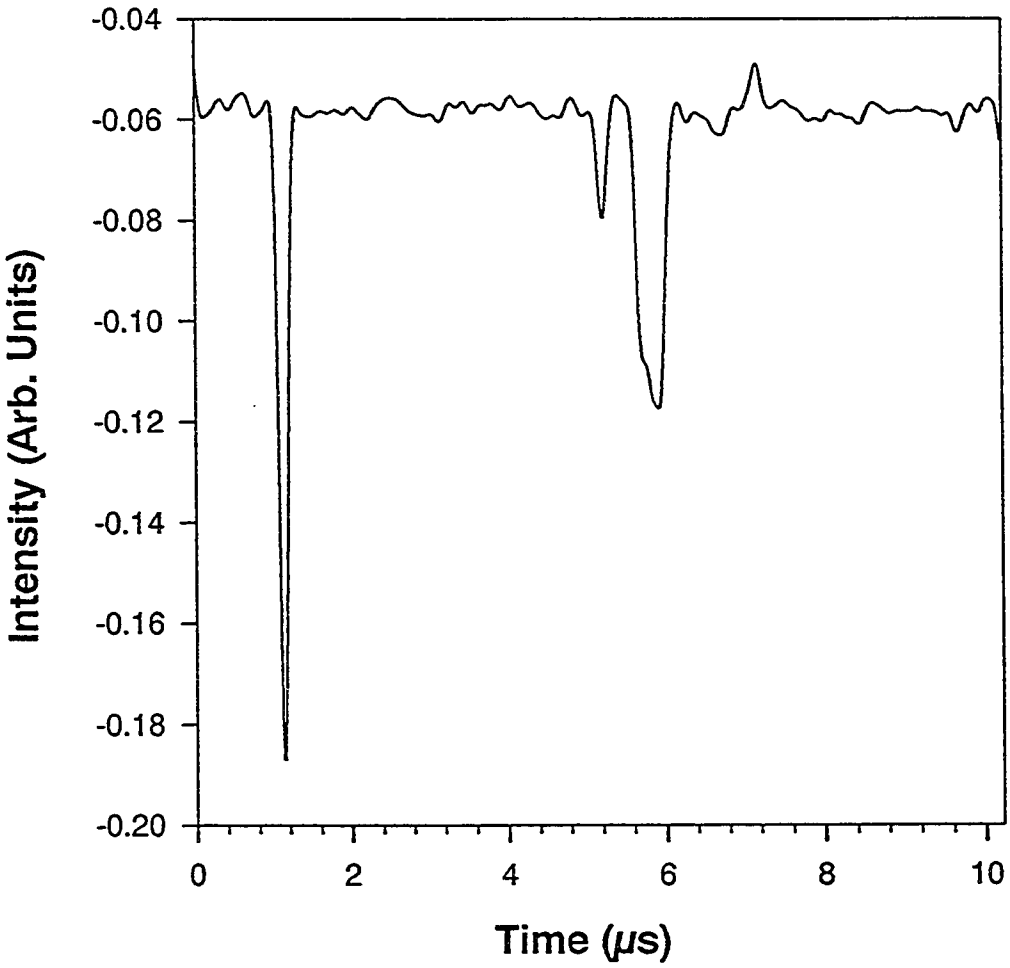

Figure 3.12: Delay between the pulses from the two lasers.

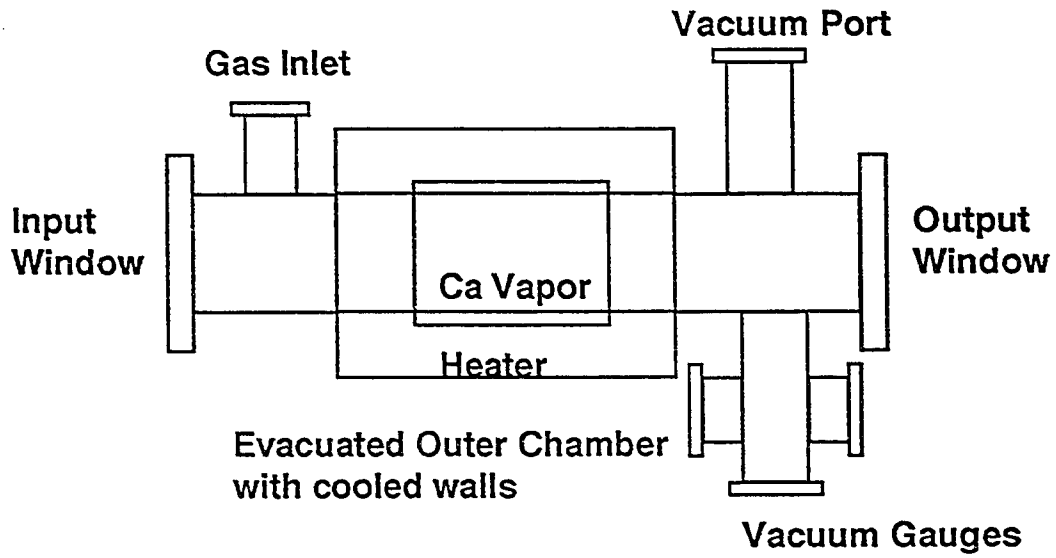

Figure 3.13: Schematic diagram of the heatpipe oven.

3.2 The Heat Pipe Oven

The calcium vapor was produced in a stainless steel heat pipe oven with an active region of 80 mm length and 25 mm diameter where temperatures upto 1000 °C could be maintained within 1 °C using DC power and a temperature controller. A schematic diagram is shown in Figure 3.13. High purity argon is used as a buffer gas to prevent the hot vapor from depositing on the optical windows of the heat pipe oven. The oven is evacuated to 10^{-6} mbar at a preheat temperature of 350 °C before introducing the buffer gas and before further heating the oven to operating temperatures in the range 600-725 °C. This ensures a contamination free environment.

The heater power supply (GP060-20) was controlled by an (Eurotherm 815) temperature controller. The temperature of the oven was read by a thermocouple placed

on the outside wall of the heated region. This heat pipe has provisions for gas inlet, vacuum ports and optical windows. The heat pipe is placed inside a vacuum chamber. This outer vacuum chamber has a cooling jacket through which water is circulated continuously to remove the excess heat and to protect the optical windows from the vapor at high temperatures. The vacuum pumping station consists of a turbomolecular pump and a mechanical rotary pump. The pressure inside the heat pipe can be read using a Pirani gauge and a Penning gauge. The pressure of the outer chamber was read with the help of another Pirani gauge. The buffer gas was fed into the heat pipe through a gas inlet valve. Buffer gases are usually inert gases like Ar, He, Ne, Kr. Initially, the rotary pump was employed to attain pressures around 10^{-3} mbar. Then, the turbomolecular pump was used to reach pressures as low as 10^{-6} mbar. A schematic diagram of the heat pipe oven and its peripheral devices is shown in Figure 3.14.

3.3 Data Acquisition and Data Processing System

Basically the signal processing system consists of the box car averager (4420 Princeton) and the signal processor (4402 Princeton). The box car averager is triggered with a synchronous output of the laser Q-switch. With the help of this system, we were able to detect the acquired signal in two modes, the waveform mode and the static gate mode. In the waveform mode the signal is detected as a function of time. Here, the gate scanned the signal waveform and recorded it in time as a normal oscilloscope. In the static gate mode the signal is detected as a function of wavelength. In

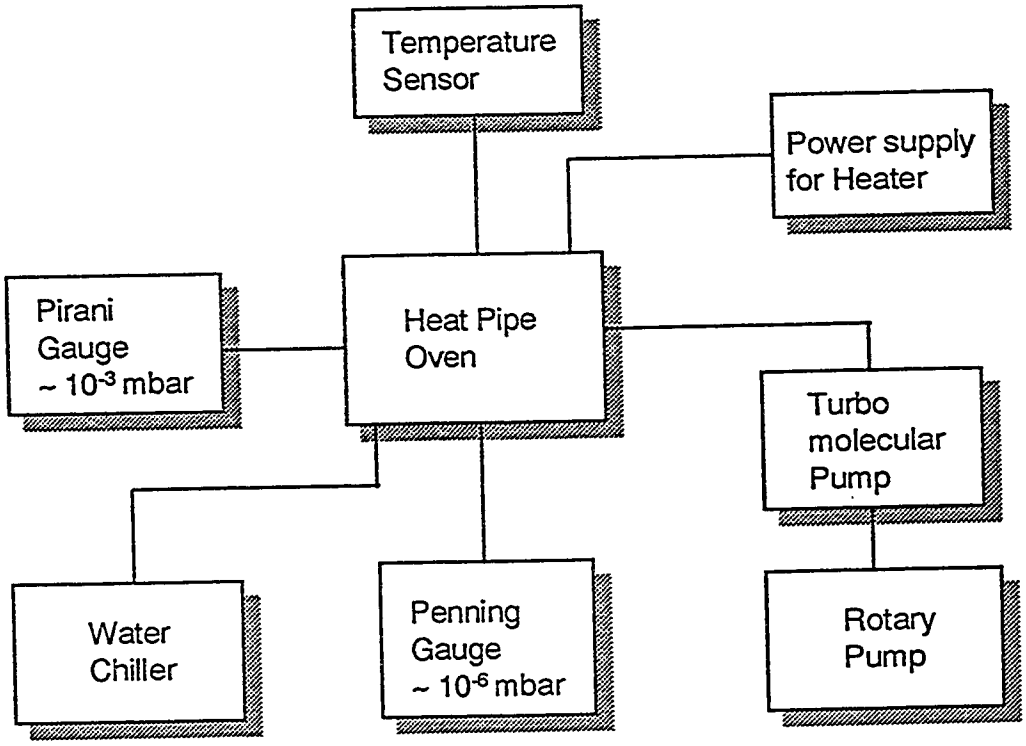

Figure 3.14: The heat pipe oven together with its peripheral devices.

this case the gate was fixed at a position corresponding to a point on the waveform which is usually the peak. In our present experiments the wavelength of the laser or the wavelength of light emitted by the vapor was scanned in the region of interest. The system also controlled the triggering level, the number of samples to be averaged per data point of the record and the number of points on the record.

The signal detection and analysis system incorporates both linear and digital averaging functions to achieve a uniquely powerful and flexible signal acquisition and processing system. This system provides high-speed sampling with variable time resolution, sophisticated digital signal averaging, multi-curve storage and display, and powerful data analysis. Exponential or linear averaging can be invoked to extract signals from noise in the way best suited to a particular application. A built in CRT provides annotated display of up to four curves simultaneously. Data storage is facilitated by multiple curve memories, a built in disk drive, an RS232C serial link, and an IEEE-488 parallel link. Virtually any arbitrary external signal can be used to trigger the system. Trigger pulses can be as narrow as 5 ns, allowing the use of beam-split, narrow, laser pulses to directly trigger the system. The system has been interfaced with an external computer using the IEEE-488 communications link provided. The curves obtained can thus be plotted on a plotter which in turn is linked with the external computer. Raw data are retained in volatile LC (live curve) memory for CRT viewing, with provisions to transfer these to internal MC (a total of 16 memory curves) arrays, disk, external computer or printer. Several post-acquisition processes like smoothing, area integration and many other mathematical functions can easily be performed on the signal processor.

3.4 The Monochromator and Photomultiplier

The fluorescence emission from the atomic vapor was detected with the help of a 0.5m scanning monochromator (SPEX 1870). Fluorescence is directed by an off-axis lens and an off-axis mirror towards the monochromator and a thermoelectrically cooled photomultiplier tube (Thorne EMI 9558b). The output of this unit is transferred to the boxcar averager for further processing. This monochromator is able to scan a wide wavelength range at controlled speeds. The individual steps can be as low as 0.001 nm. This monochromator is controlled through a CD 2A Compudrive unit. A thermoelectrically cooled (upto 50 ^{0}C below room temperature) photomultiplier tube PMT is mounted at the output slits of the monochromator. The light signal detected by the spectrometer is changed into an electrical signal by this photomultiplier. This signal then passes through the preamplifier into the box car averager for further processing.

3.5 Experimental Procedure

A schematic representation of the full experimental setup is shown in figure 3.15.

The calcium atomic vapor was prepared by placing calcium metal granules in the center of the heat pipe oven. However, before introducing calcium granules, the system is baked at 800-900 °C for several hours. In this way we got rid of any impurities which might be present in the heat pipe oven. The calcium is then heated to 350 °C and evacuated to a pressure of 10^{-6} mbar as noted earlier. Then the buffer gas (Argon) was introduced into the heat pipe oven in a controlled manner with a

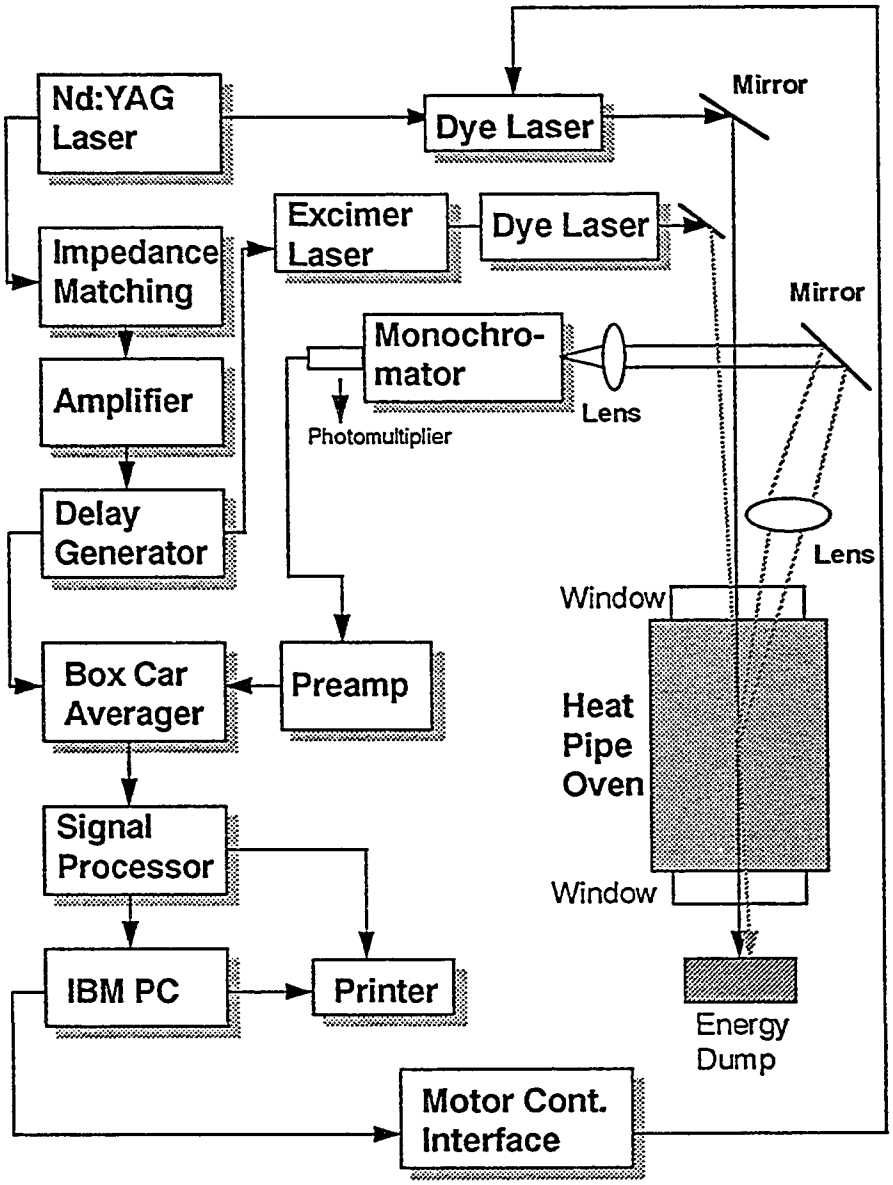

Figure 3.15: Schematic diagram of the experimental setup.

needle valve. The system is then finally heated to the desired temperature of about 720 °C. At this temperature the calcium vapor density is of the order of 10^{15} cm^{-3}.

To observe the emitted signal it is imperative to have a proper control on the timing and triggering sequence between the events, otherwise it may not be possible to observe any signal. In our experimental setup it is necessary to have the signal processing system ready at the time the laser pulse interacted with the calcium vapor, so that the detection would be carried out at the correct time. A 4-channel digital-delay generator (SRS 535) was used for this purpose. It has four outputs which can be time delayed (electronically) with respect to the trigger pulse, which comes usually from the YAG laser as explained earlier. These outputs are utilized for further triggering of excimer laser, box car averager and oscilloscope. In our present experimental setup the time delay between the excimer and the YAG laser was kept around 1-5 μs in order to get the optimum signals.

Chapter 4

Experimental Results

4.1 Introduction

In a series of experiments, several highly excited states of Ca were prepared using the step-wise resonant laser excitation discussed in chapter 3. In particular, 3d4p ($^1D_1$, ^3D), 3d4p ^3F, 4s5p ^3P, 4s5s ^3S states were prepared, one state at a time. The subsequent transfer of population to nearby states 3d4p (^3F, ^1D, ^3P), 4s5p (^1P, ^3P), 4s4d ^3D and $4p^2$ ^3P was monitored through a systematic study of fluorescence from these states. Measurements included spectrally resolved fluorescence and time-resolved spectra, where the rise time as well as fall time of fluorescence signal were measured. Furthermore, measurements were made at high Argon pressures as well as at low Ar pressures as discussed below. Figure 4.1 shows a partial energy level diagram for calcium, showing the laser prepared states and the levels populated by collisional transfer with buffer gas atoms. This looks too detailed and complicated because all the transitions investigated have been displayed. However, in individual

experiments, only one specific state is prepared by the lasers and only a few dominant transfer channels are investigated as discussed later in this chapter. Laser 1 prepared the $4s4p\,^3P_1$ state through resonant pumping of the $4s^2\,^1S_0 \rightarrow 4s4p\,^3P_1$ transition at 6572.78 Å with Rhodamine 101 dye dissolved in methanol. Transfer of atoms to $4s3d\,^3D$ states occured through collisional energy transfer i.e. collisional energy pooling between excited atoms, as well as the Ar-supported collision cascade particularly from $4s4p\,^1P_1$ state [2, 8, 17, 18, 19, 78]. Laser 2 subsequently pumped the population of individual components of the $4s4p\,^3P$ states or $4s3d\,^3D$ states to some higher energy states through resonant absorption.

4.2 Energy Transfer Through Collisions

Collisions between excited atoms including energy pooling collisions [68, 79, 80, 81, 82, 83], associative ionization [84, 85], and Penning ionization [86, 87] can have high rate coefficients. However, associative ionization and Penning ionization have not been investigated in any significant detail in the case of Ca. Energy pooling collision, on the other hand, have been reported in two previous papers [79, 88]. A further class of collisions involves two atoms where only one of them is in an excited state. The total exchange of energy is limited to the thermal energies of the collision partners. These are a special class of the so called "Thermal Collisions" and can also have large rate coefficients. Here the product state is usually a state lying nearby on the energy scale and can be easily investigated through a study of fluorescence. We are primarily interested in collisions with Ar used here as a buffer gas.

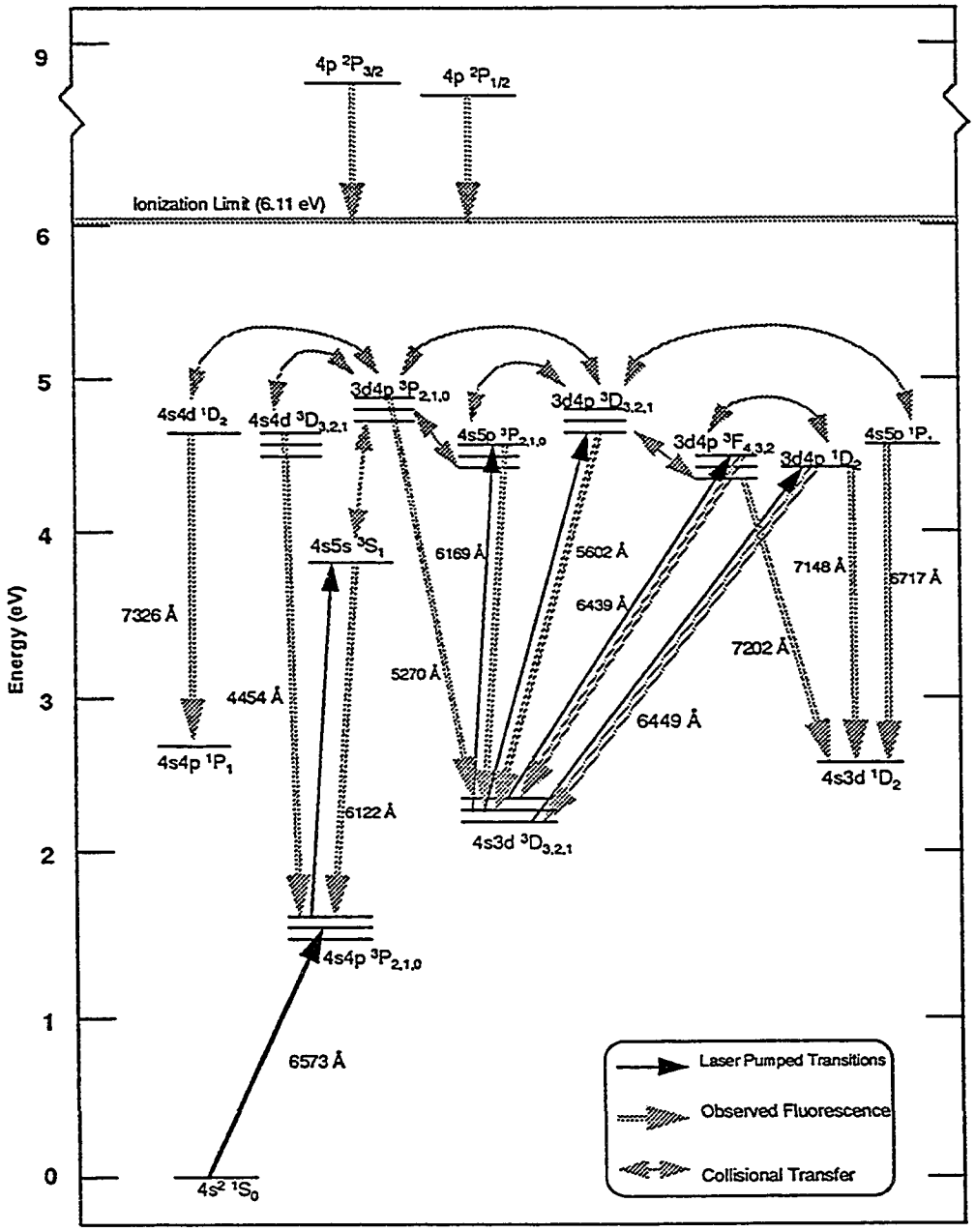

Figure 4.1: A simplified energy level diagram for calcium, showing the laser prepared states together with the levels populated by collision and important radiative pathways.

	Product States						
Parent States↓	$3d4p\ ^3F_2$	$4s5p\ ^1P_1$	$4s4d\ ^3D_3$	$4s4d\ ^1D_2$	$3d4p\ ^3P_2$	$4s5p\ ^3P_2$	$3d4p\ ^1D_2$
$3d4p\ ^1D_2$	104.959	896.202	1922.036	1462.874	3504.667	739.71	0
$3d4p\ ^3F_4$	166.435	834.726	1860.56	1401.398	3443.191	678.23	61.476
$4s5p\ ^3P_2$	844.67	156.5	1182.33	723.17	2764.96	0	739.71
$3d4p\ ^3D_1$	2461.938	1460.777	434.943	894.105	1147.688	1617.273	2356.979
$4s5s\ ^3S_1$	4190.959	5192.12	6217.954	5758.792	7800.585	5035.624	4295.918

Table 4.1: Energy defect (cm^{-1}) between the parent and the product state.

The energy defects[1] (cm^{-1}) between the laser prepared parent (first column) and the product states (first row) are given in Table 4.1. We did not observe any significant transfer to nearby and possible product states when the 4s5s $^3S_1$ parent state was prepared by the step-wise laser excitation process. This is probably due to the reason that the energy defect between this particular parent state and the possible product states is relatively large (last row) as compared to the energy defects between the other parent and product states.

4.3 A Broad Overview of Strong Collision Channels

As a first step, it is important to identify strong collision channels where the collisions result in a large transfer of excitation energy (population) to other atomic states. This can be done through a systematic study of relative intensities of fluorescence. This is very useful, in the present case, in the sense that only these channels are investigated

[1] All values from Reference [89].

in order to extract information on rate coefficients. A summary of the measured intensities for various transitions of Ca I and also one transition of Ca II at 3933 Å, when different selected states (taken one at a time) were prepared by the step-wise laser excitation is given in Table 4.2. The corresponding bar graph is shown in Fig 4.2. Here the oven temperature was 725 ^{0}C with 16 mbar Ar pressure. Although the intensities are not corrected for the response of the photomultiplier, we get a clear idea of dominant collision channels. Once again, in the text hereafter we will refer to the states prepared by the step-wise laser excitation process as the "parent" state and the upper states of the transitions populated by collisional transfer from the parent state as the "product" states.

		Parent States			
Transition	λ (Å)	3d4p $^1D_2$	3d4p $^3F_4$	3d4p $^3D_1$	4s5p $^3P_2$
$4p\ ^2P_{3/2} \rightarrow 4s\ ^2S_{1/2}$	3933	18.75	1.58	1.36	1.64
$4p^2\ ^3P_2 \rightarrow 4s4p\ ^3P_2$	4302	4.72	6.1	54.57	3.76
$4s4d\ ^3D_3 \rightarrow 4s4p\ ^3P_2$	4454	17.41	27.37	52.8	26.88
$3d4p\ ^3P_2 \rightarrow 4s3d\ ^3D_3$	5270	5.23	5.73	29.02	lost
$4s5p\ ^3P_2 \rightarrow 4s3d\ ^3D_3$	6169	16.23	29.61	10.37	0
$4s5p\ ^1P_1 \rightarrow 4s3d\ ^1D_2$	6717	3.78	7.83	5.83	9.1
$3d4p\ ^1D_2 \rightarrow 4s3d\ ^1D_2$	7148	12.98	17.22	5.05	14.96
$3d4p\ ^3F_2 \rightarrow 4s3d\ ^1D_2$	7202	8.73	12.12	2.89	12.9
$4s4d\ ^1D_2 \rightarrow 4s4p\ ^1P_1$	7326	1.16	3.5	4.07	2.9

Table 4.2: Intensities (arbitrary units) of various transitions observed when different parent states were prepared.

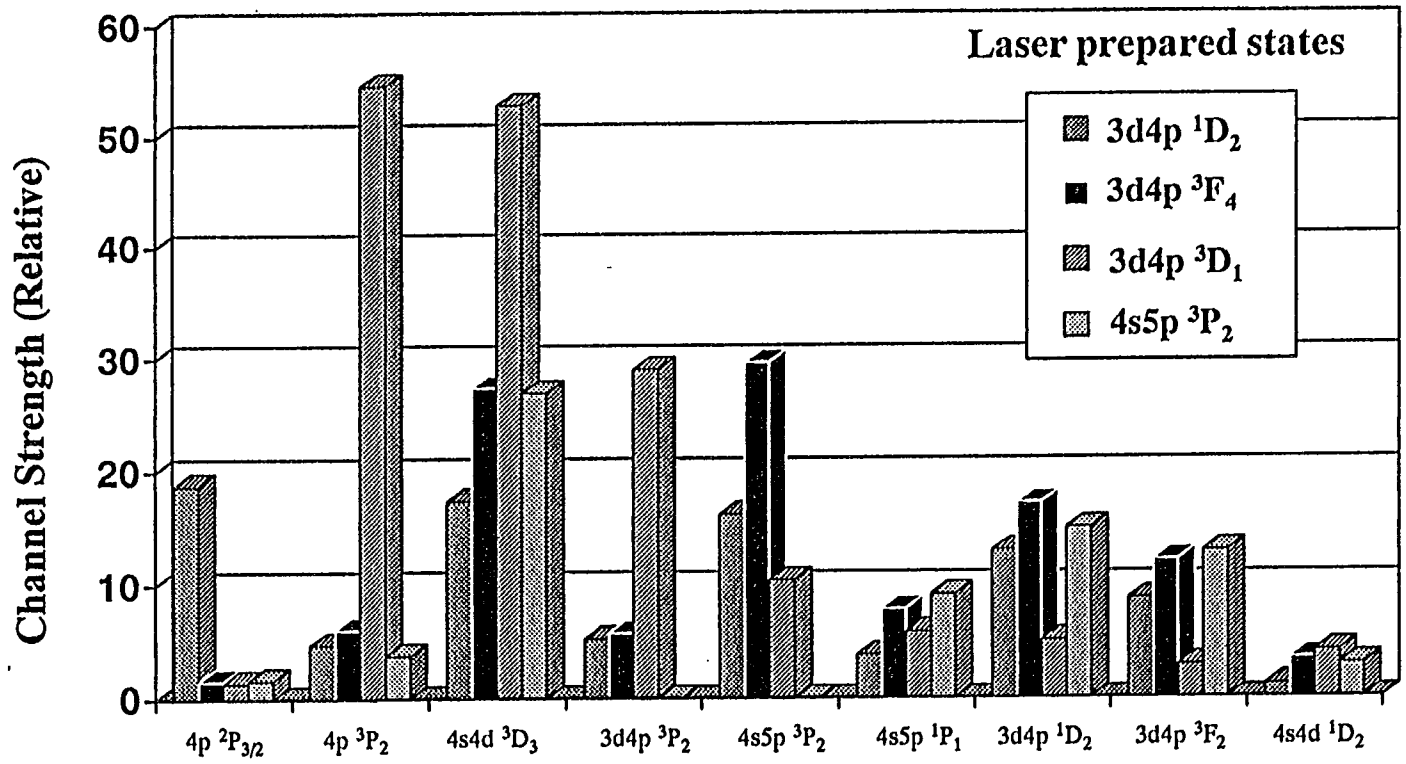

Figure 4.2: Relative intensities emitted from the upper states of the fluorescing transitions when different parent states were prepared by the second laser as indicated in the legend.

4.4 Time-Resolved Kinetics

In an attempt to investigate the total deactivation rate constants of the parent states, we recorded the time-resolved fluorescence from these states. Figure 4.3 shows an example of the time resolved emissions from the 3d4p $^1D_2$ state (3d4p $^1D_2 \rightarrow$ 4s3d $^1D_2$) at 7148 Å when the oven temperature was 725 ^{0}C.

In order to obtain a good estimate of the rise and the fall times of the signal, a 50 Ω termination was used here instead of the $1M\Omega$ termination. For example, the population in the 3d4p $^1D_2$ state apparently reaches a peak in about 11 ns while the collapse of its population occurs in about 50 ns (Figure 4.3). The total deactivation rate constants are derived from the Stern-Volmer plots [20], as illustrated in Figures 4.4 to 4.6, where the rare gas density is kept sufficiently low to ensure linear plots.

4.4.1 Parent State $3d4p\ ^1D_2$

Figure 4.4 shows the decay rates for the transition 3d4p $^1D_2 \rightarrow$ 4s3d $^1D_2$ at 7148 Å as a function of Ar density when the 3d4p $^1D_2$ parent state was prepared by the second laser at 6449 Å with the help of the step-wise laser excitation process. From the slope of this linear plot we get the total quenching rate K_d of the parent state. The observed rate is $K_d = 6.66 \times 10^{-11}\ cm^3/\text{sec}$ as indicated on the graph.

4.4.2 Parent State $3d4p\ ^3F_2$

The decay rates for the transition 3d4p $^3F_2 \rightarrow$ 4s3d $^1D_2$ at 7202 Å as a function of Ar density, when the 3d4p $^3F_2$ parent state was prepared by the second laser at 6493 Å are shown in Figure 4.5. From the slope of this linear plot we get the total quenching

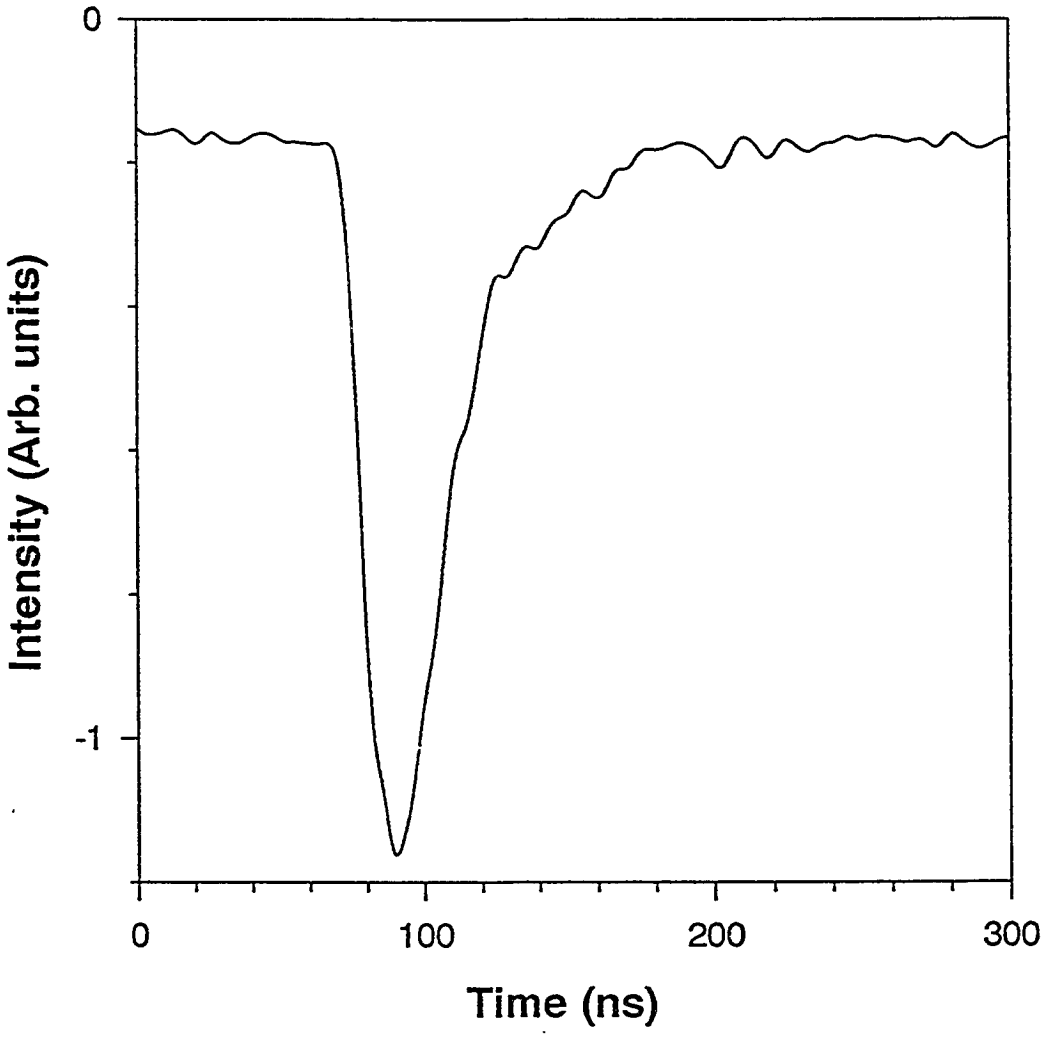

Figure 4.3: Time resolved fluorescence traces of the 3d4p $^1D_2 \rightarrow$ 4s3d $^1D_2$ transition at 7148 Å, with 70 mbar Ar pressure.

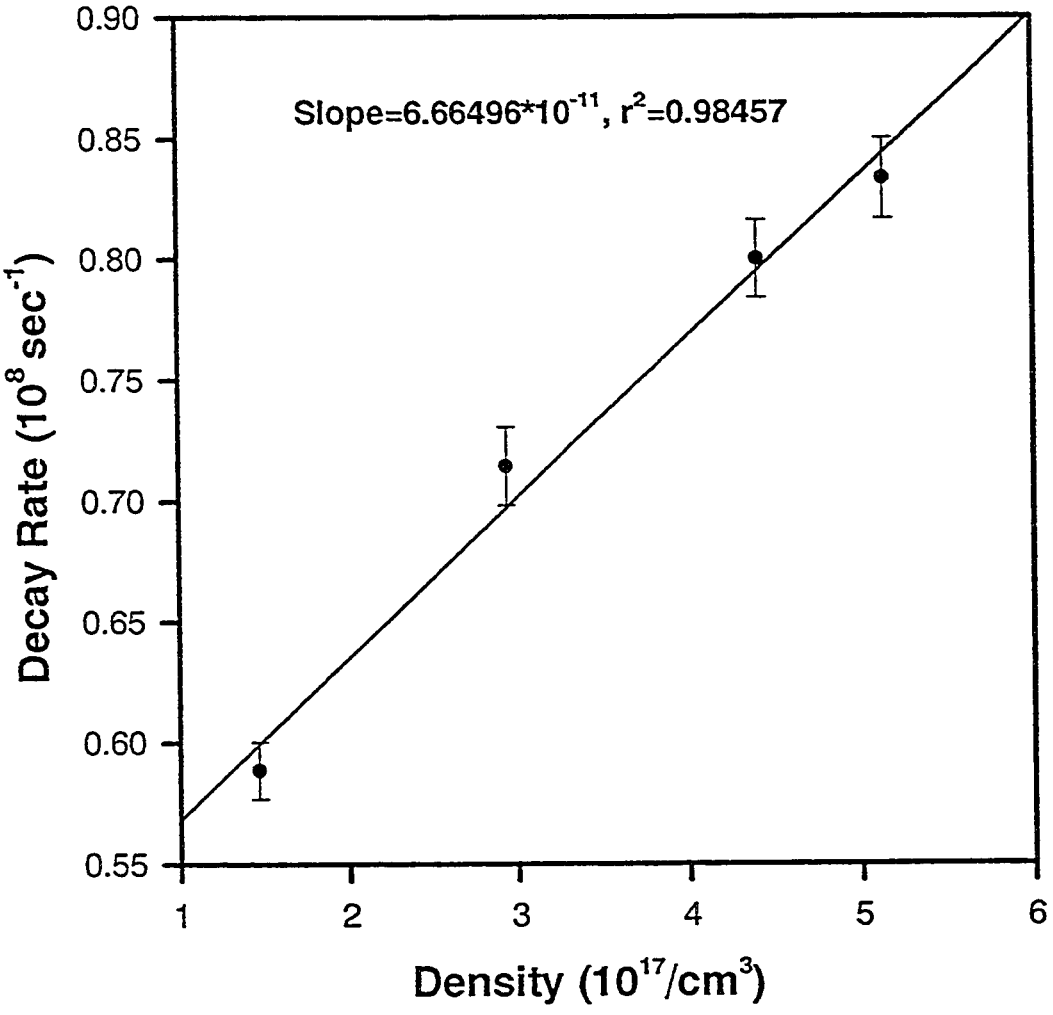

Figure 4.4: Deactivation plot for the transition 3d4p $^1D_2 \rightarrow$ 4s3d $^1D_2$ at 7148 Å.

rate $K_d = 10.12 \times 10^{-11}\ cm^3/\text{sec}$.

4.4.3 Parent State $3d4p\ ^3D_1$

Similarly the total decay rates for the transition 3d4p $^3D_1 \rightarrow$ 4s3d $^3D_1$ at 5598 Å as a function of Ar density are shown in Figure 4.6. Here, the parent state was excited by the second laser at 5602 Å. The slope gives a total quenching rate of $K_d = 6.45 \times 10^{-11}$ cm^3/sec.

Time-resolved emission from other parent states could not be investigated because suitable transitions (other than the laser pumped transitions) originating from these states which could be recorded in the 3000 - 8000 Å region with relative ease, were not available. Table 4.3 summarizes the results on total quenching rates for the parent states discussed above.

Parent State	K_d (cm^3 sec^{-1})
$3d4p\ ^3F_2$	10.12×10^{-11}
$3d4p\ ^1D_2$	6.66×10^{-11}
$3d4p\ ^3D_1$	6.45×10^{-11}

Table 4.3: Total quenching rates for the parent states.(see text for further explanation)

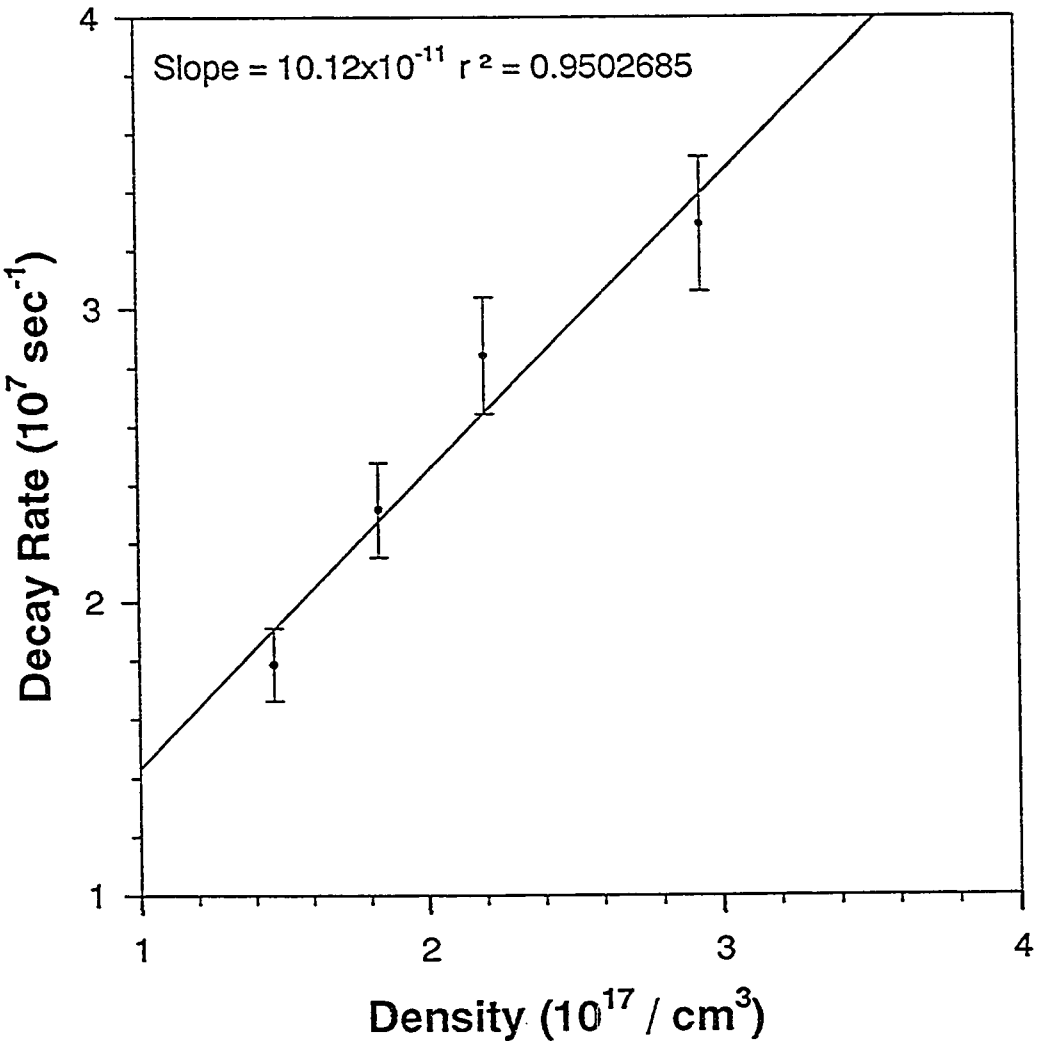

Figure 4.5: Deactivation plot for the transition 3d4p $^3F_2 \rightarrow$ 4s3d $^1D_2$ at 7202 Å.

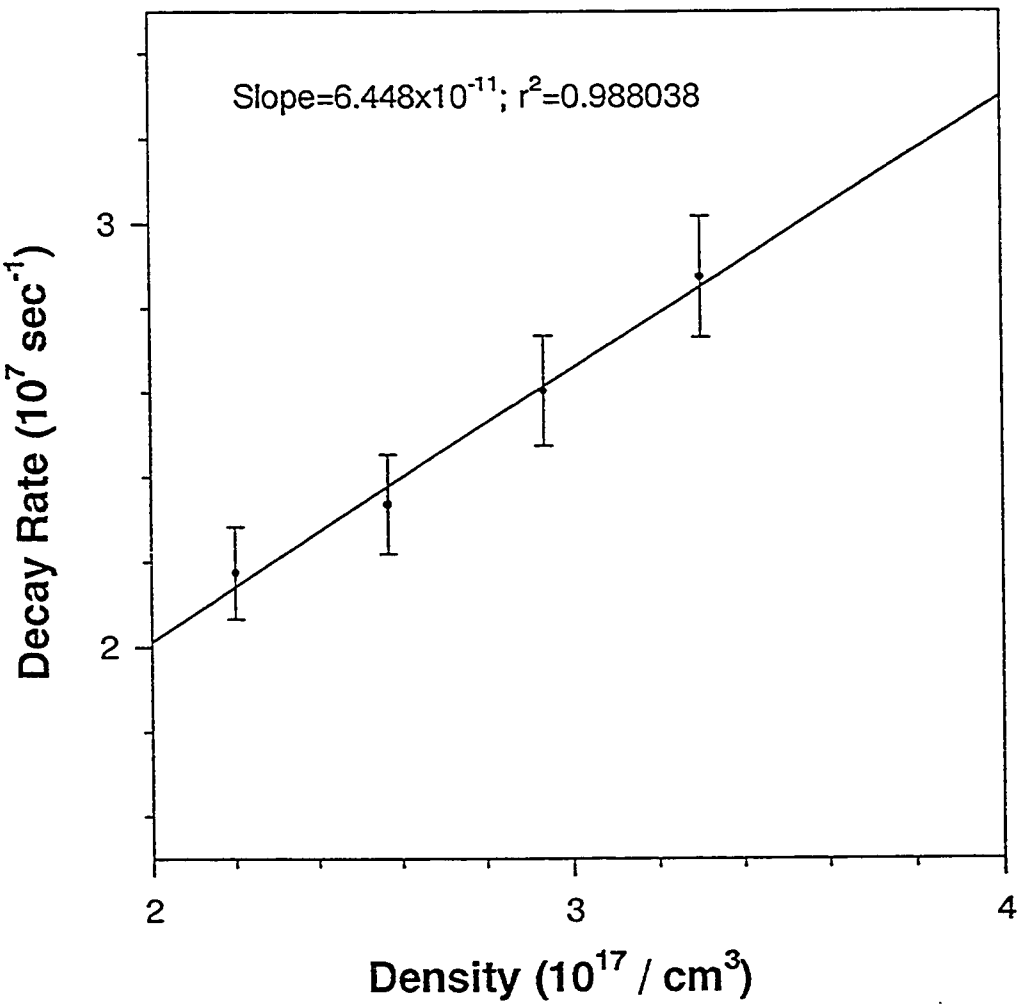

Figure 4.6: Deactivation plot for the transition 3d4p $^3D_1 \rightarrow$ 4s3d $^3D_1$ at 5598 Å.

4.5 Wavelength-Resolved Spectra

In order to determine the population distribution of the near-by states populated by Ar-supported collisional transfer, and the individual rate constants for the transfer, wavelength-resolved emission spectra were recorded with a boxcar averager. Fluorescence was imaged onto the slit of a monochromator using an off axis mirror and an off-axis lens as explained in chapter 3 above. The monochromator slit width was kept at 130 μm to obtain a good signal at a reasonable resolution. The dispersed fluorescence from the 1200 groves per mm grating was directed onto the exit slits and then to the photomultiplier tube. This provided the records of the fluorescence emission from various states of Ca. The Signal processor Model 4402 with our boxcar enables us to integrate the intensities within each transition in the wavelength-resolved spectra. Theses intensities can then be related to the state-to-state rate constant by means of Eq. 2.30. Thus the S_i in Eq. 2.30 refers to the signal voltage integrated over the wavelength. Figure 4.7 shows a typical signal from a fluorescing transition as recorded by the boxcar averager. The area under this curve is taken to be proportional to the intensity of the fluorescing transition. Here the monochromator was scanned around 7196 - 7247.34 Å covering the expected region of the transition 3d4p $^3F_2 \rightarrow$ 4s3d $^1D_2$ of Ca I. Also to be noted here is that the intensities appear negative. This is because of the photomultiplier signal, which is negative. The area under this curve is then taken as the intensity of the emitted signal.

Figures 4.8 to 4.10 show typical examples of signals from several fluorescing transitions in the 6436Å to 6487.34Å as recorded by the boxcar averager when the Ar

λ(Å)	Transition
6439.073	$3d4p\ ^3F_4 \rightarrow 4s3d\ ^3D_3$
6449.810	$3d4p\ ^1D_2 \rightarrow 4s3d\ ^3D_1$
6455.600	$3d4p\ ^1D_2 \rightarrow 4s3d\ ^3D_2$
6462.566	$3d4p\ ^3F_3 \rightarrow 4s3d\ ^3D_2$
6471.660	$3d4p\ ^3F_3 \rightarrow 4s3d\ ^3D_3$

Table 4.4: The actual transitions corresponding to different lines in Figures 4.8 to 4.10.

pressure was 10, 20 and 40 mbar respectively. Here the parent state prepared was $4s5p\ ^3P_2$. Note that the vertical scales are different in these diagrams. The change in the intensity with increasing Ar pressure is clearly noticeable. Table 4.4 shows the actual transitions corresponding to different lines in these diagrams. In our studies, for each parent state, we investigated the variation in the intensity of individual transitions as a function of Ar pressure.

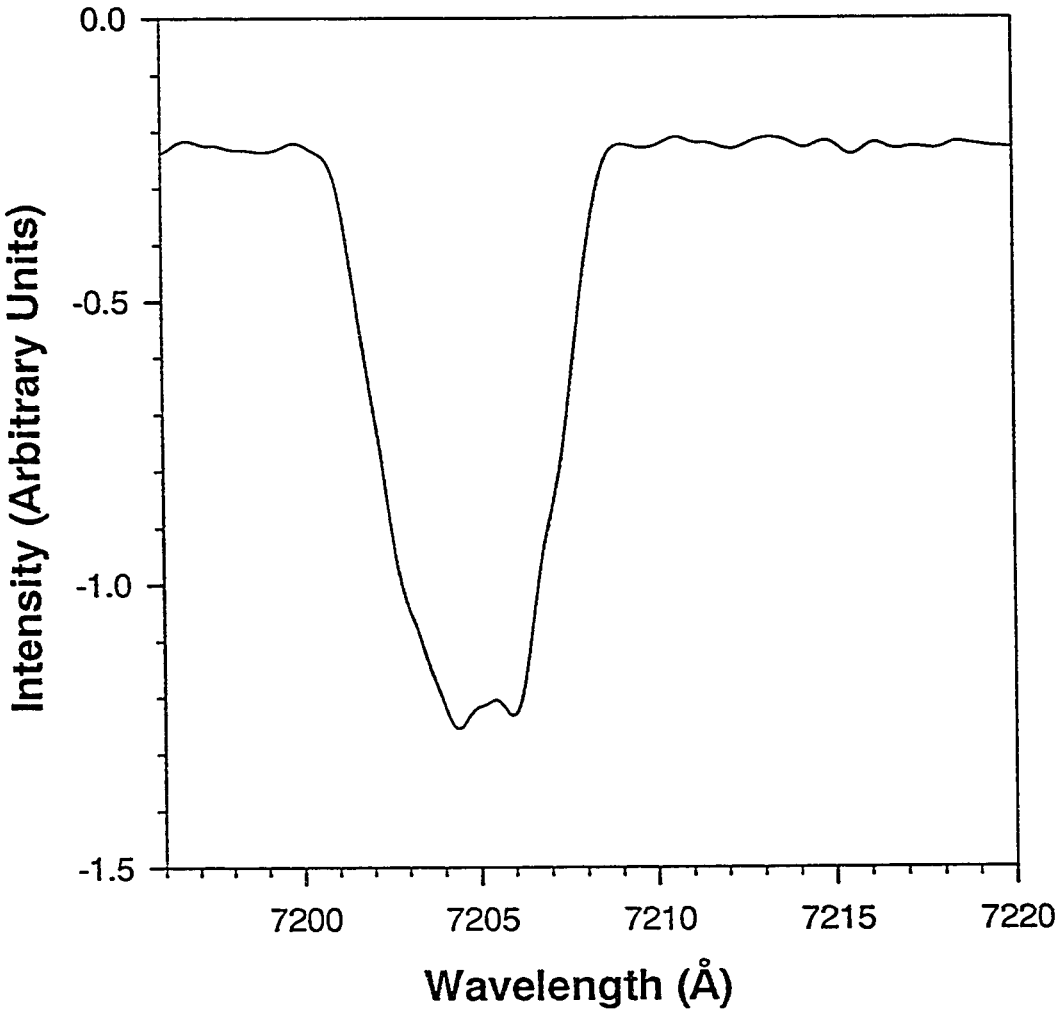

Figure 4.7: A typical spectrum of the 3d4p $^3F_2 \rightarrow$ 4s3d $^1D_2$ transition of Ca I at 7202Å.

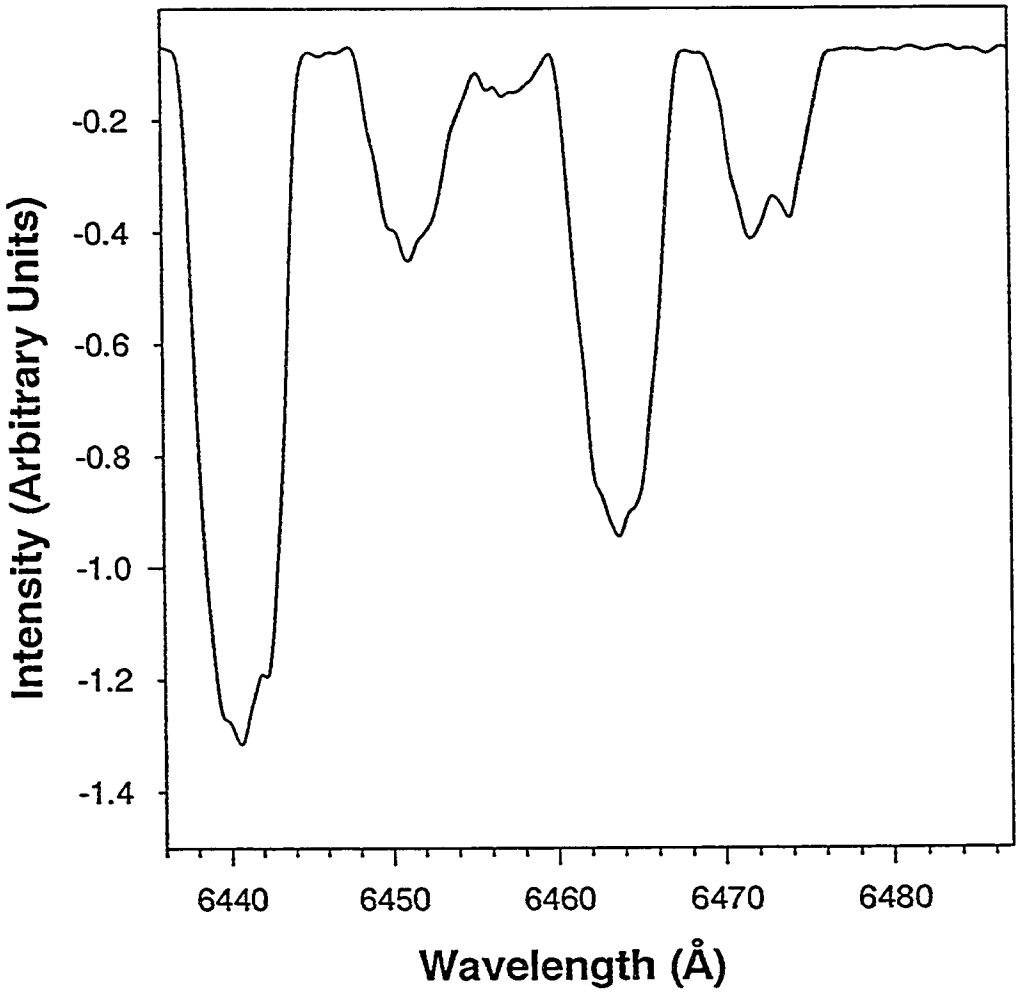

Figure 4.8: Fluorescent spectrum in the 6436 to 6487.34Å region when the $4s5p\ ^3P_2$ state was prepared by step-wise excitation. Here the Ar pressure was 10 mbar.

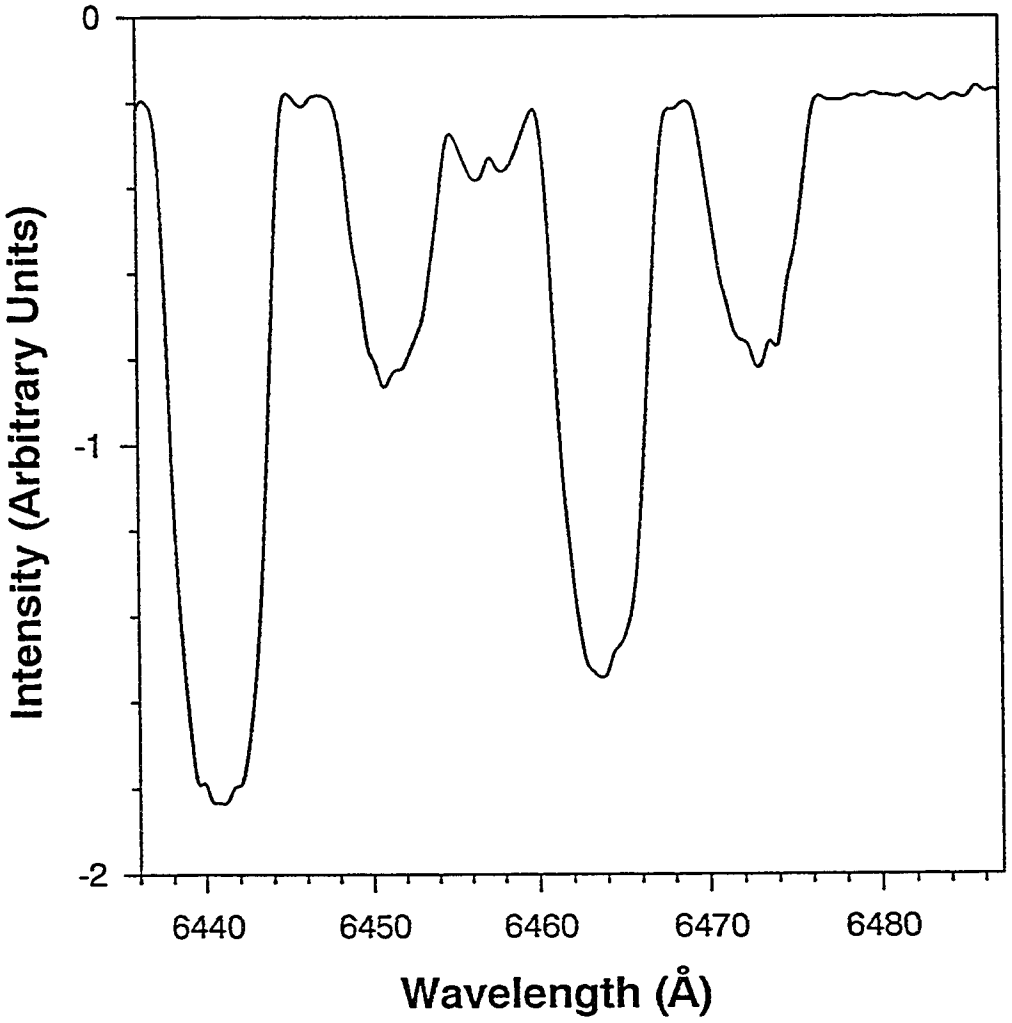

Figure 4.9: Fluorescent spectrum in the 6436 to 6487.34Å region when the $4s5p\ ^3P_2$ state was prepared by step-wise excitation. Here the Ar pressure was 20 mbar.

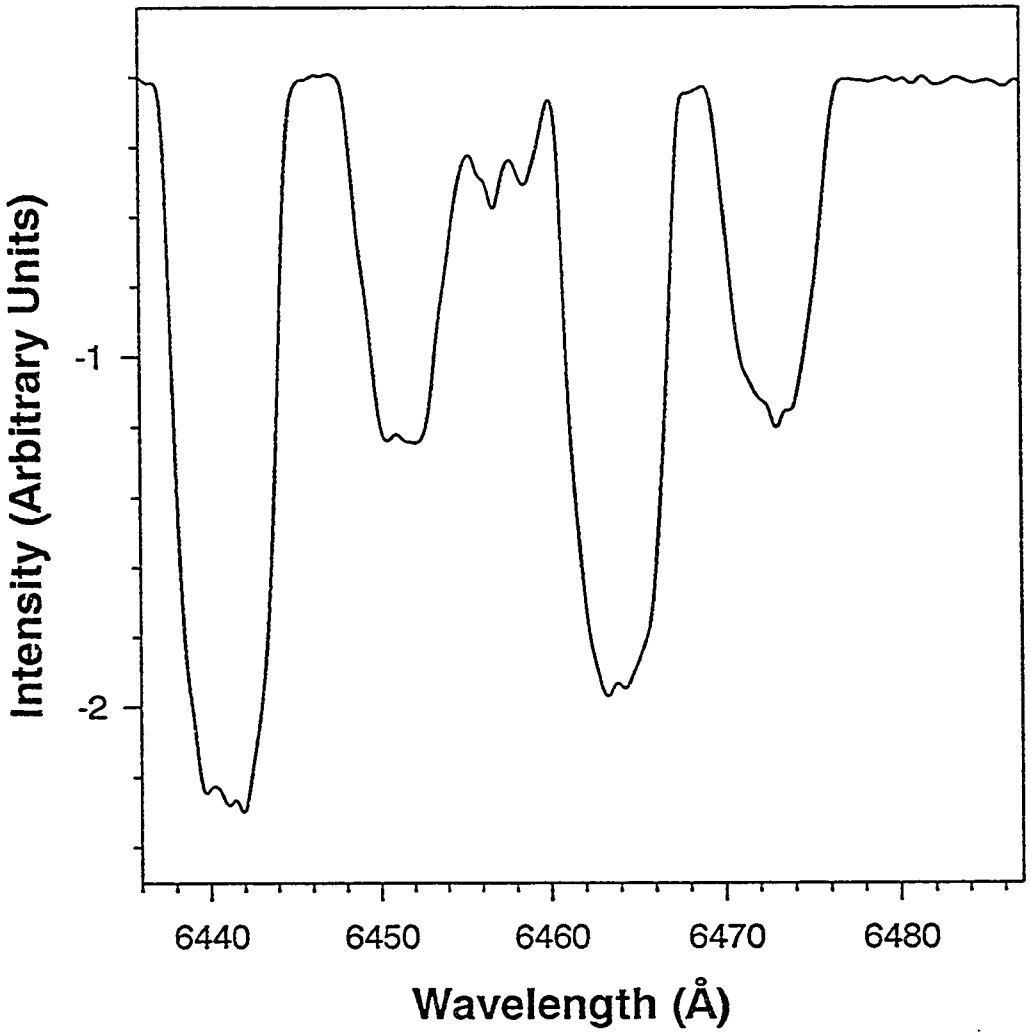

Figure 4.10: Fluorescent spectrum in the 6436 to 6487.34Å region when the $4s5p\ ^3P_2$ state was prepared by step-wise excitation. Here the Ar pressure was 40 mbar.

In the study of the general behavior of intensities of selected emission lines as a function of Ar density. The density was kept sufficiently low to ensure linear plots. This is because at low Ar densities the upper "product" state of the fluorescing transition essentially decays directly to the lower state through spontaneous radiative emission, while at high Ar densities a very substantial collisional back transfer of the upper state can also occur. These graphs represent an intermediate result for the determination of the state-to-state rate constants, which will be discussed in section 4.6. We discuss the case of individual parent states here below.

4.5.1 Parent State $3d4p\ ^1D_2$

Fig 4.11 shows the 3d4p $^1D_2$ as the parent state prepared by the step-wise excitation. The collisional transfer to other nearby states and the wavelengths of the transitions on which fluorescence was observed are also shown. Figures 4.12 to 4.15 show the intensity for different transitions (indicated on each graph) of calcium as a function of Ar density when the 3d4p $^1D_2$ parent state was prepared by the step-wise excitation. The linearity of the fit is an indication of the acceptability of the approximations considered. However, since the exact response function and the geometrical factors are not known, we have adapted a technique involving relative intensities in order to recover the state-to-state rate coefficients as discussed in chapter 2.

The intensity behavior of the 4s5p $^1P_1 \rightarrow$ 4s3d $^1D_2$ transition at 6717 Å at different Argon densities is shown in Figure 4.12. Here, the slope is 1.64×10^{-18} which is in fact related to the required rate coefficient. Similarly, the intensity behavior of the 3d4p $^3F_2 \rightarrow$ 4s3d $^1D_2$ transition at 7202 Å at different Argon densities is illustrated

in Figure 4.13. The value of the slope is 4.51×10^{-18}. The intensity behavior of the 4s5p $^3P_1 \rightarrow$ 4s3d $^3D_2$ transition at 6169 Å as a function of Ar density is shown in Fig 4.14. The corresponding slope is 8.49×10^{-18} . Likewise The intensity behavior of the 3d4p $^1D_2 \rightarrow$ 4s3d $^1D_2$ transition at 7148 Å as a function of Ar density is shown in Fig 4.15. The corresponding slope is 2.69×10^{-17}.

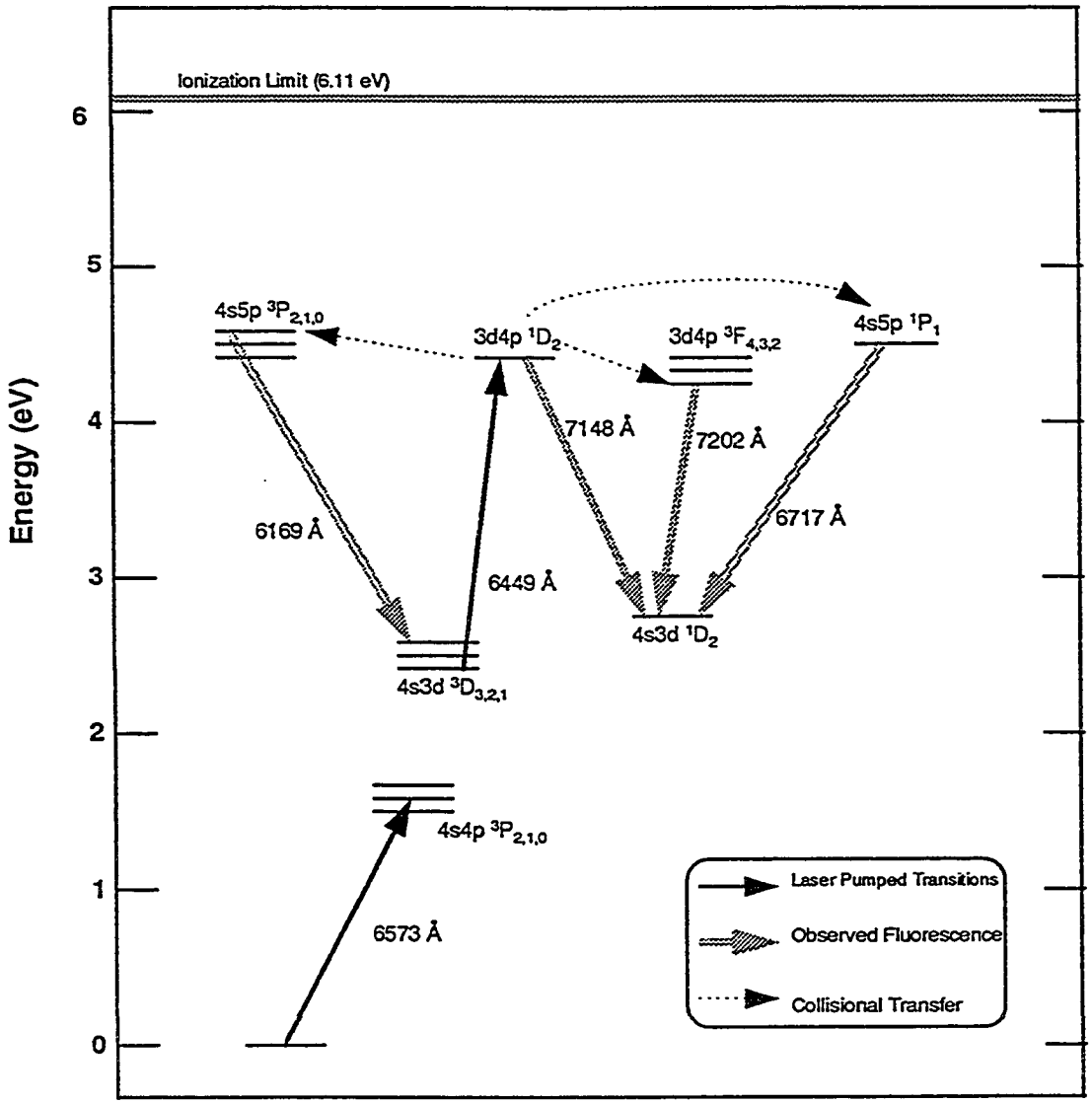

Figure 4.11: Partial energy level diagram for the calcium atom showing the laser - excited 3d4p $^1D_2$ state, the predominant product states (4s5p $^3P_1$, 3d4p $^3F_2$, 4s5p $^1P_1$) populated by collisions with Argon, and fluorescent transitions observed.

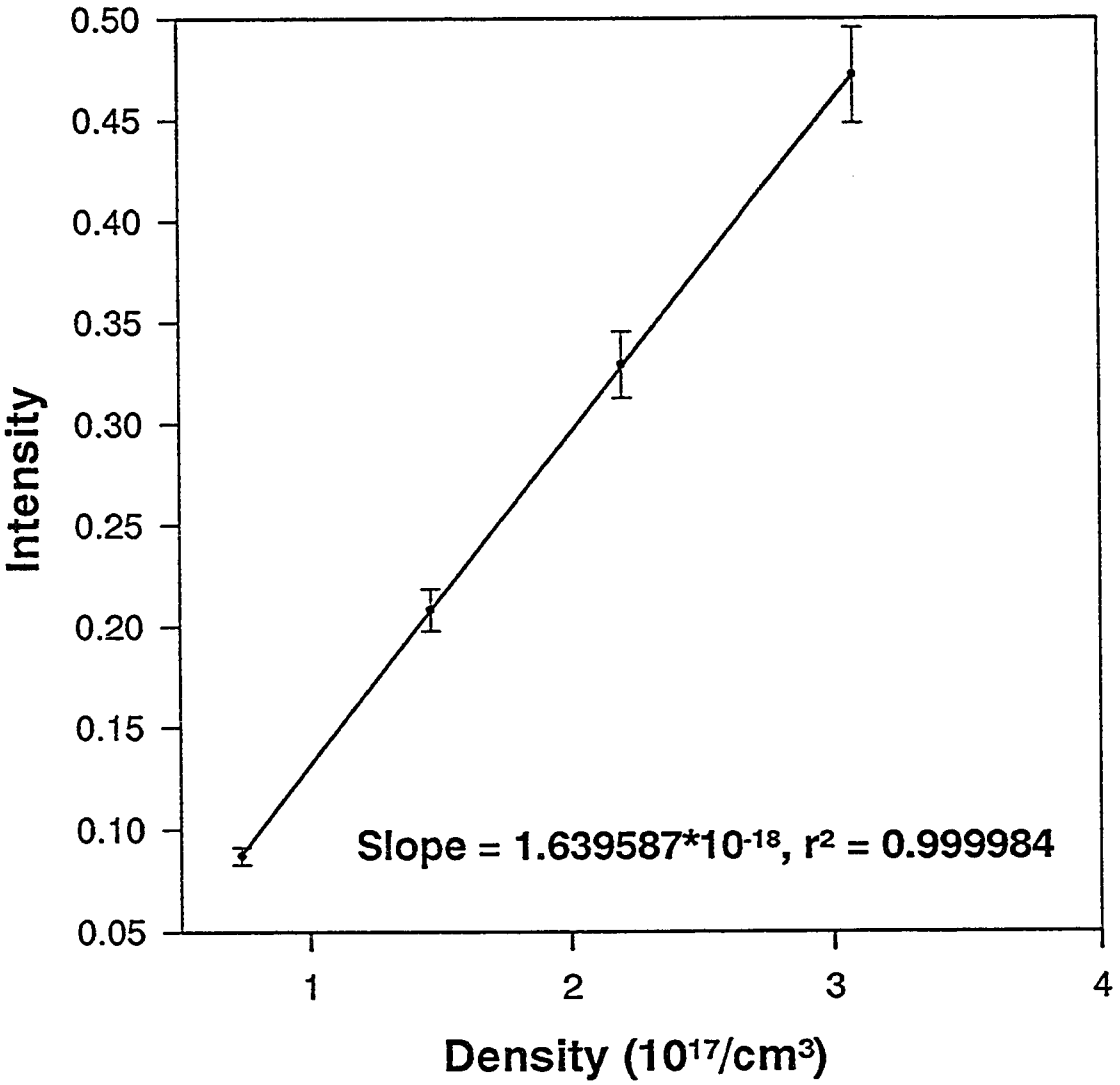

Figure 4.12: Fluorescence yield from the 4s5p $^1P_1 \rightarrow$ 4s3d $^1D_2$ at 6717 Å at different Argon densities, when the 3d4p $^1D_2$ state of calcium was prepared with the help of the step-wise laser excitation process.

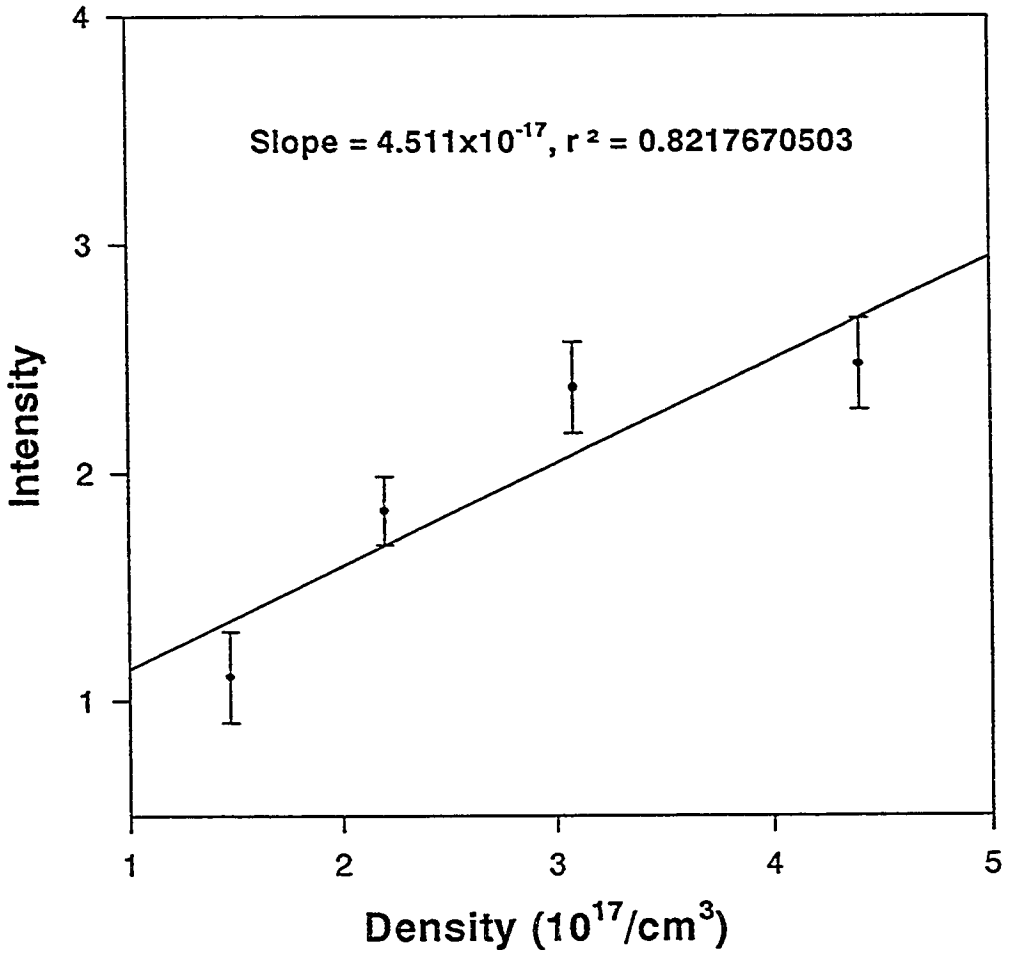

Figure 4.13: Fluorescence yield from the 3d4p $^3F_2 \rightarrow$ 4s3d $^1D_2$ at 7202 Å at different Argon densities, when the 3d4p $^1D_2$ state of calcium was prepared with the help of the step-wise laser excitation process.

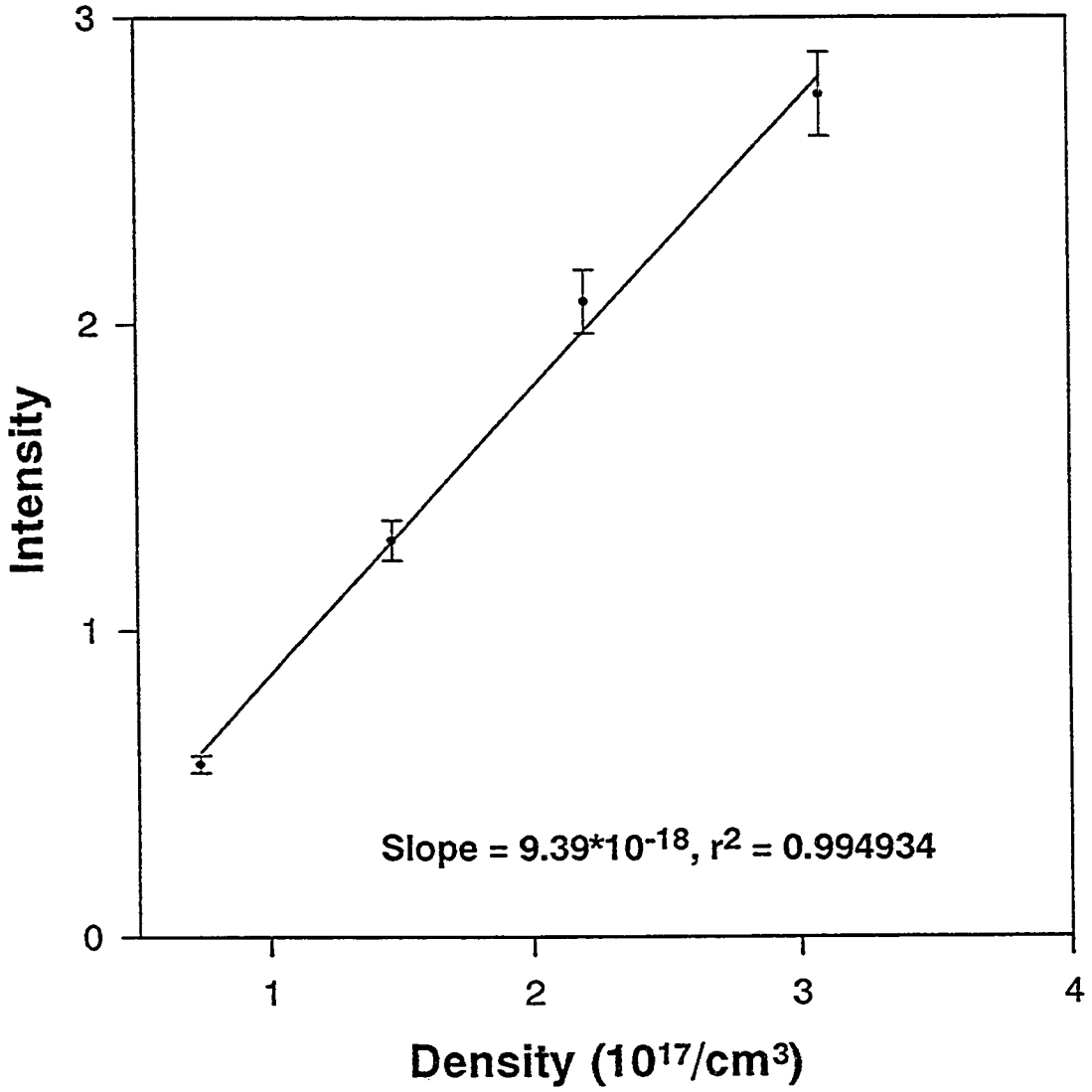

Figure 4.14: Fluorescence yield from the 4s5p $^3P_2 \rightarrow$ 4s3d $^3D_2$ at 6169 Å at different Argon densities, when the 3d4p $^1D_2$ state of calcium was prepared with the help of the step-wise laser excitation process.

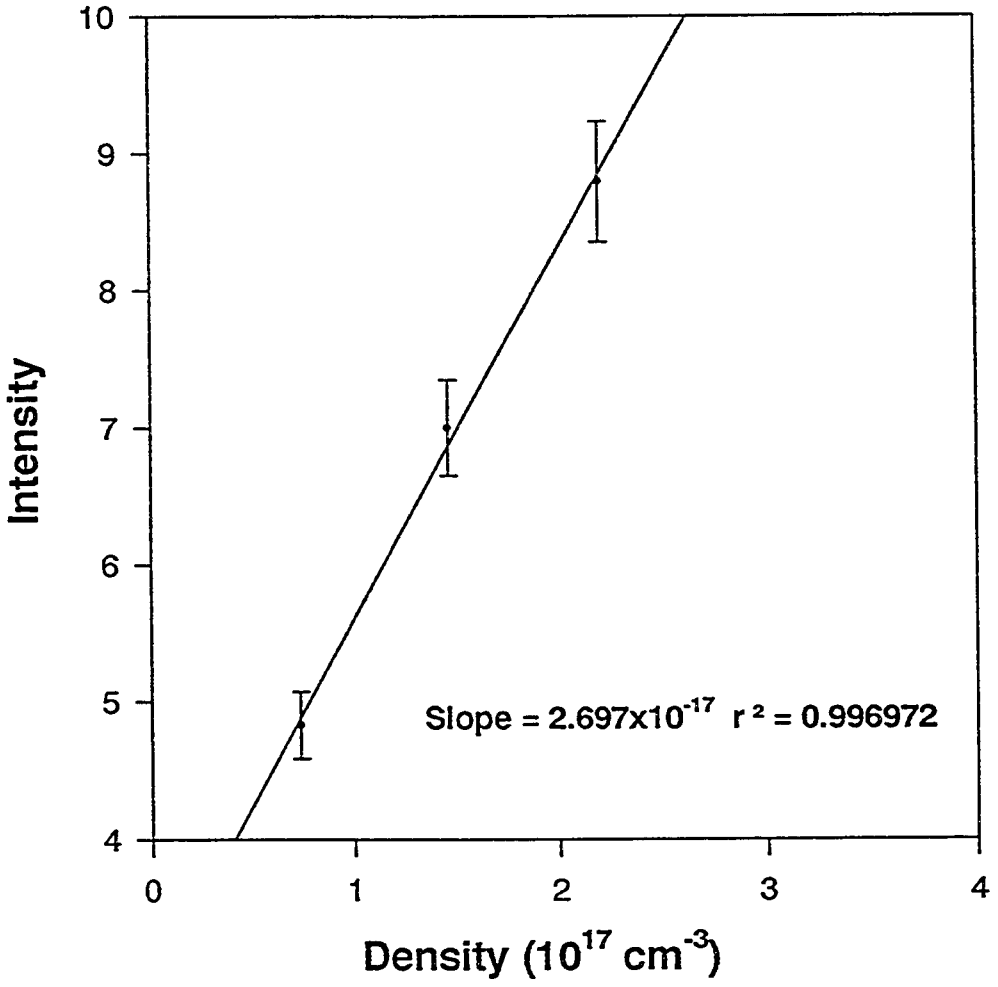

Figure 4.15: Fluorescence yield from the 3d4p $^1D_2 \rightarrow$ 4s3d $^1D_2$ at 7148 Å at different Argon densities, when the 3d4p $^1D_2$ state of calcium was prepared with the help of the step-wise laser excitation process.

4.5.2 Parent State $3d4p\ ^3F_4$

Fig 4.16 shows the 3d4p $^3F_4$ state as the parent state, the predominant product states (4s5p $^3P_1$, 3d4p $^1D_2$, 4s5p $^1P_1$) populated by collisions with Argon, and fluorescent transitions observed. Figures 4.17 to 4.21 show the pressure versus the intensity plots for selected transitions, when the 3d4p $^3F_4$ parent state was prepared by the second laser.

The intensity behavior of the 3d4p $^3F_2 \rightarrow$ 4s3d $^1D_2$ transition at 7202 Å as a function of Ar density is shown in Fig 4.17. The corresponding slope is 7.96×10^{-18}. Likewise, the intensity behavior of the 4s5p $^1P_1 \rightarrow$ 4s3d$^1D_2$ transition at 6717 Å as a function of Ar density is illustrated in Fig 4.18. The corresponding slope is 3.17×10^{-18}. The intensity behavior of the 3d4p $^1D_2 \rightarrow$ 4s3d $^1D_2$ transition at 7148 Å as a function of Ar density is shown in Fig 4.19. The corresponding slope is 1.02×10^{-17}.

4.5.3 Parent State $3d4p\ ^3F_2$

The intensity behavior of the 3d4p $^1D_2 \rightarrow$ 4s3d $^1D_2$ at 7148 Å as a function of Ar density when the 3d4p $^3F_2$ state was prepared is shown in Fig 4.20. The corresponding slope is 2.04×10^{-16}. Similarly the intensity behavior of the 3d4p $^3F_2 \rightarrow$ 4s3d $^1D_2$ at 7202 Å as a function of Ar density when the 3d4p $^3F_2$ state was prepared is shown in Fig 4.21. The corresponding slope is 6.07×10^{-16}.

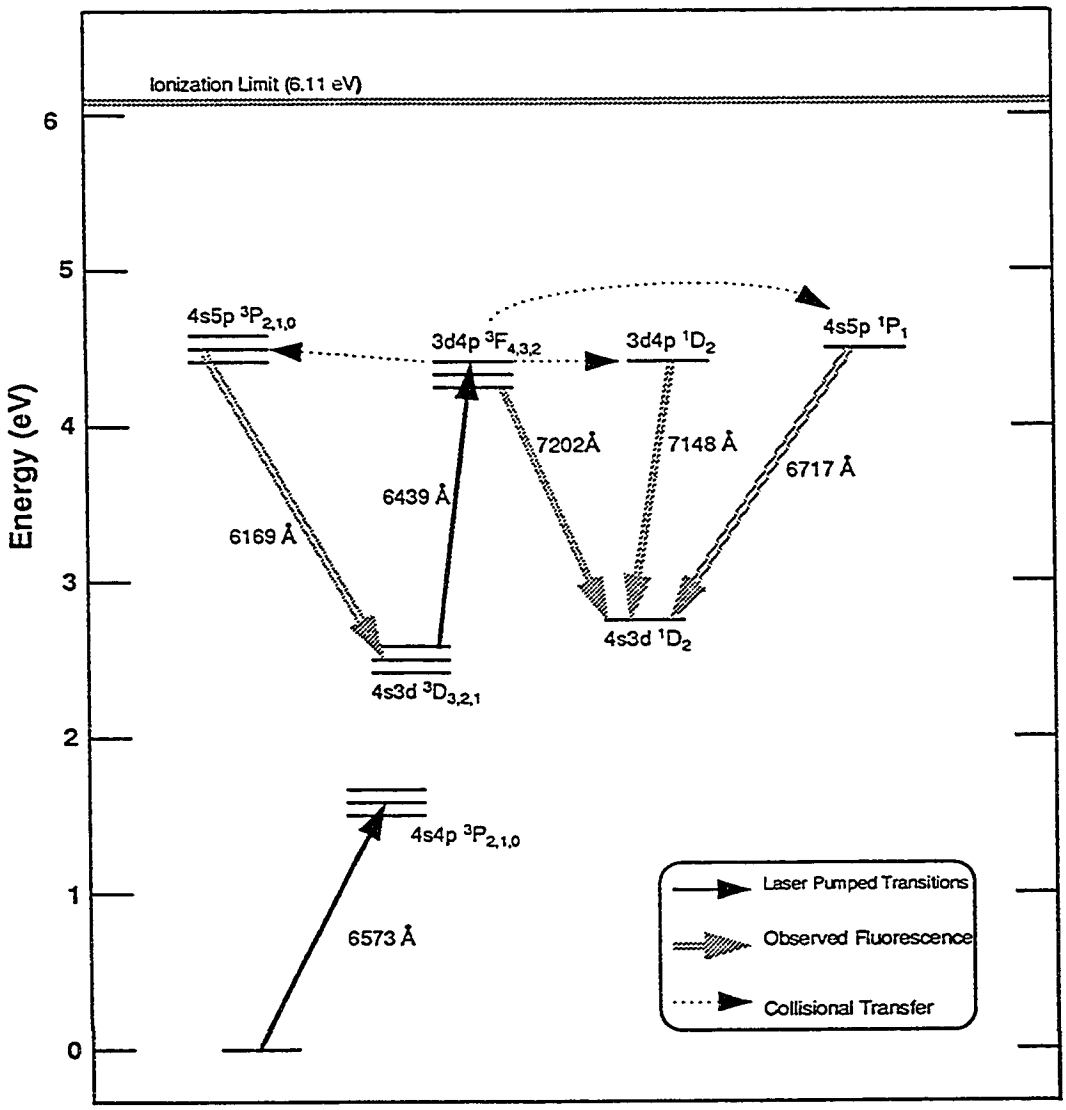

Figure 4.16: Partial energy level diagram for the calcium atom showing the laser - excited 3d4p $^3F_4$ state, the predominant product states (4s5p $^3P_1$, 3d4p $^1D_2$, 4s5p $^1P_1$) populated by collisions with Argon, and fluorescent transitions observed.

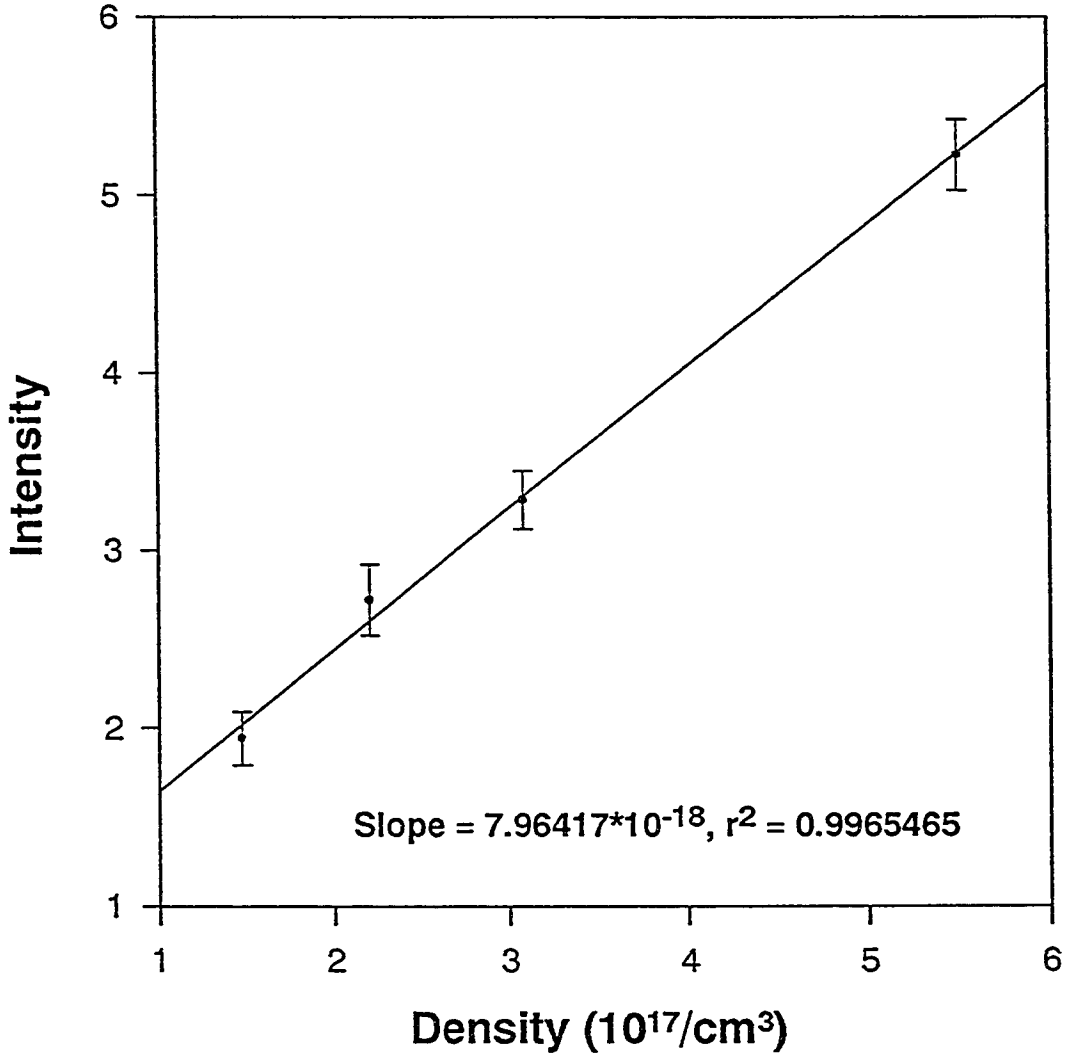

Figure 4.17: Fluorescence yield from the 3d4p $^3F_2 \rightarrow$ 4s3d $^1D_2$ at 7202 Å at different Argon densities, when the 3d4p $^3F_4$ state of calcium was prepared with the help of the step-wise laser excitation process.

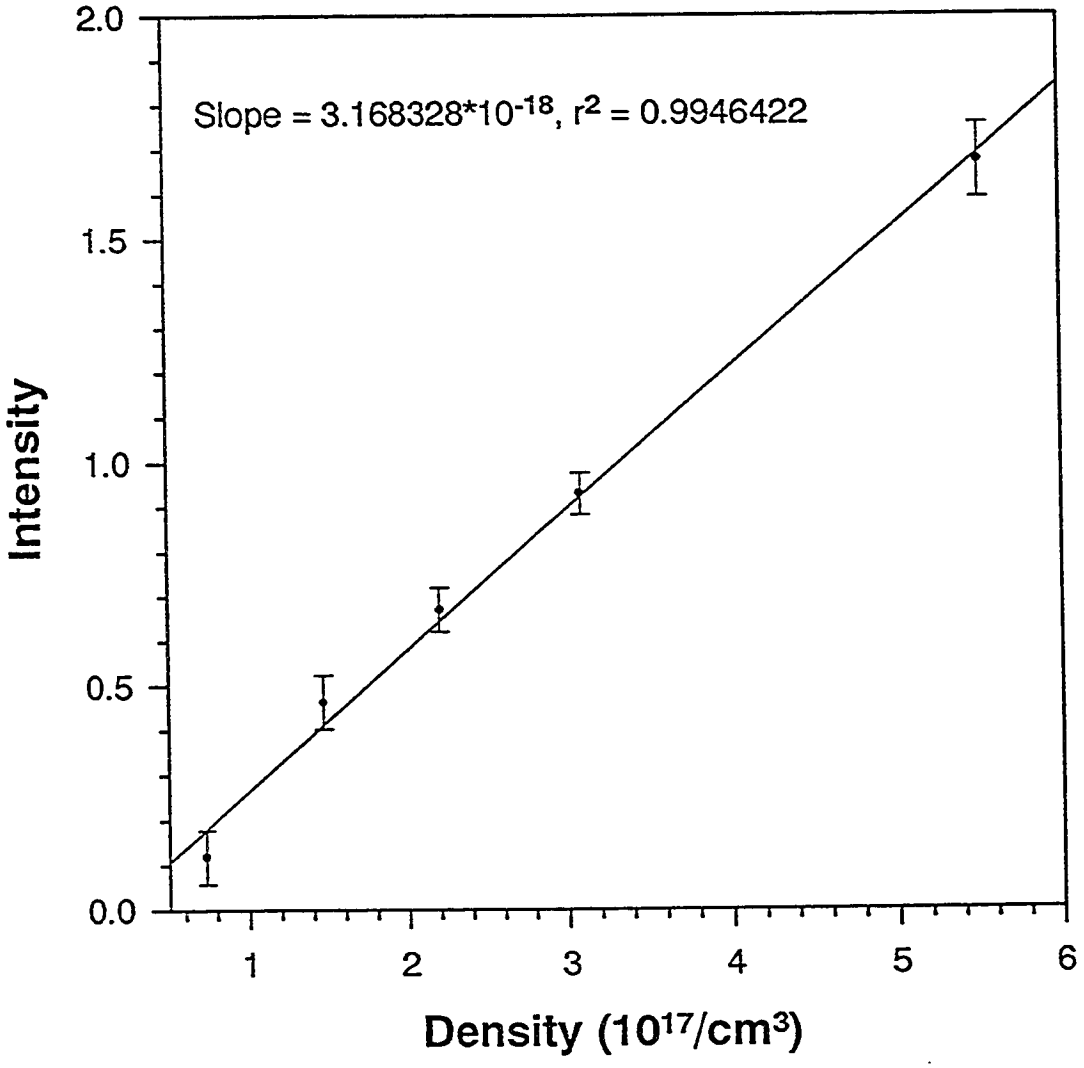

Figure 4.18: Fluorescence yield from the 4s5p $^1P_1 \rightarrow$ 4s3d$^1D_2$ at 6717 Å at different Argon densities, when the 3d4p $^3F_4$ state of calcium was prepared with the help of the step-wise laser excitation process.

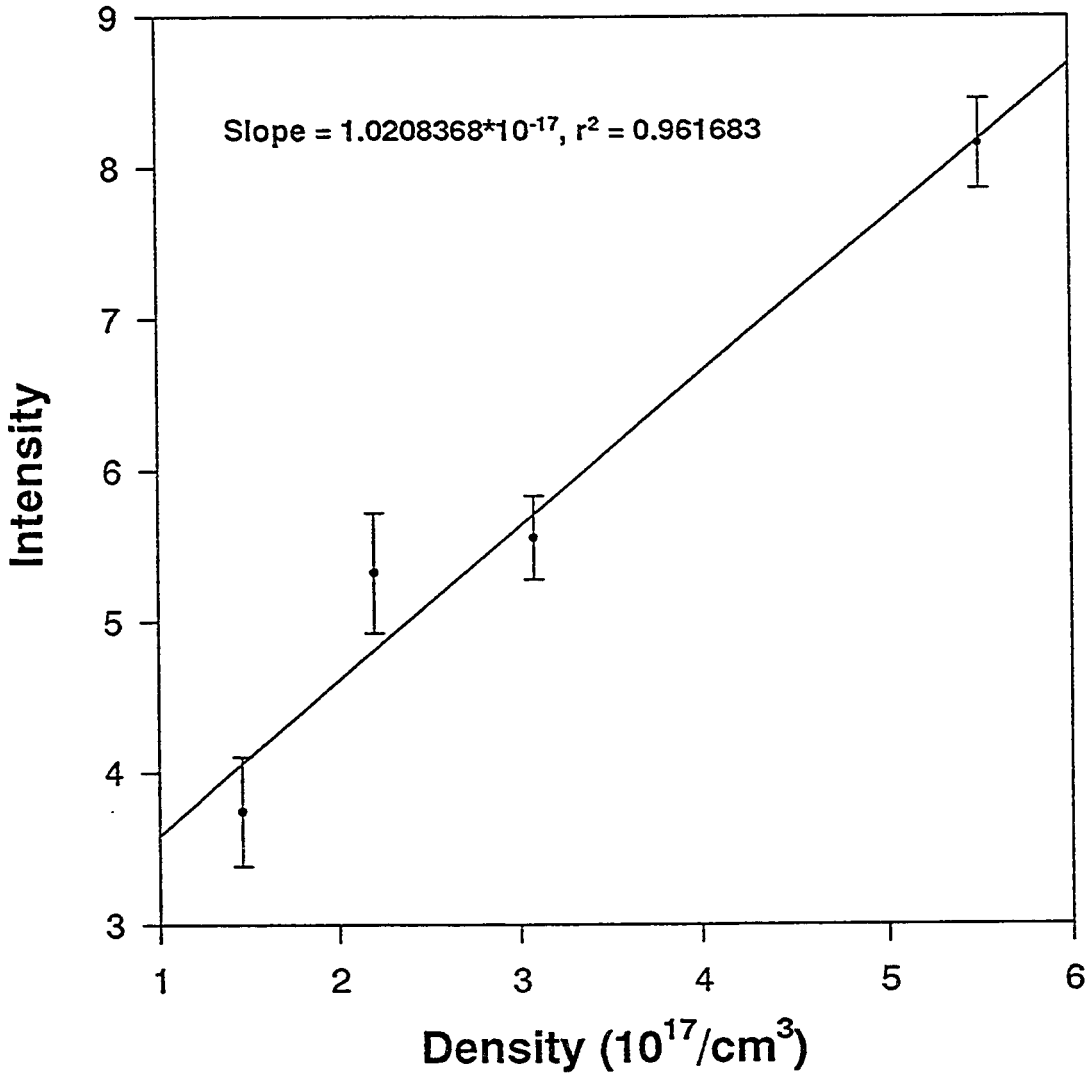

Figure 4.19: Fluorescence yield from the 3d4p $^1D_2 \rightarrow$ 4s3d $^1D_2$ at 7148 Å at different Argon densities, when the 3d4p $^3F_4$ state of calcium was prepared with the help of the step-wise laser excitation process.

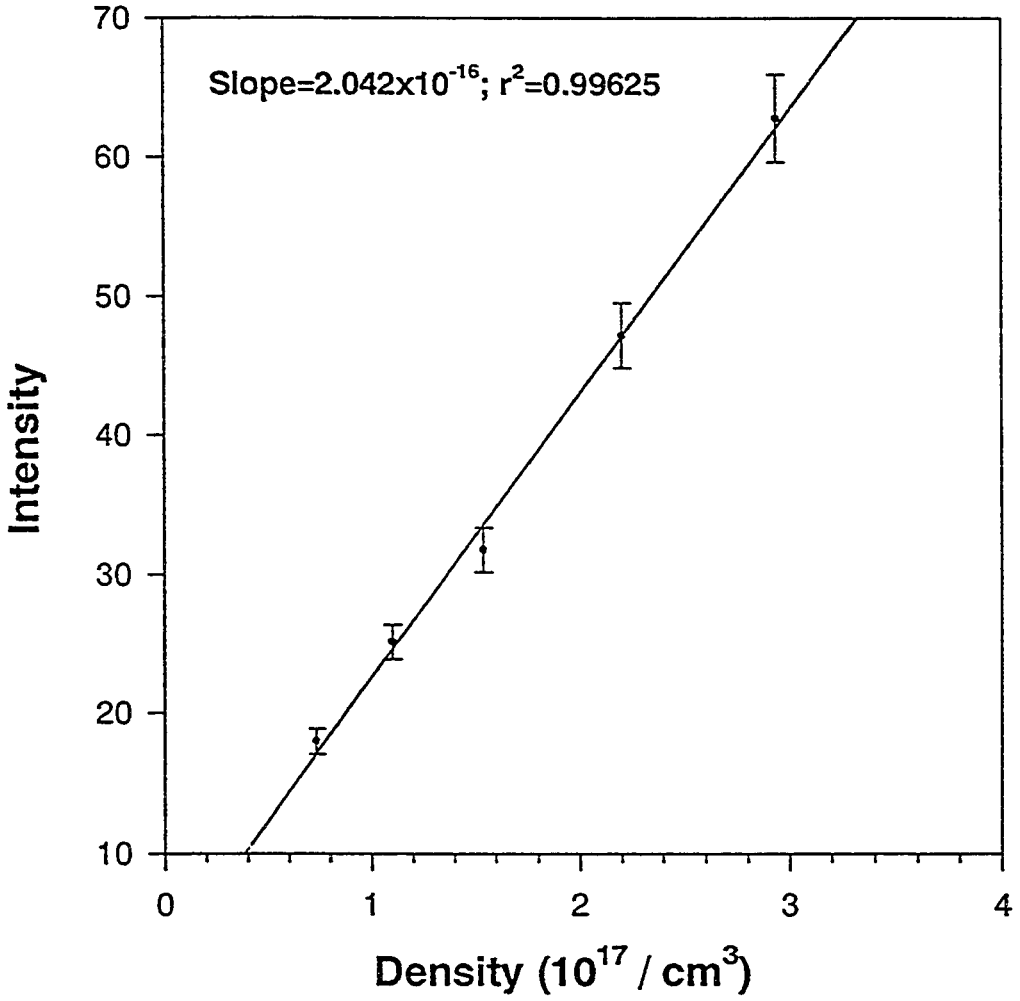

Figure 4.20: Fluorescence yield from the 3d4p $^1D_2 \rightarrow$ 4s3d $^1D_2$ at 7148 Å at different Argon densities, when the 3d4p $^3F_2$ state of calcium was prepared with the help of the step-wise laser excitation process.

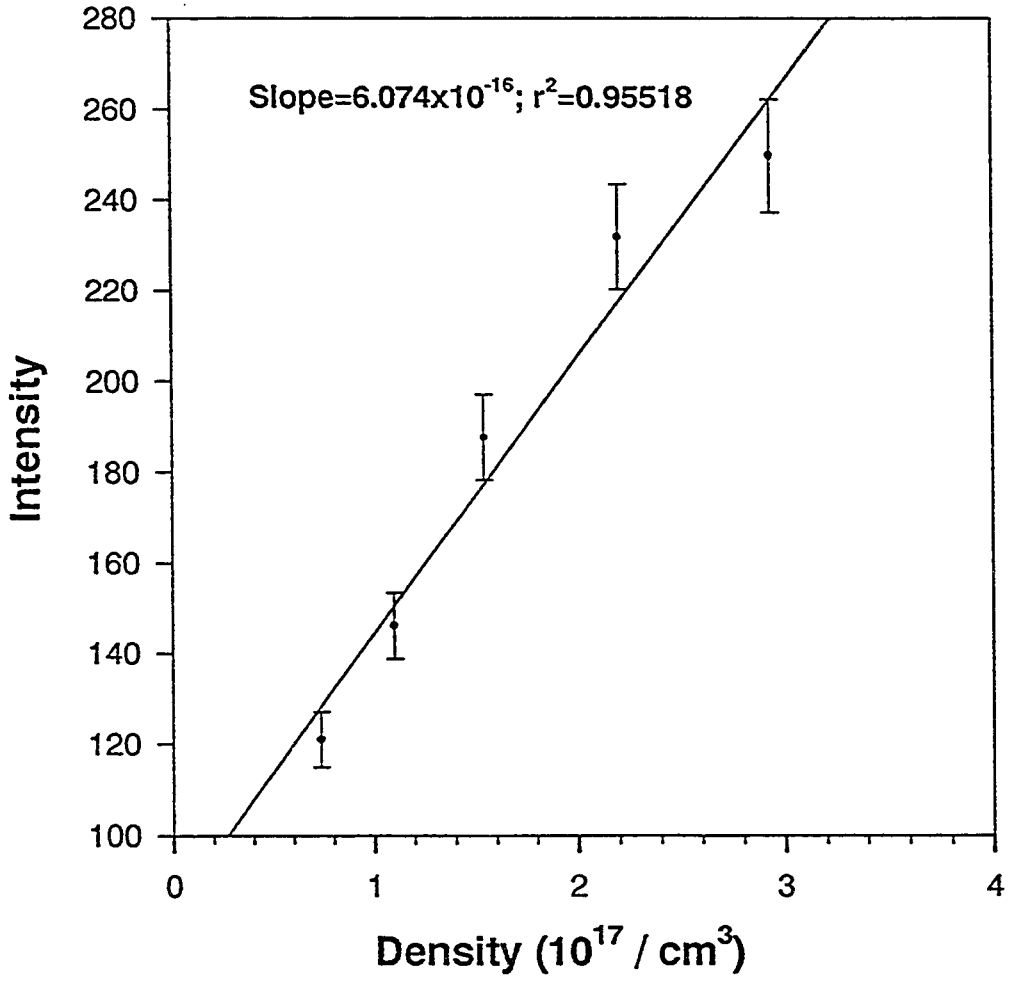

Figure 4.21: Fluorescence yield from the 3d4p $^3F_2 \rightarrow$ 4s3d $^1D_2$ at 7202 Å at different Argon densities, when the 3d4p $^3F_2$ state of calcium was prepared with the help of the step-wise laser excitation process.

4.5.4 Parent State $4s5p\ ^3P_2$

Fig 4.22 shows 4s5p $^3P_2$ as the parent states together with the relevant product states and the transitions on which fluorescence was observed.

Fig 4.23 shows the intensity behavior of the 3d4p $^1D_2 \rightarrow$ 4s3d $^1D_2$ transition at 7148 Å as a function of Ar density. The slope is 1.23×10^{-17}. The intensity behavior of the 3d4p $^3F_2 \rightarrow$ 4s3d $^1D_2$ transition at 7202 Å as a function of Ar density is shown in Fig 4.24. The corresponding slope is 9.26×10^{-18}. Similarly Fig 4.25 illustrates the intensity behavior of the 4s5p $^1P_1 \rightarrow$ 4s3d$^1D_2$ transition at 6717 Å as a function of Ar density. The slope is 4.38×10^{-18}. Likewise, the intensity behavior as a function of Ar density of the 4s4d $^3D_3 \rightarrow$ 4s4p $^3P_2$ transition at 4454 Å is shown in Fig 4.26. The slope is 7.02×10^{-18}. The intensity behavior of the 3d4p $^1D_2 \rightarrow$ 4s3d $^3D_1$ transition at 6449 Å as a function of Ar density is shown in Fig 4.27. Here, the slope is 8.19×10^{-17}.

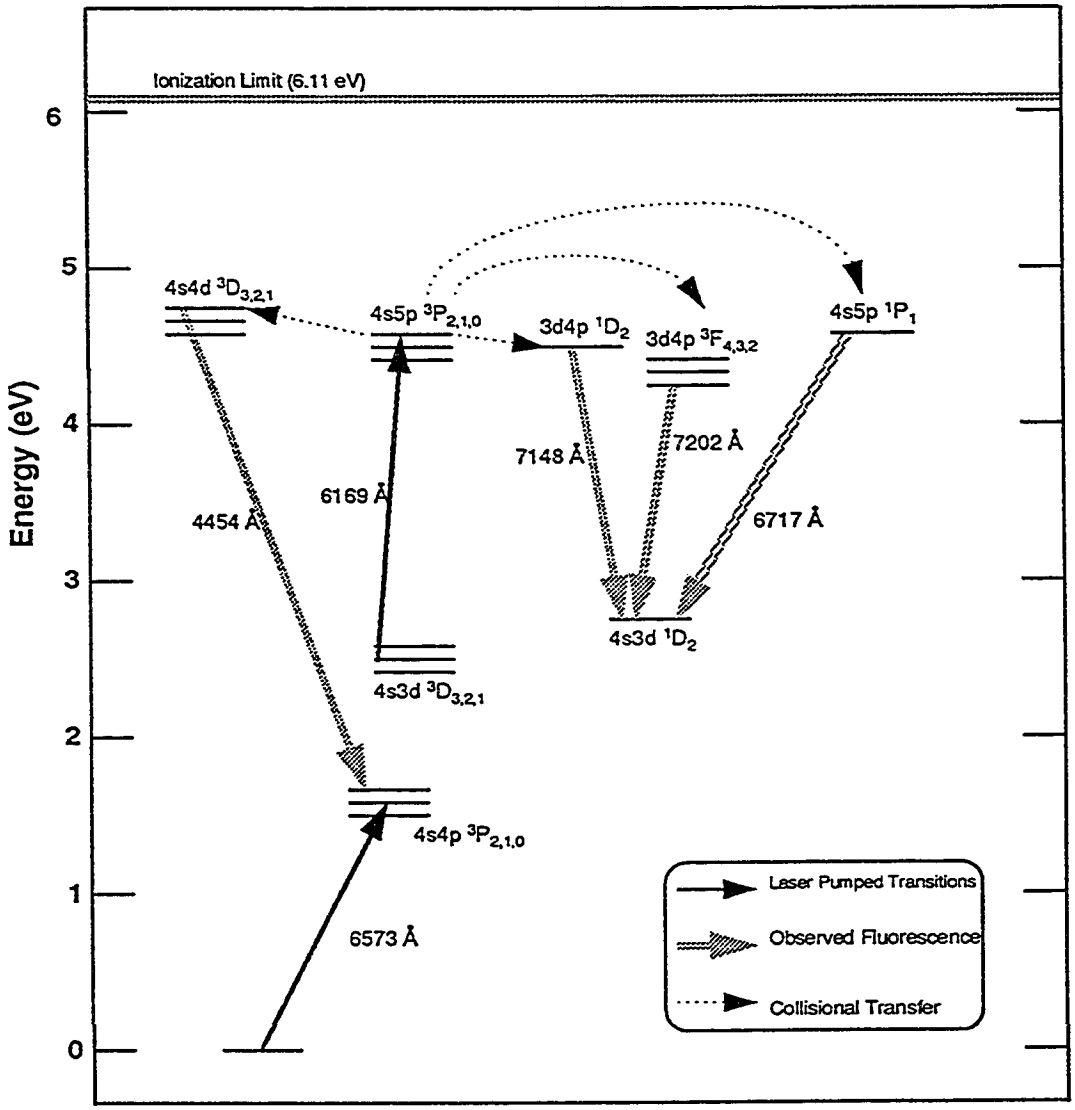

Figure 4.22: Partial energy level diagram for the calcium atom showing the laser - excited 4s5p $^3P_2$ state, the predominant product states (3d4p $^1D_2$, 3d4p $^3F_2$, 4s5p $^1P_1$) populated by collisions with Argon, and fluorescent transitions observed.

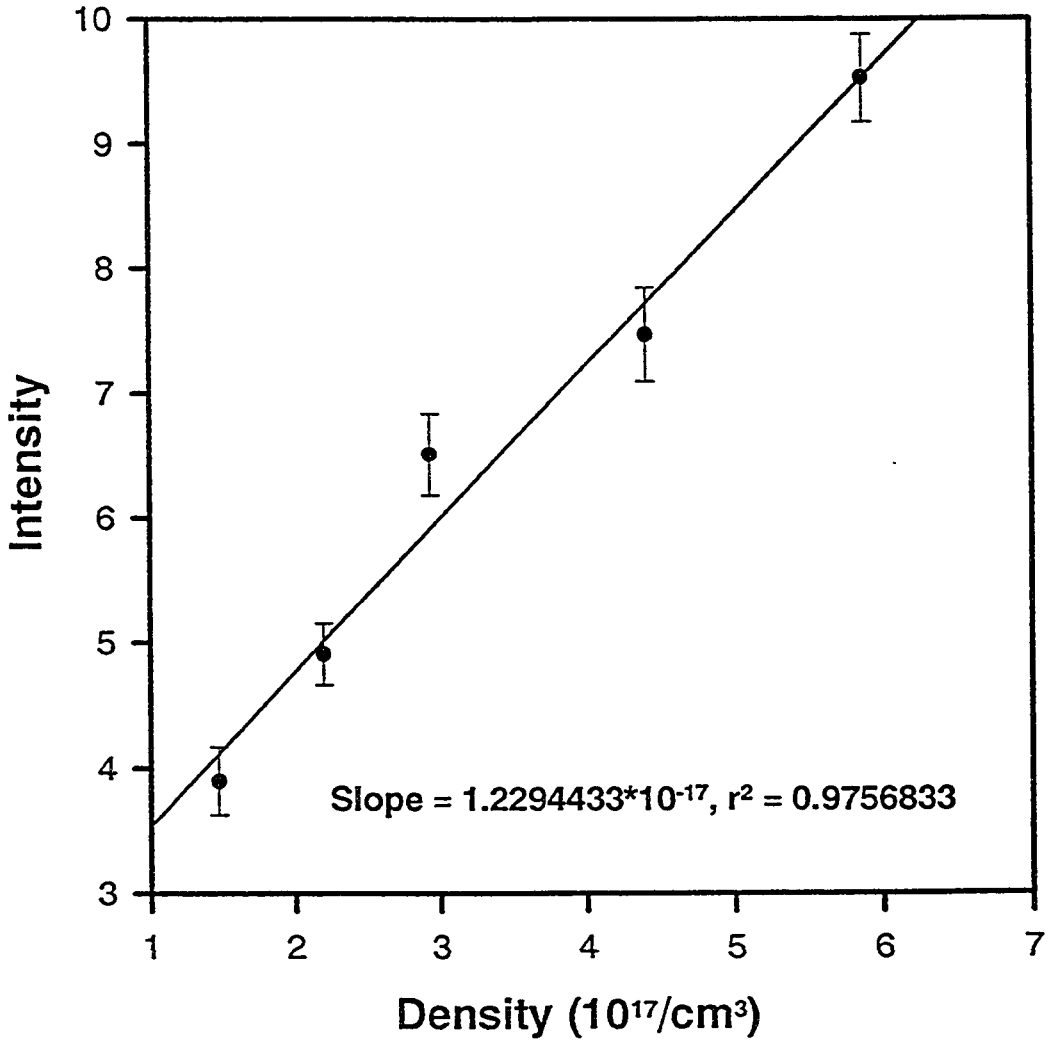

Figure 4.23: Fluorescence yield from the 3d4p $^1D_2 \rightarrow$ 4s3d $^1D_2$ at 7148 Å at different Argon densities, when the 4s5p $^3P_2$ state of calcium was prepared with the help of the step-wise laser excitation process.

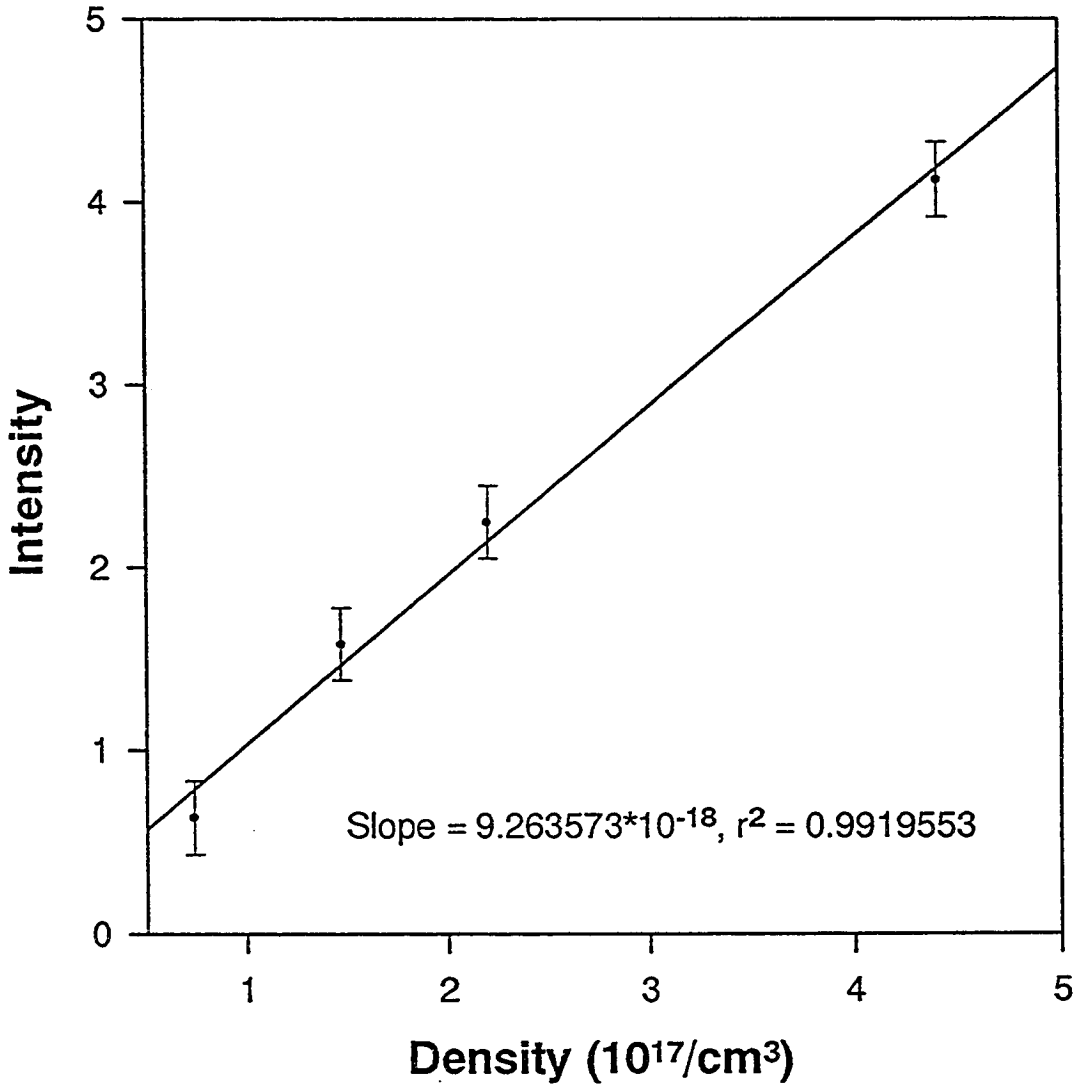

Figure 4.24: Fluorescence yield from the 3d4p $^3F_2 \rightarrow$ 4s3d $^1D_2$ at 7202 Å at different Argon densities, when the 4s5p $^3P_2$ state of calcium was prepared with the help of the step-wise laser excitation process.

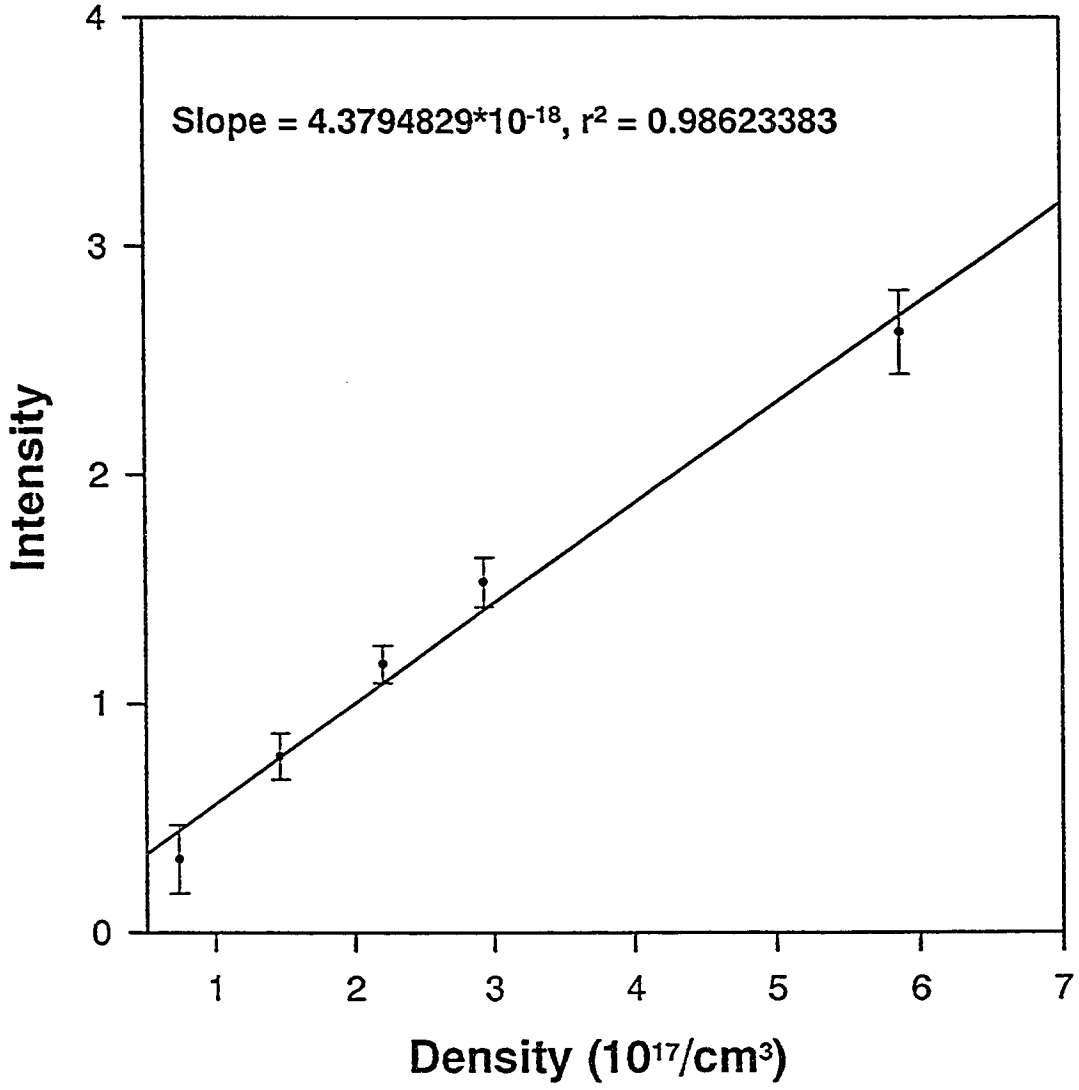

Figure 4.25: Fluorescence yield from the 4s5p $^1P_1 \rightarrow$ 4s3d$^1D_2$ at 6717 Å at different Argon densities, when the 4s5p $^3P_2$ state of calcium was prepared with the help of the step-wise laser excitation process.

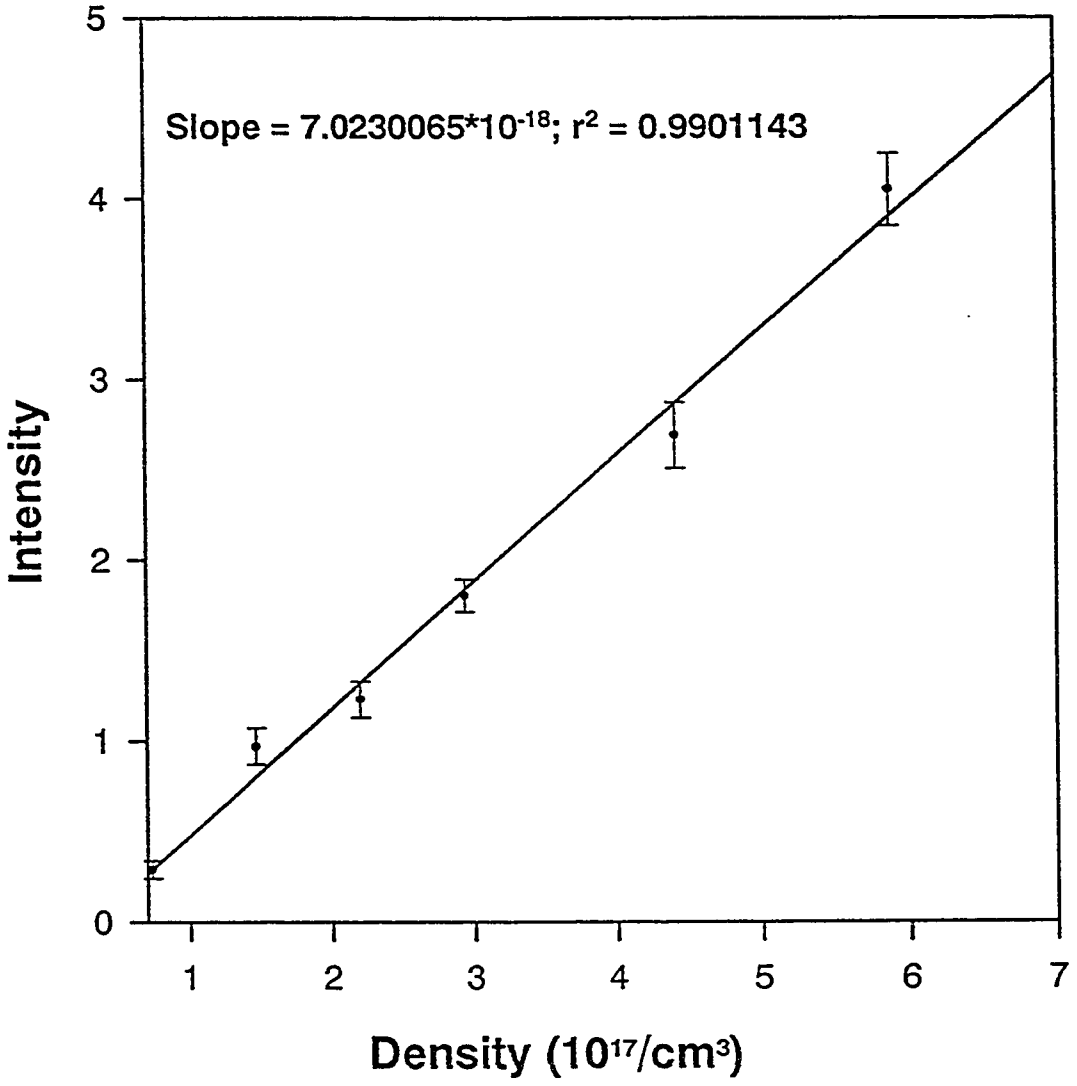

Figure 4.26: Fluorescence yield from the 4s4d $^3D_3 \rightarrow$ 4s4p $^3P_2$ at 4454 Å at different Argon densities, when the 4s5p $^3P_2$ state of calcium was prepared with the help of the step-wise laser excitation process.

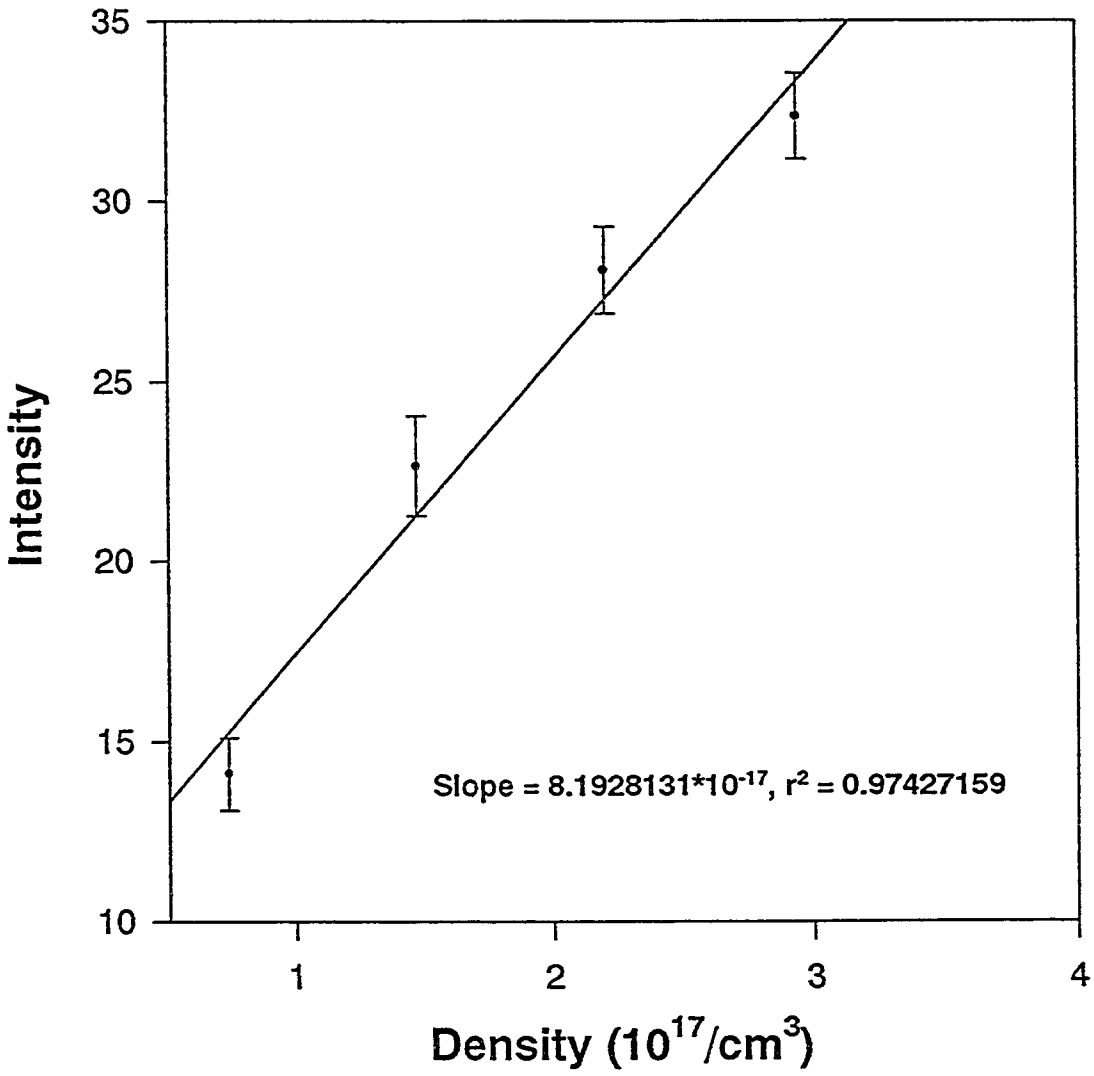

Figure 4.27: Fluorescence yield from the 3d4p $^1D_2 \rightarrow$ 4s3d $^3D_1$ at 6449 Å at different Argon densities, when the 4s5p $^3P_2$ state of calcium was prepared with the help of the step-wise laser excitation process.

4.5.5 Parent State $3d4p\ ^3D_1$

Fig 4.28 shows the 3d4p $^3D_1$ state as the parent state. The respective product states and the transitions on which fluorescence was observed are also shown here. Figures 4.29 to 4.31 show the pressure versus the intensity plots for selected transitions, when the 3d4p $^3D_1$ parent state was prepared by the second laser.

The intensity behavior of the 3d4p $^3P_2 \rightarrow$ 4s3d $^3D_3$ transition at 5270 Å as a function of Ar density is shown in Fig 4.29. The corresponding slope is 8.93×10^{-18}. Likewise, the intensity behavior of the 4s4d $^3D_3 \rightarrow$ 4s4p $^3P_2$ transition at 4454 Å as a function of Ar density is shown in Fig 4.30. The corresponding slope is 2.08×10^{-17}. Finally, Fig 4.31 shows the intensity behavior of the $4p^2\ ^3P_2 \rightarrow$ 4s4p $^3P_2$ transition at 4302 Å as a function of Ar density. The corresponding slope is 1.18×10^{-17}.

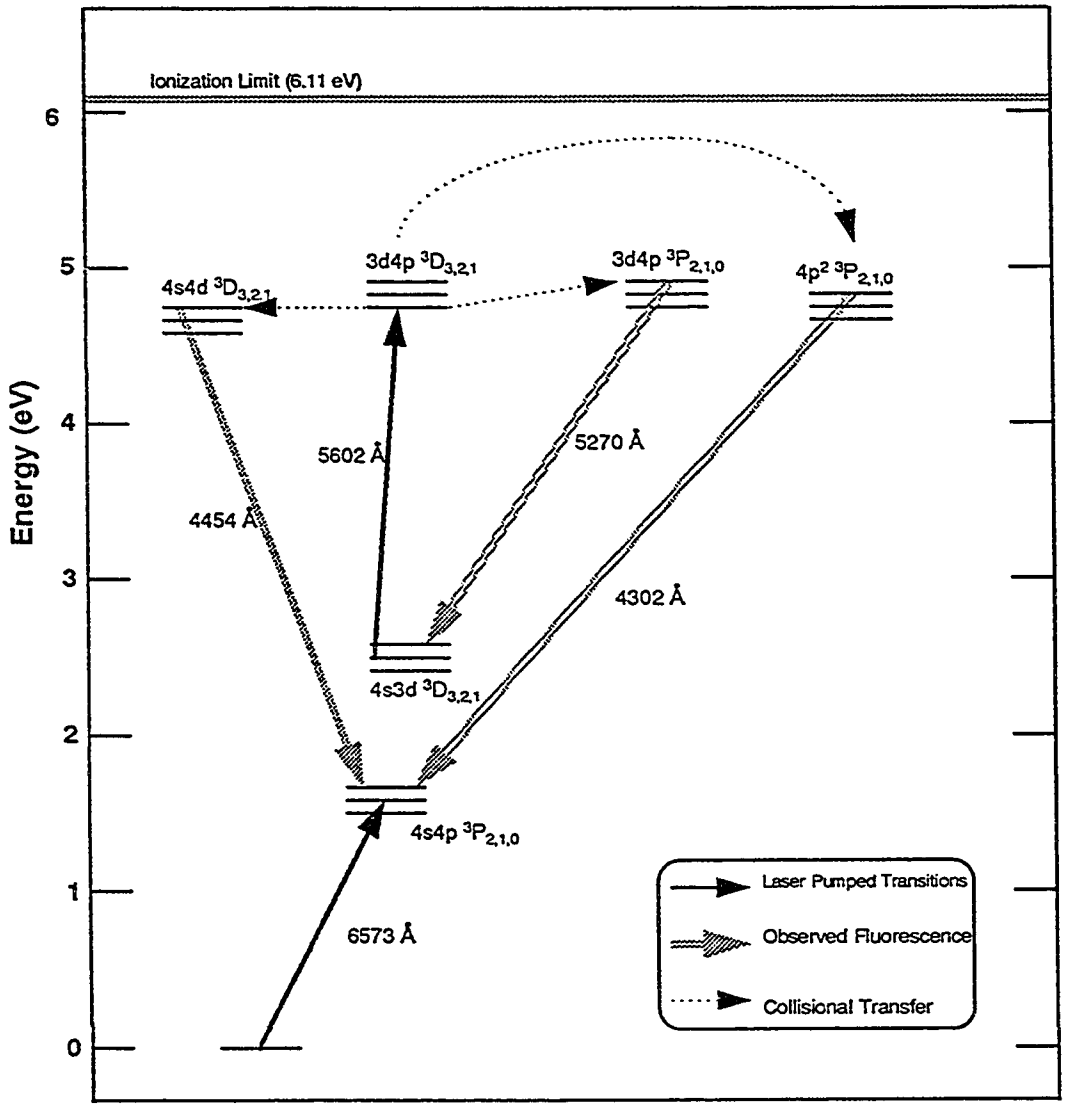

Figure 4.28: Partial nergy level diagram for the calcium atom showing the laser - excited 3d4p $^3D_1$ state, the predominant product states (4s4d $^3D_3$, 3d4p $^3P_2$, 4p^2 $^3P_2$) populated by collisions with Argon, and fluorescent transitions observed.

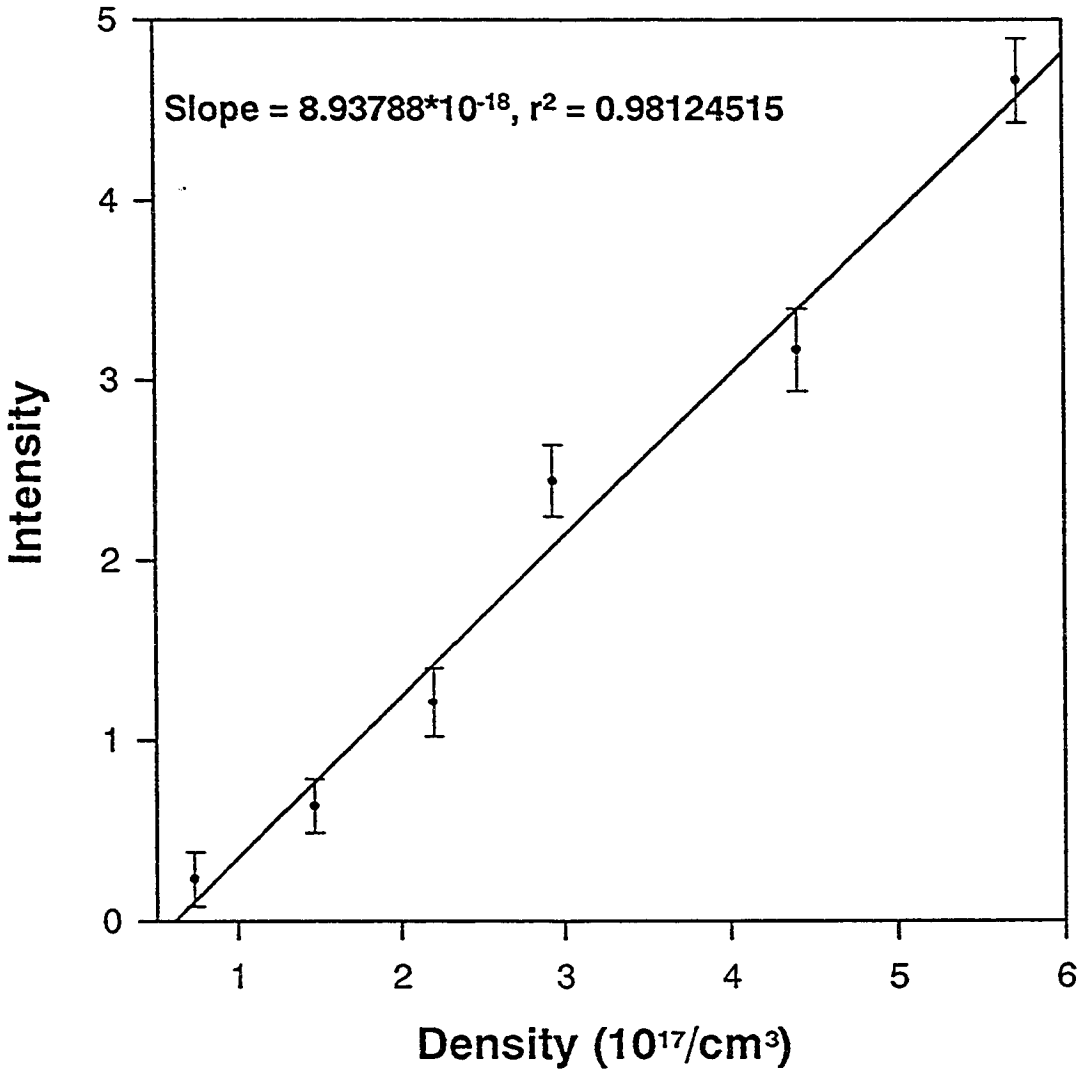

Figure 4.29: Fluorescence yield from the 3d4p $^3P_2 \rightarrow$ 4s3d $^3D_3$ at 5270 Å at different Argon densities, when the 3d4p $^3D_1$ state of calcium was prepared with the help of the step-wise laser excitation process.

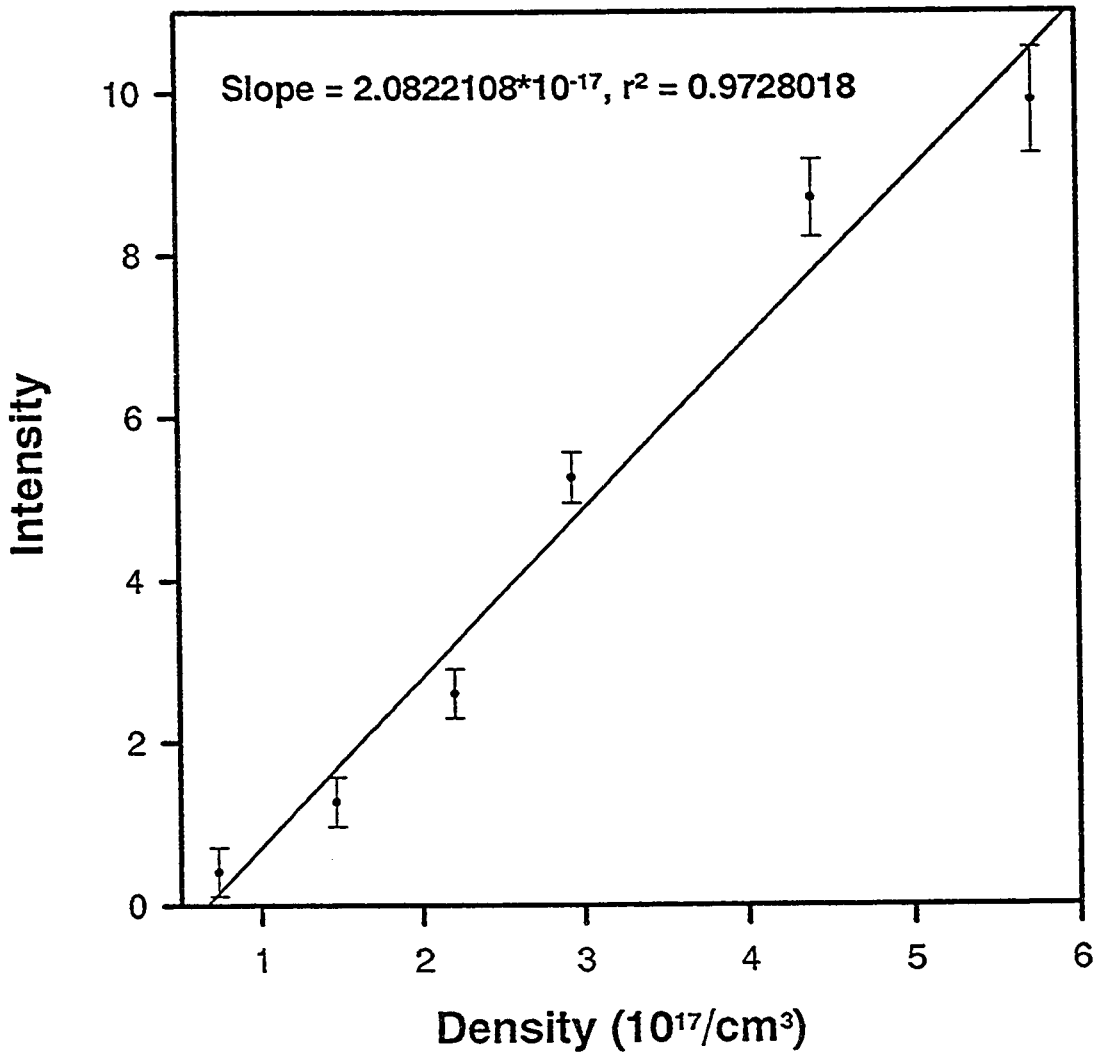

Figure 4.30: Fluorescence yield from the 4s4d $^3D_3 \rightarrow$ 4s4p $^3P_2$ at 4454 Å at different Argon densities, when the 3d4p $^3D_1$ state of calcium was prepared with the help of the step-wise laser excitation process.

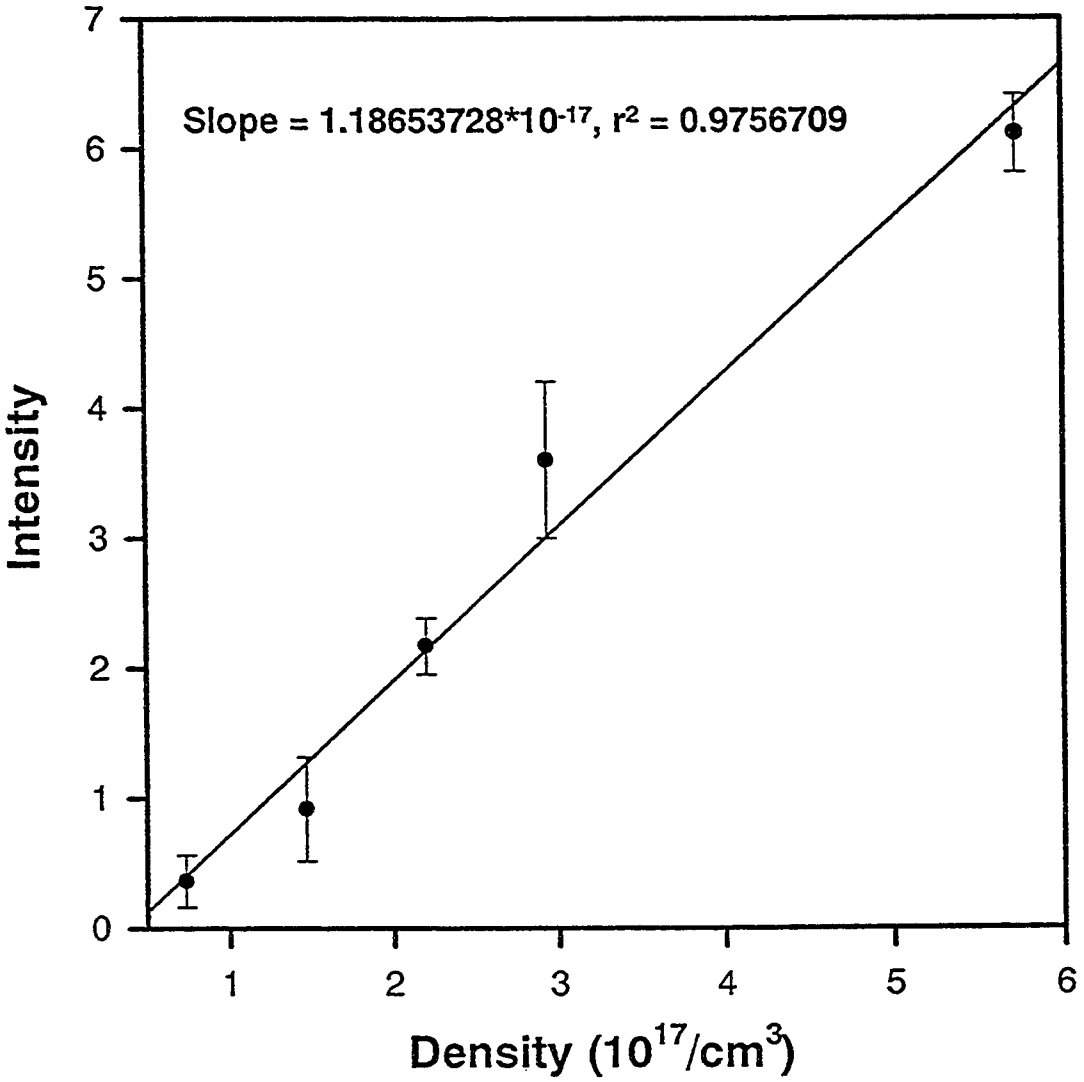

Figure 4.31: Fluorescence yield from the $4p^2\ ^3P_2 \rightarrow 4s4p\ ^3P_2$ at 4302 Å at different Argon densities, when the $3d4p\ ^3D_1$ state of calcium was prepared with the help of the step-wise laser excitation process.

4.6 State-to-state rate constant

In order to obtain the state-to-state rate constants we used the method discussed in chapter 2 (section 2.4). Table 4.5 lists all the observed transitions, the known total radiative rates Γ of the upper state of the transition, the Einstein's A coefficients for the transitions taken from the literature [90, 91, 92], and the response function F taken from the response curves supplied by the manufacturer.

Transition	λ (Å)	$\Gamma^{\dagger}$ (10^8 s^{-1})	$A^{\dagger}$ (10^8 s^{-1})	$F(\lambda)^{\ddagger}$
$3d4p\ ^1D_2 \rightarrow 4s3d\ ^3D_1$	6449	0.104	0.09	0.36
$3d4p\ ^1D_2 \rightarrow 4s3d\ ^1D_2$	7148	0.4754*	0.358*	0.16
$3d4p\ ^3F_4 \rightarrow 4s3d\ ^3D_3$	6439	—	0.53	0.362
$4s5p\ ^3P_2 \rightarrow 4s3d\ ^3D_3$	6169	0.2253	0.19	0.46
$3d4p\ ^3D_1 \rightarrow 4s3d\ ^3D_2$	5602	0.57	0.14	0.6
$3d4p\ ^3F_2 \rightarrow 4s3d\ ^1D_2$	7202	0.435*	0.141*	0.145
$4s5p\ ^1P_1 \rightarrow 4s3d\ ^1D_2$	6717	0.1227	0.12	0.245
$4s4d\ ^3D_3 \rightarrow 4s4p\ ^3P_2$	4454	—	0.86	0.956
$4s4d\ ^1D_2 \rightarrow 4s4p\ ^1P_1$	7326	—	6.7**	0.113
$3d4p\ ^3P_2 \rightarrow 4s3d\ ^3D_3$	5270	0.5971	0.5	0.75
$4p^2\ ^3P_2 \rightarrow 4s4p\ ^3P_2$	4302	1.794	1.36	0.994

Table 4.5: Atomic data for the observed transitions for rate constant measurements.

† All values from Ref. [90], unless otherwise noted.
‡ Dimensionless, relative calibration factor for optics and monochromator efficiency and photomultiplier response.
⋆ Reference [91].
⋆⋆ Reference [92].

The rate constants are calculated with the help of equation 2.30 discussed previously in chapter 2. At densities needed to obtain reasonable signal to noise ratios in the product state spectra, the derived rate constants are observed to decrease with increasing Argon density. Thus we measure the K_{1j} as a function of rare gas pressure, and back-extrapolate to zero pressure (y - intercept) to obtain the best estimate of the true rate constants. The results obtained by this method agree well with the results obtained for other transitions in Ca and some other atoms reported in publications on similar subject [22]. Examples of the data obtained are shown in Figure 4.32 to 4.35. The state-specific rate constants are summarized in Tables 4.6 to 4.8. Most of the rate constants were determined from multiple runs of a single spectral line. In general, the results are mutually consistent. One general limitation is the lack of accurate values of the A coefficients, which differ substantially from one source to another [90, 91, 92]. For example the value of A quoted by [91] is $0.116 \times 10^8/\text{sec}$ while [90] gives $A = 0.19 \times 10^8/\text{sec}$ (for the $4s5p\ ^3P_2 \rightarrow 4s3d\ ^3D_3$ transition at 6169.56Å). These variations can introduce upto 40% uncertainty in the measured values.

Product State	ΔE (cm^{-1})	K_{1j} (10^{-11} cm^3/sec)
$3d4p\ ^1D_2$	61.476	4.29

Table 4.6: The forward rate constant for the parent state 3d4p $^3F_2$ induced by Ar collisions.

Product State	ΔE (cm^{-1})	K_{1j} (10^{-11} cm^3/sec)
$3d4p\ ^3F_2$	104.959	14.8141
$4s5p\ ^1P_1$	896.202	0.745338
$4s5p\ ^3P_2$	739.71	2.373

Table 4.7: The forward rate constant for the parent state 3d4p $^1D_2$ induced by Ar collisions.

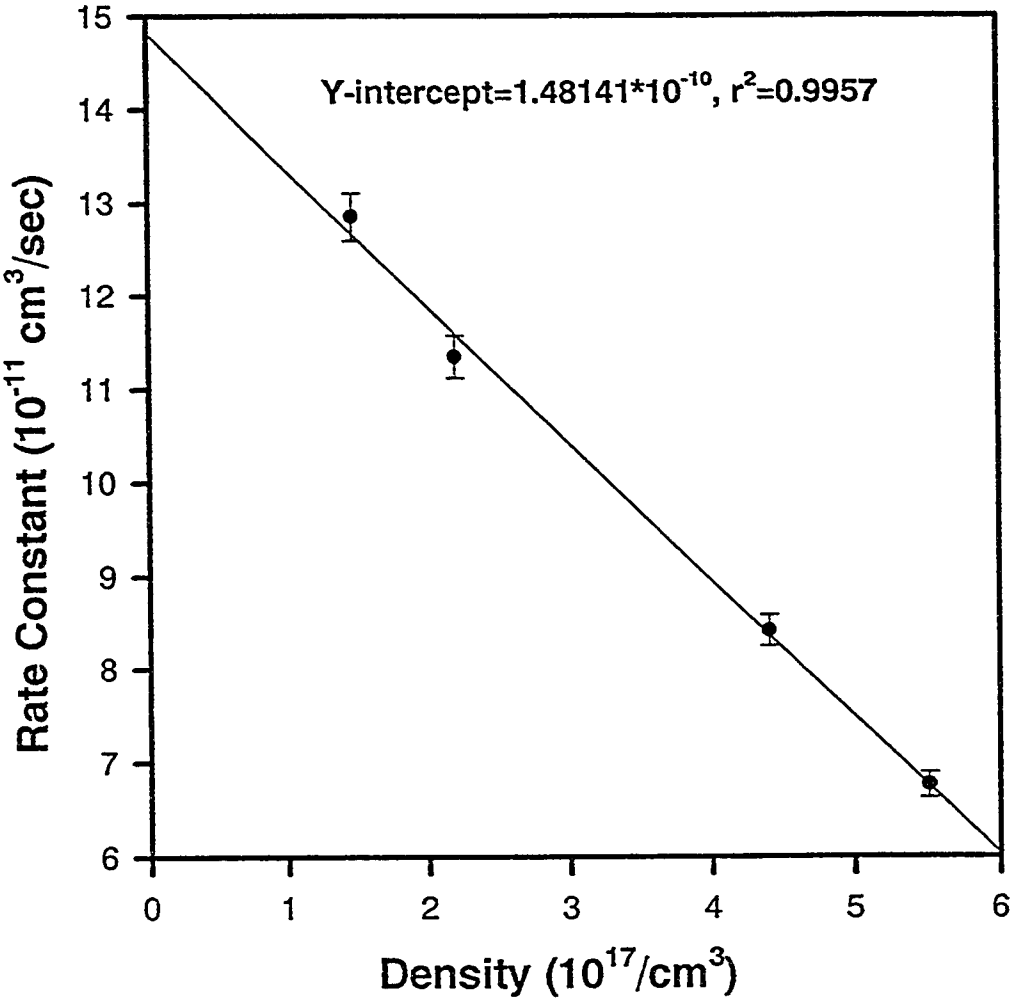

Figure 4.32: A plot of the state-to-state rate constant for energy transfer from 3d4p $^1D_2 \rightarrow 3d4p^3F_2$ as a function of the Argon pressure. The line is a weighted least-squares fits to the data, the intercept is taken to be the state-to-state rate constant.

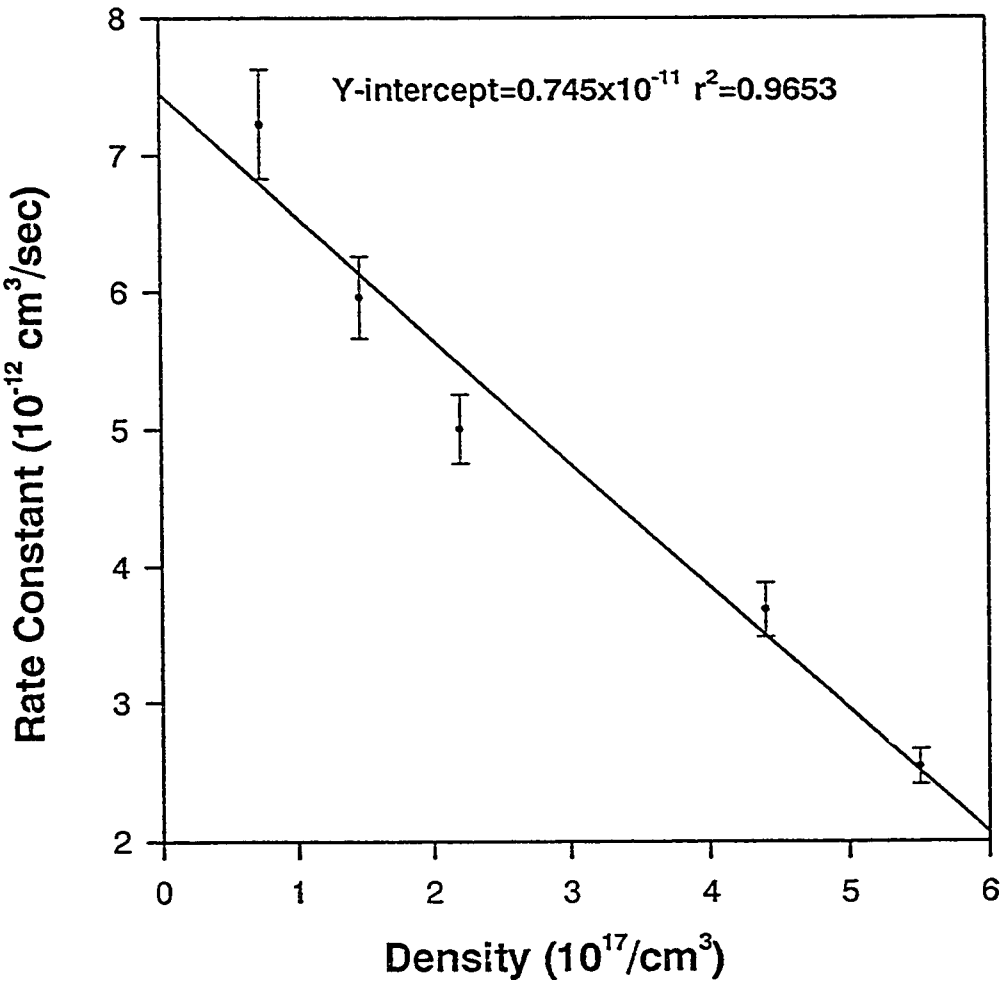

Figure 4.33: A plot of the state-to-state rate constant for energy transfer from 3d4p $^1D_2 \rightarrow$ 4s5p $^1P_1$ as a function of the Argon pressure. The line is a weighted least-squares fits to the data, the intercept is taken to be the state-to-state rate constant.

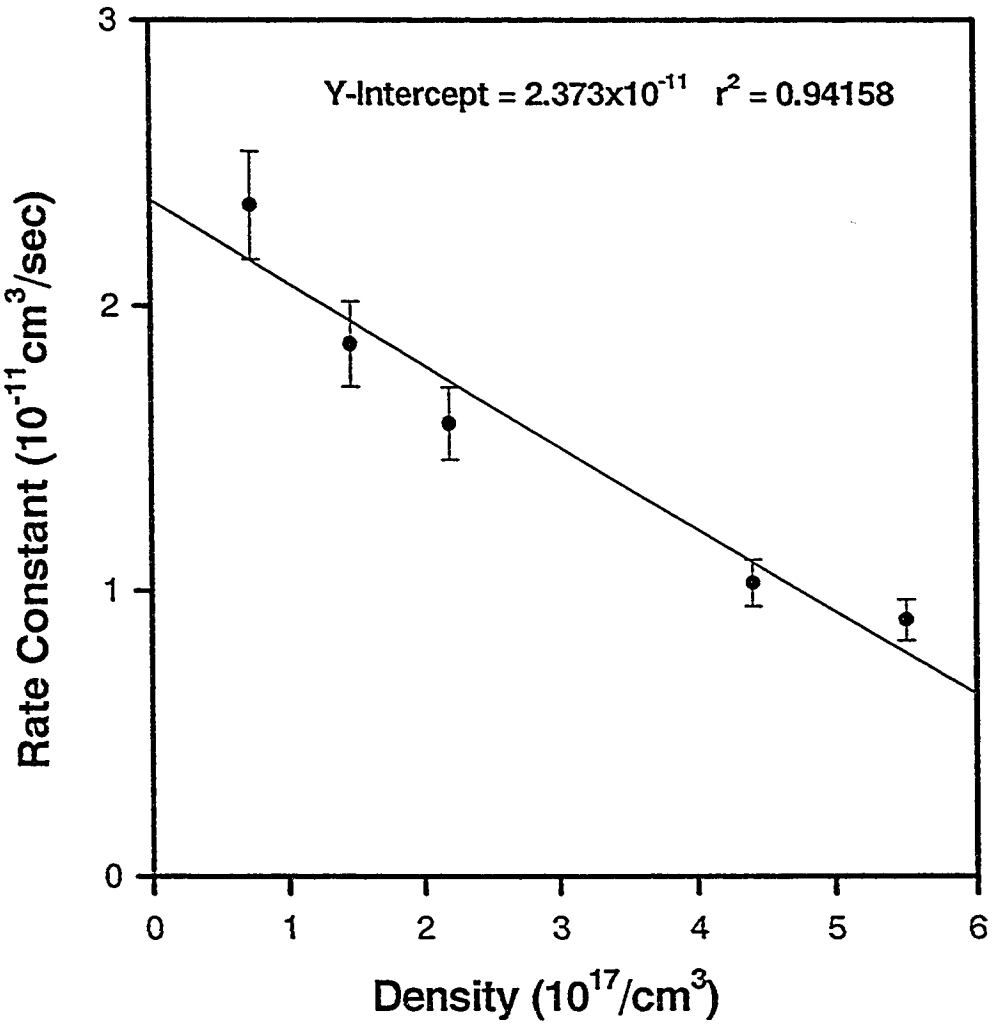

Figure 4.34: A plot of the state-to-state rate constant for energy transfer from 3d4p $^1D_2 \rightarrow$ 4s5p $^3P_2$ as a function of the Argon pressure. The line is a weighted least-squares fits to the data, the intercept is taken to be the state-to-state rate constant.

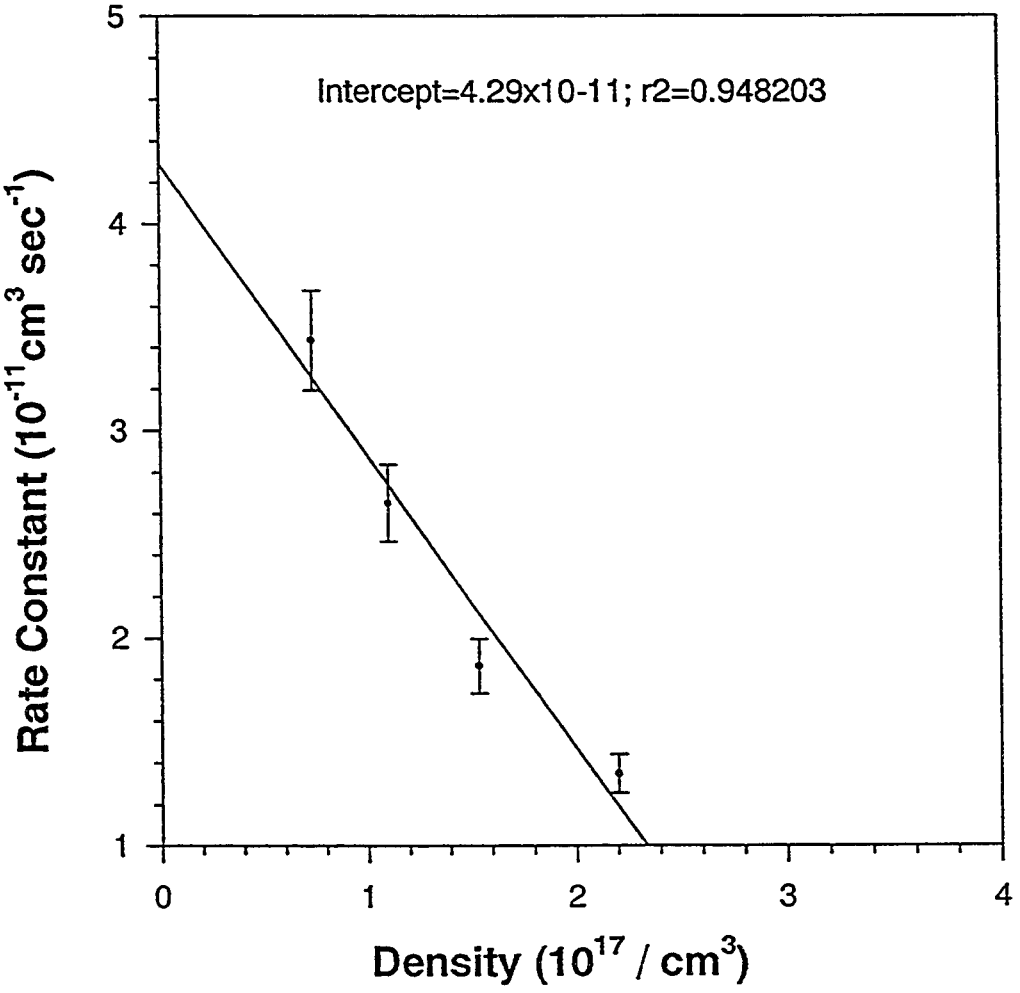

Figure 4.35: A plot of the state-to-state rate constant for energy transfer from 3d4p $^3F_2 \rightarrow$ 3d4p $^1D_2$ as a function of the Argon pressure. The line is a weighted least-squares fits to the data, the intercept is taken to be the state-to-state rate constant.

Smedley et al [20] also reported that for helium densities similar to those used in this experiment, a linear dependence of the rate constants on rare gas density is observed. The strongest density dependence is found for states which have relatively long radiative lifetimes or relatively large rate constants for population transfer out of that particular state.

In another previous publication, Hale and Leone [22] carried out similar work on the total deactivation rate constants for Ca. They measured the state-to-state population transfer rate from 4s5p $^1P_1$ to 4s5p $^3P_2$ state of calcium under the influence of Ar as a buffer gas and found it to be 5.2×10^{-11} cm^3 sec^{-1}. We used their results to calculate the state-to-state population transfer rate from 4s5p $^3P_2$ parent state to 4s5p $^1P_1$ product state assuming detailed balance.

$$K_{ji} = K_{ij}\frac{g_i}{g_j}\exp\{-(E_i - E_j)/KT\} \tag{4.1}$$

Subsequently on using Equation 2.30, the available data on the Einstein's A coefficients and the experimentally acquired values of the observed intensities, we were able to calculate the state-to-state population transfer rate from $4s5p\ ^3P_2$ to the other nearby product states (3d4p $^1D_2$, 3d4p $^3F_2$) as well. These results are displayed in Table 4.8.

It is apparent from Tables 4.6 to 4.8 that the transfer to $3d4p\ ^3F$ states is generally the highest. In particular the $3d4p\ ^1D_2$ to $3d4p\ ^3F_2$ transfer rate is nearly double the transfer rate from $3d4p\ ^1D_2$ to $4s5p\ ^3P_1$ while it is nearly 20 times the transfer rate from $3d4p\ ^1D_2$ to $4s5p\ ^1P_1$ (see Table 4.7). Similarly the transfer rate from $4s5p$

Product State	ΔE (cm^{-1})	K_{1j} (10^{-11} cm^3/sec)
$3d4p\ ^1D_2$	719.336	13.95
$3d4p\ ^3F_2$	824.295	26.95
$4s5p\ ^1P_1$	176.866	2.5*

Table 4.8: The forward rate constant for the parent state 4s5p $^3P_2$ induced by Ar collisions. * Rate constant calculated via detailed balance using results of Hale and Leone (see text).

$^3P_2$ to $3d4p\ ^3F_2$ is nearly twice the transfer rate to $3d4p\ ^1D_2$ (Table 4.8). Some of these results were confirmed in the recent experiments of Khan et al [77] where Ar-supported collisional transfer to $3d4p\ ^3F$ states was exploited to access some high angular momentum $^3G_{3,4,5}$ states using a multistep excitations scheme.

Chapter 5

Computer Model Calculations & Comparison with Experimental Results

5.1 Introduction

A computational study for the calculations of instantaneous population densities of the laser prepared state and the nearby states based on rate - equation analysis is presented. The primary interest, however, is to simulate the population transfers and cross check the experimentally calculated rate constants with the help of the simple kinetic model discussed in chapter 2. This is achieved by converting the computed instantaneous population densities into line intensities i.e. the fluorescence yield from the upper states under consideration. The ratio of intensities of fluorescence from any two states is then taken and compared with the experimental data. Various collisional and radiative processes such as, electron impact excitation and ionization, radiative and three body recombination, spontaneous radiative decay, energy pooling collisions, and collisions with the buffer gas have been included for calculating the instantaneous population densities, as we believe that these processes could play a vital role for the

transfer of population from one state to another. The convective diffusion of laser-excited atoms is also included. The appropriate rate equations for the population density in different atomic states, electron density and electron energy are developed. These are solved numerically using a fourth order Runge-Kutta method.

The main problem in developing a realistic computer model is the lack of reliable experimental data on the rate coefficients for various collisional and radiative processes. Information on the level energies and radiative transition probabilities for most of the states considered here is available [89, 90, 92]. However, data for collisional processes including the electron-atom and atom-atom collisions is not available. We have used approximate rates for hydrogen - like atoms including alkalis. However, we have incorporated the appropriate weight factors to take into account any deviations from this hydrogenic behavior.

5.2 The Computer Code

Khan et al [25] have recently developed a computer code based on the fourth order Runge-Kutta method to study the dynamics of the populations of various atomic states in a laser-pumped vapor. This code is based on the principles that the laser saturates the pumped transitions and superelastic transfer of energy of laser-excited atoms to free electrons is instrumental in effecting large scale excitation and ionization. Their main interest, however, was in the study of population inversions between various states in the "thermalizing" phase of laser-pumped Ca vapor following laser excitation.

We have modified the code of Khan et al [25] to simulate a step-wise laser ex-

citation of highly excited states as opposed to single step, single laser excitation. Furthermore, collisions with Ar are also included which were not considered before. We have used this model to study the problem of energy transfer between nearby states. The solutions of the coupled rate equations give the temporal behavior of level populations, the energy of free electrons and temperature as a function of time. The rate coefficients in these equations can be varied to account for the observed phenomena. The main features of this model are:

1. The laser pulse from laser 1 (Excimer Laser pumped dye laser) is assumed to saturate the primary transition $4s^2\ ^1S_0 \rightarrow 4s4p\ ^3P_1$ such that the populations N_2 and N_1 of the upper and the lower states are in the ratio of their statistical weights, i.e.

$$\frac{N_2}{N_1} = \frac{g_2}{g_1} \tag{5.1}$$

   Here, enhanced absorption in the presence of collisions with Ar (buffer gas) atoms is included[93]. However, in the case of pumping a metastable state, as in the present case, this may not be important as long as the laser saturates the transition within the duration of its pulse. In fact, instantaneous deposition of energy would also be adequate in this case.

2. Once a large pool of excited atoms in the metastable state is created, the energy stored in the excited atoms is subsequently redistributed through various collisional and radiative processes. In particular, it has been experimentally observed [6, 8] that a rapid transfer of atomic populations to the 4s3d ^{3}D states

located approximately 5150 cm^{-1} above the 4s4p $^3P_1$ states takes place. This is usually affected in 1 - 2 μs after the population of 4s4p $^3P_1$ state. This was incorporated in the model as a collisional transfer.

3. A second independently tunable laser (Laser 2, Nd:YAG laser pumped dye laser) is then used to prepare a range of highly excited states including 3d4p $^1D_2$, 3d4p ^3F, 4s5p ^3P, 3d4p ^3D and 4s5s ^3S taken one at a time. These are referred to as the "parent states". It is noted that only in the case of 4s5s ^3S, the second laser connects the primary 4s4p ^3P state prepared by the first laser to the parent state. In all other cases, the collisional transfer from the primary 4s4p ^3P state to 4s3d ^3D is utilized before bringing in the second laser.

4. Subsequently, thermal collisions with Ar transfer the population to nearby states henceforth called the "product states".

5. A total of twenty excited states are included in this model. However, explicit calculation of instantaneous population of only the first fifteen states have been made for our present study. In particular, the ground state and fourteen excited states were considered. This is justified by our recent experimental observation that spectral emission from these very states is particularly strong [6] while the spectra of higher states is virtually wiped out [94]. In addition, each triplet is considered as one state assuming that the distribution of population within the triplet is statistical. Table 5.1 gives the details of various states considered, their assigned labels, their energies [90] and their statistical weights.

State #	State	Statistical Weight	E (cm^{-1})	E (eV)
1	$4s^2\ ^1S_0$	1	0	0
2	$4s4p\ ^3P$	9	15210	1.886
3	$4s3d\ ^3D$	15	20356	2.523
4	$4s3d\ ^1D$	5	21850	2.71
5	$4s4p\ ^1P$	3	23652	2.932
6	$4s5s\ ^3S$	3	31539	3.91
7	$3d4p\ ^3F$	21	35831	4.442
8	$3d4p\ ^1D$	5	35835	4.443
9	$4s5p\ ^3P$	9	36565	4.533
10	$4s5p\ ^1P$	3	36732	4.554
11	$4s4d\ ^1D$	5	37298	4.624
12	$4s4d\ ^3D$	15	37754	4.681
13	$3d4p\ ^3D$	15	38232	4.74
14	$4p^2\ ^3P$	9	38508	4.774
15	$3d4p\ ^3P$	9	39338	4.577
16	$4s6s\ ^3S$	3	40474	5.018
17	$4s4f\ ^3F$	21	42171	5.228
18	$4s6p\ ^3P$	9	42519	5.271
19	$4s5d\ ^3D$	15	42745	5.299
20	$4s7s\ ^3S$	3	43981	5.453

Table 5.1: The states alongwith their energies and statistical weights

6. Collisional deexcitation of state 2 promoting rapid superelastic transfer of energy to free electrons which subsequently spearhead further excitation and some possible ionization of laser-pumped atoms, is assumed. Since the energy is initially stored in state 2 which is a metastable state, this process essentially controls the electron temperature, a parameter important in electron collision processes. Thus we have the following processes

$$\text{Ca } 4s4p\ ^3P_1 + e \Rightarrow \text{Ca } 4s^2\ ^1S_0 + e^* \tag{5.2}$$

$$\text{Ca } 4s4p\ ^3P + e^* \Rightarrow \text{Ca } nlml' + e + \Delta E' \tag{5.3}$$

$$\text{Ca } nlml' + e^* \Rightarrow \text{Ca } 4s\ ^2S_{1/2} + 2e + \Delta E'' \tag{5.4}$$

where ΔE's are the appropriate energy differences. Here, rapid mixing of populations within the ^{3}P multiplet through buffer gas collisions is assumed. If ΔE is bigger than the thermal energy of the colliding particles, it may be bridged by a third body (electron or another atom).

7. Depopulation of state 2 through strong energy pooling collisions leading to direct population of state 5 and 6 is also included. Thus,

$$2 \times \text{Ca } 4s4p\ ^3P \Rightarrow \text{Ca } 4s^2\ ^1S_0 + \text{Ca } 4s4p\ ^1P_1 + \Delta E \tag{5.5}$$

$$2 \times \text{Ca } 4s4p\ ^3P \Rightarrow \text{Ca } 4s^2\ ^1S_0 + \text{Ca } 4s5s\ ^3S + \Delta E \tag{5.6}$$

In addition, energy pooling between an atom in state 2 and another atom in state 3 is also included thereby directly creating an atom in state 7 or 8. Thus,

$$\text{Ca } 4s4p\,^3P + \text{Ca } 4s3d\,^3D \Rightarrow \text{Ca } 4s^2\,^1S_0 + \text{Ca } 3d4p\,^3F + \Delta E \qquad (5.7)$$

$$\text{Ca } 4s4p\,^3P + \text{Ca } 4s3d\,^3D \Rightarrow \text{Ca } 4s^2\,^1S_0 + \text{Ca } 3d4p\,^1D_2 + \Delta E \qquad (5.8)$$

8. An arbitrary fraction of the thermionic electrons present in the thermionic diode [5, 95, 96] is used as "seed" electrons. These "seed" electrons gain energy in superelastic collisions with laser-excited atoms and subsequently transfer a substantial fraction from it to other excited atoms through inelastic collisions as noted earlier.

9. Depopulation of the states 3 and the "product" states is mainly through spontaneous radiative decay and hence the collisional deexcitation rates of these states are kept small.

10. The cross-sections for the associative ionization and Penning ionization are assumed to be very small.

11. Excitation of the buffer gas (Ar) atoms is not considered. This is consistent with our experimental results since spectral emission from Ar has not been recorded [6].

12. Convective diffusion of laser-excited atoms towards the optical windows is included through an exponential factor viz

$$N_2 = N_2 \exp\left(-\frac{t}{\tau_d}\right) \qquad (5.9)$$

where τ_d is the characteristic diffusion time of the order of 1 ms. This may be justified in the presence of moderate pressures of Ar which inhibit the convective diffusion through a chain of elastic collisions [3].

13. Since we are assuming our triplet state to be a singlet, the rate calculated is the total rate of transfer into the entire triplet manifold. However, experimentally we are calculating the rate to one particular state of the triplet manifold only. In order to make the two results mutually consistent, the rate calculated from the computer calculations must be multiplied by ratio fraction of the statistical weights. Furthermore, four transitions are originating from 4p3d $^3F_2$ and we have considered this factor through the branching ratios for the transitions originating from the $^3F_2$.

5.3 The Rate Equations

In order to study the dynamics of the atomic processes and to determine the relative contribution of each of the above processes a set of time-dependent differential equations representing the temporal behavior of the population density of an atomic level, the energy of free electron and the density of free electrons have been developed.

5.3.1 Instantaneous Population Densities of Excited States

After the initial preparation of the atomic population in a particular parent state, the instantaneous population of the excited state 'n' (density N_n) will change with time due to various collisional and radiative processes (some of which are mentioned before). The appropriate rate equation for its population density (N_n) may be written

as

$$\begin{aligned}\frac{dN_n}{dt} &= -N_n\left\{N_e\left[K_{nc}+\sum_m(1-\delta_{nm})K_{nm}\right]+\sum_{m<n}(\gamma A_{nm})\right\}\\ &+N_e\sum_m N_m(1-\delta_{nm})K_{nm}+\sum_{m<n}[N_m(\gamma A_{nm})]\\ &+N_eN^+\{\beta(n)+N_eK_{cn}\}+0.5N_2^2\{K_{ep1}(\delta_{6n}-2\delta_{2n}+\delta_{1n})\\ &+K_{ep4}(\delta_{5n}-2\delta_{2n}+\delta_{1n})\}+N_2N_3\{K_{ep2}(\delta_{7n}-\delta_{2n}-\delta_{3n}+\delta_{1n})\\ &+K_{ep3}(\delta_{8n}-\delta_{2n}-\delta_{3n}+\delta_{1n})\}+(1-2\delta_{nl})QN^{Ar}N_n \qquad (5.10)\end{aligned}$$

where

N_e is the electron density,

N^+ is the ion density,

δ is the Kronecker delta function,

K_{mn} is the rate coefficient for electron-atom collisional excitation or deexcitation between states m and n,

K_{ep1} is the rate coefficient of energy pooling collisions to state 6 (see Eq. 5.6),

K_{ep2} is the rate coefficient of energy pooling collisions to state 7 (see Eq. 5.7),

K_{ep3} is the rate coefficient of energy pooling collisions to state 8 (see Eq. 5.8),

K_{ep4} is the rate coefficient of energy pooling collisions to state 5 (see Eq. 5.5),

K_{nc} is the rate coefficient for the ionization of state n through electron collisions,

A_{nm} is the radiative transition probability for spontaneous decay of state n to state m,

$\beta(n)$ is the rate coefficient for radiative recombination into state n,

K_{cn} rate coefficients for three body recombination into state n,

γ is the Holstein escape factor,

Q is the rate constant for thermal collisions with Ar,

N^{Ar} is the density of Ar,

Note that the factor with K_{ep1} corrects for the double counting of the same atom.

5.3.2 Electron Density

Similarly the rate equation for electron density may be written as

$$\frac{dN_e}{dt} = N_e \sum_n \left\{ N_n K_{nc} - N^+ \left[\beta(n) + N_e K_{cn} \right] \right\} + \alpha N_e^{th} \tag{5.11}$$

where αN_e^{th} is the contribution from thermionic emission, while the first two terms represent collisional ionization and radiative recombination contributions.

5.3.3 Electron Energy

The rate of variation of electron energy is given by

$$\begin{aligned} \frac{d(N_e k T_e)}{dt} &= -N_e \{ \sum_n N_n \left[E_{nc} K_{nc} \sum_{m<n} (E_{nm} K_{nm}) \right] - \sum_{m>n} (N_m K_{mn} E_{mn}) \\ &\quad - N^+ N_e \sum (K_{cn} E_{cn}) \} + (2E_2 - E_5) K_{ep4} N_2^2 \end{aligned} \tag{5.12}$$

where

E_{nm} is the energy difference between the levels n and m.

E_{nc} is the ionization energy of a state n.

K is the boltzman constant.

T_e is the electron temperature.

5.3.4 Normalization

The normalization conditions are given by:

$$N_0 = \sum_n N_n + N^+ \tag{5.13}$$

and

$$N_e = \alpha N_e^{th} + N^+ \tag{5.14}$$

where N_0 is the vapor density of Ca.

The solution of these rate equations gives the time behavior of level populations, the free-electron energy and temperature as a function of time. The rate coefficient in these equations can be varied to account for the observed phenomena.

5.3.5 The Actual Rates Used

We have used Seaton's formulas for electron collisional excitation and deexcitation involving discrete states [97] as well as for the electron collisional ionization [98]. The rate coefficient K_{cn} for three-body recombination into state n is calculated from the corresponding rate K_{nc} for ionization from the state n through the Saha equation assuming detailed balance [37, 99]. Thus,

$$K_{cn} = \left[1.67 \times 10^{-22} \frac{g(n)}{g(2,1)} (kT_e)^{-1.5} \exp\left(\frac{E_{cn}}{kT_e}\right)\right] K_{nc} \tag{5.15}$$

where $g(n)$ and $g(2,1)$ are the statistical weights for the state n of the Ca atom and the ground state of Ca ion, respectively. However, we could not find a suitable mathematical formula giving the cross sections for energy pooling collisions even

though some theoretical studies were reported for alkali atoms [100, 101, 102, 103]. Instead, we used some numerical values judiciously selected from the range of experimental data on cross sections for Ca and other atoms reported in the literature [8, 37, 100, 101, 102, 103]. The variations in the rate of the energy pooling collisions with temperature are partly included through the variations in the relative velocities of the particles $v \propto (kT)^{0.5}$, and through their densities.

For other atomic processes considered here, e.g., radiative recombination, we have used modified formulas for hydrogen-like atoms [97]. However, in all cases, we have introduced a multiplicative weight factor in the rates for the collision processes as an adjustable parameter.

In order to appreciate the relation between the multiplicative weight factors and the relevant experimental parameters, we may see them as correction factors accounting for possible underestimates, for example, in particle (atomic, ionic or electron) densities, electron temperature, as well as possible differences between the real and the calculated rates.

5.4 Line Intensities

The population densities are subsequently converted into line intensities by means of the following equation

$$Intensity = N_n A_{nm} E_{nm} F(\lambda_n) Br_n G \tag{5.16}$$

where

$F(\lambda_n)$ is the response function.

Br_n is the branching ratio of the state n.

G includes the geometric factors such as solid angles, fluorescence collecting optics, monochromator field of view and response of detection electronics, but excluding the photomultiplier response.

It is difficult to obtain the absolute values of line intensities without a proper calibrating source which should cover the entire range of wavelengths of interest. However a measurement of relative intensities can also give meaningful results where factors like G can be eliminated.

Thus the ratio of intensities of fluorescence from any two states may be taken. These ratios can be compared to the ratio of the line intensities obtained experimentally to confirm the validity of the computer model.

As an example, the population densities "N" calculated by this computer model as a function of time are shown in Fig. 5.1. Actually Log N is plotted for the convenience of displaying the results on the same graph. Note that in the case of the ground state $4s^2\ {}^1S_0$, the population density is virtually constant for the entire 10 μs except for the short duration of Laser pulse from Laser 1. State 2 and 3 have small blips near 1 μs, since the population is transferred to higher states of Ca at this time when a pulse from Laser 2 arrives. However, the population reaches an almost steady value again.

The corresponding electron temperature T_e reaches a peak value near 1 μs after the laser pulse from Laser 1, corresponding to the arrival of laser pulse from Laser 2 as shown in Fig 5.2. This is due to the large super elastic transfer rate coefficient

considered. From that point onwards the electron temperature decreases only slowly since the energy exchange between electrons and excited atoms seems to be fairly balanced.

The electron density N_e, on the other hand, appears to rise sharply near 1 μs, but still remains quite low with a maximum of about 10^6 cm^{-3}. It then continues to rise due to collisional ionization though rather slowly. This is shown in Fig 5.3.

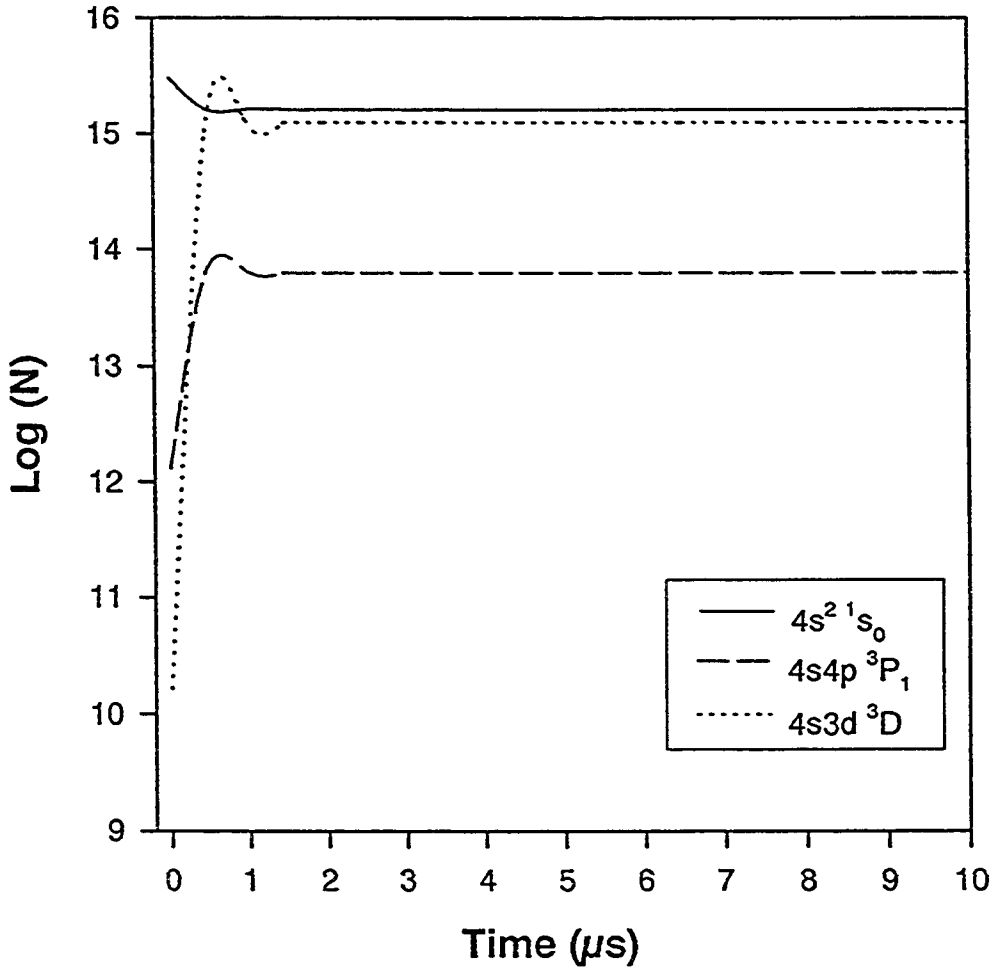

Figure 5.1: Variation of population density of selected states of Ca with time.

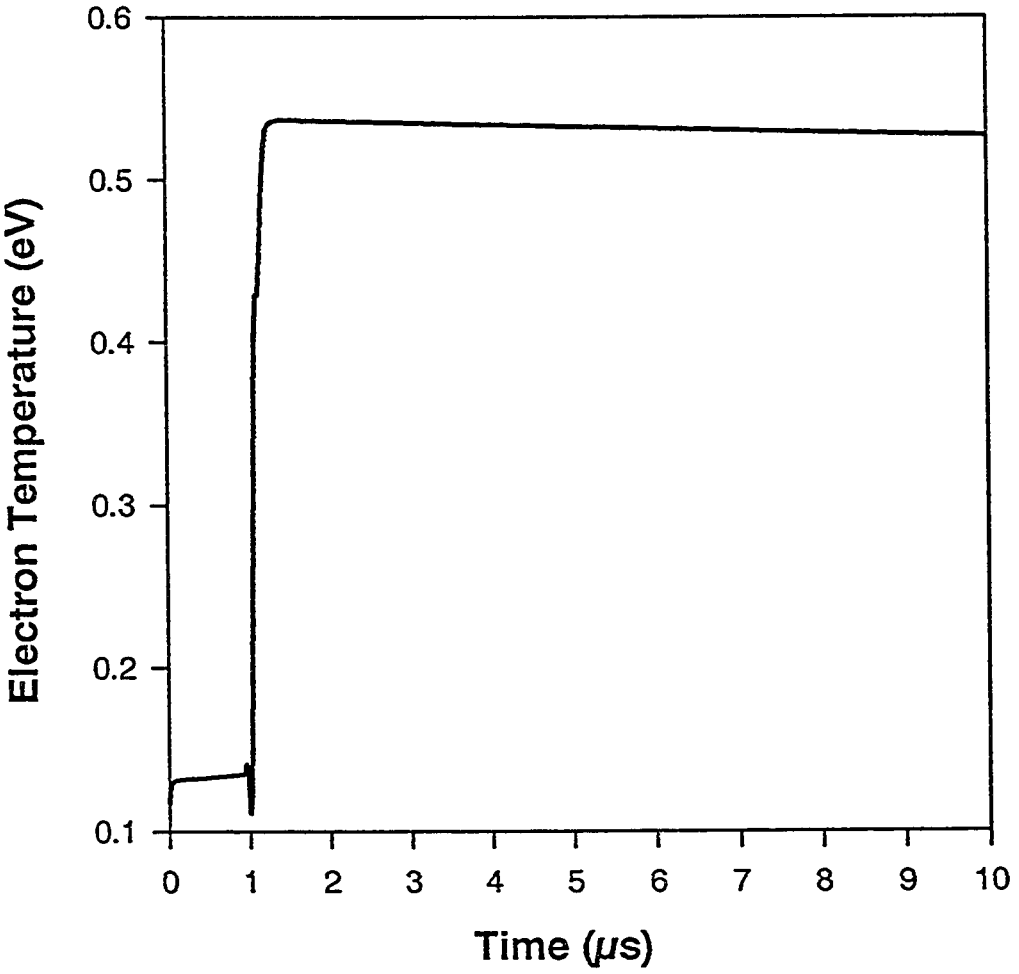

Figure 5.2: Variation of electron temperature with time.

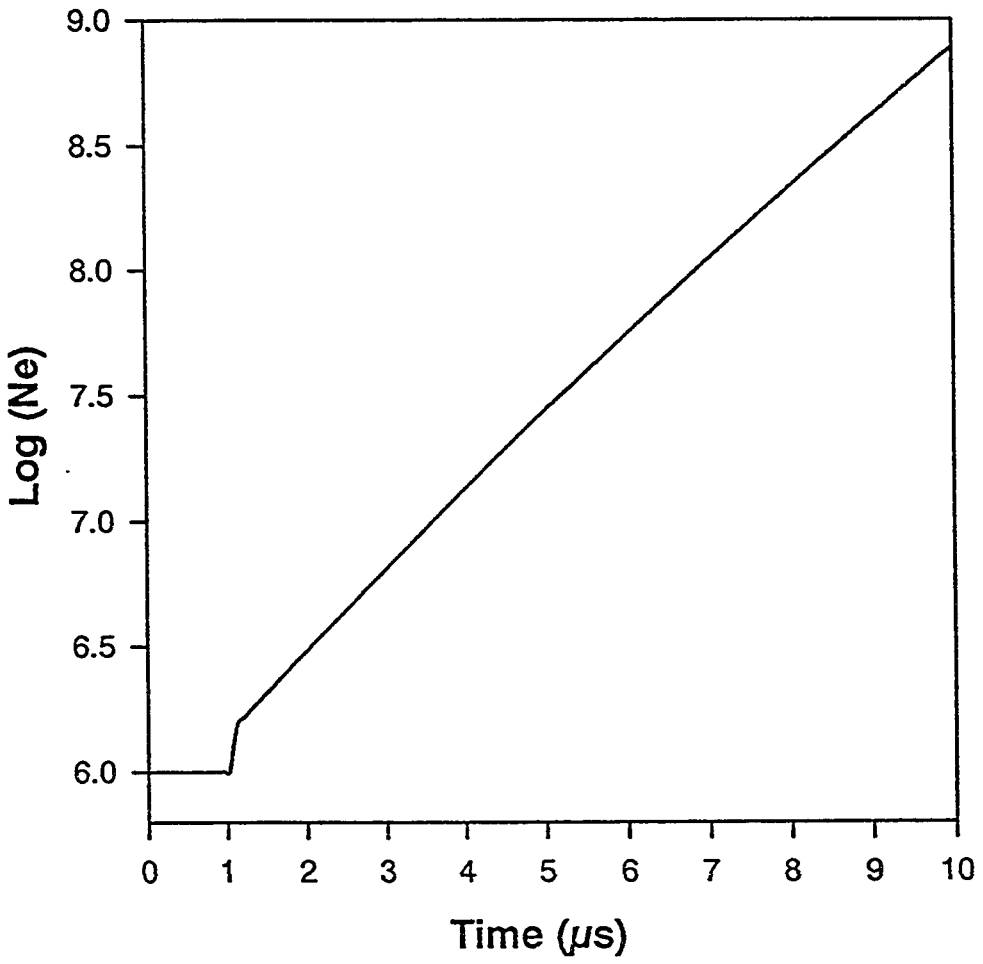

Figure 5.3: Variation of electron density with time.

5.5 Results on the Population Densities

5.5.1 Parent State 3d4p $^1D_2$

Figure 5.4 shows the variation of the population density with time of the parent state 3d4p $^1D_2$ and the three product states 4s5p ^3P, 3d4p ^3F, 4s5p $^1P_1$ for the first few μs. Note that near 1 μs i.e. upon the arrival of the 2nd laser pulse the population of the parent state jumps to a maximum. This is because the laser is resonant with the transition wavelength. Almost simultaneously the population of the parent state is transferred to the product states through thermal collisions with Ar depending on the appropriate rate coefficients. The populations of the product states clearly indicate this (Figure 5.4). Furthermore, the peaks for the product states are somewhat lower than that of the parent state as expected. This is quite reasonable, as the population is distributed among the three product states as indicated in Figure 2.2. The populations of these states subsequently drop quite rapidly, due to radiative decay and possibly also collisions. Note that collisions were neglected in the simple kinetic model discussed in chapter 2.

5.5.2 Parent State 3d4p ^3F

Figure 5.5 shows the variation of the population density with time for the parent state 3d4p ^3F and the three product states 4s5p ^3P, 3d4p $^1D_2$, 4s5p $^1P_1$. Here also we observe that near 1 μs the population of the parent state jumps to a maximum.The population of the parent state is transferred to the product states through thermal collisions with Ar depending on the appropriate rate coefficients. As in the previous case the peaks for the product states are somewhat lower than that of the parent state,

while populations of these states fall rapidly, due to radiative decay and collisions.

5.5.3 Parent State 4s5p ^{3}P

Variation of the population density with time of the parent state 4s5p ^{3}P is shown in Figure 5.6. Also shown are the populations for the three product states 3d4p $^1D_2$, 3d4p ^{3}F, 4s5p $^1P_1$. The peak of the ^{3}F state is comparable to that of the parent state itself as this state is quite rapidly populated through collisional transfer processes. Also the rate coefficient to this state is greater than the other two states. The peaks for the other product states 3d4p $^1D_2$ and 4s5p $^1P_1$, however, are lower than that of the parent state as expected. The populations of these states subsequently drop rapidly.

5.5.4 Parent State 3d4p ^{3}D

Variation of the population density with time of the parent state 3d4p ^{3}D is shown in Figure 5.7. The corresponding population of the three product states 4s4d ^{3}D, 4p^2 ^{3}P, 3d4p ^{3}P is also shown in the same figure. The peak of the ^{3}F state is comparable to that of the parent state itself as this state is quite rapidly populated through collisional transfer processes. Also the rate coefficient to this state is greater than the other two states. The peaks for the other product states 3d4p $^1D_2$ and 4s5p $^1P_1$ are therefore lower than that of the parent state as expected.

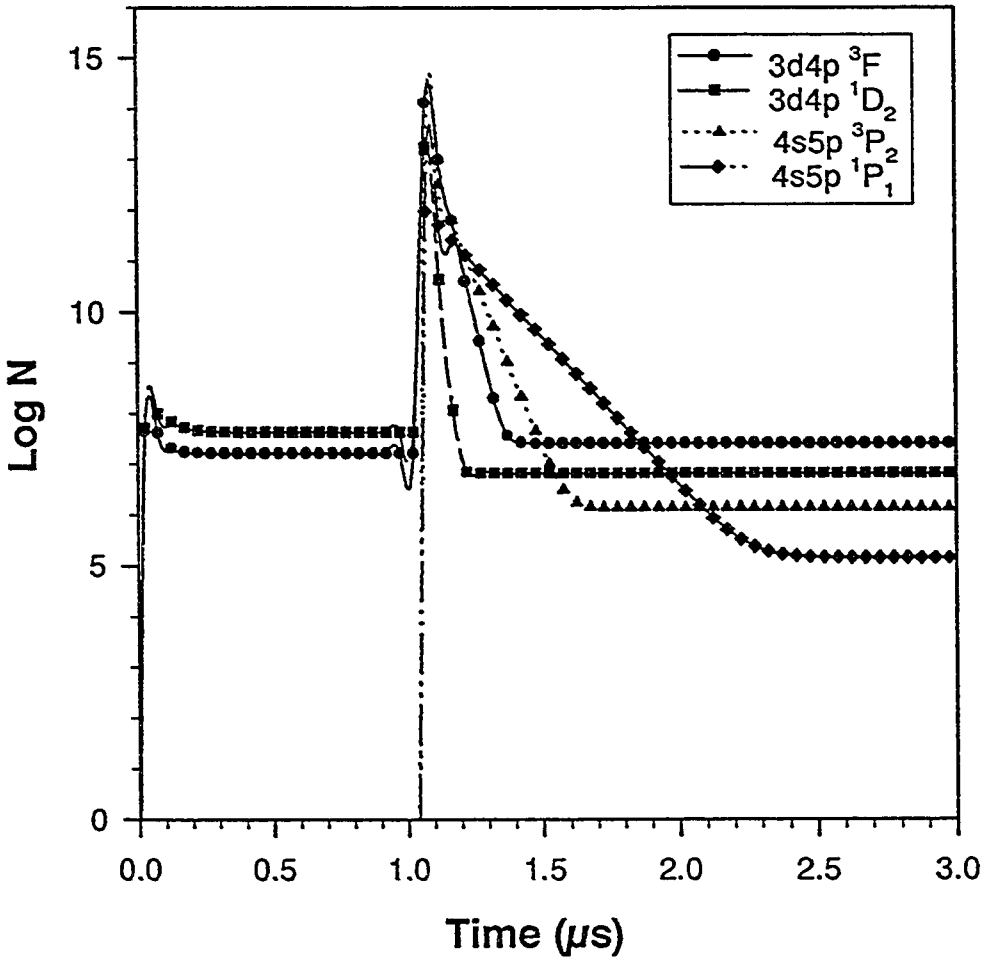

Figure 5.4: Variation of population density of some selected states (see the legend) of Ca with time. Here the parent state is the 3d4p $^1D_2$ state of Ca.

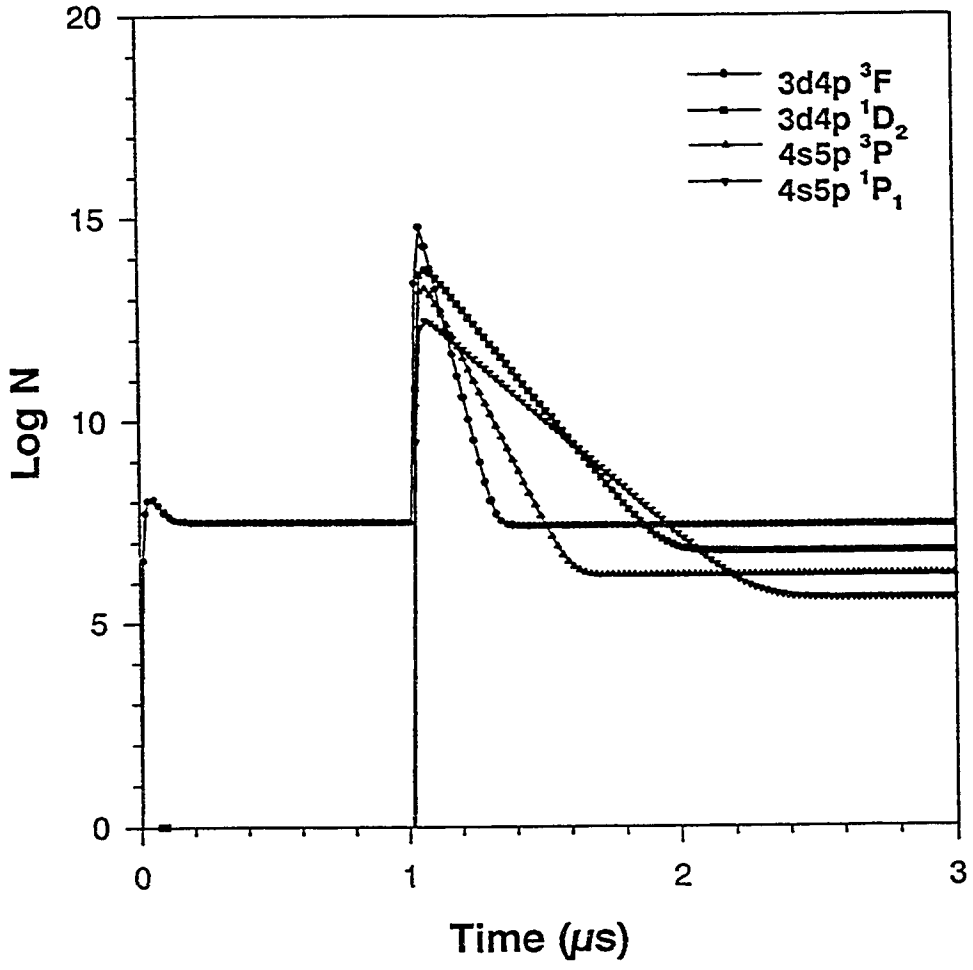

Figure 5.5: Variation of population density of some selected states of Ca with time. Here the parent state is the 3d4p ^{3}F state of Ca.

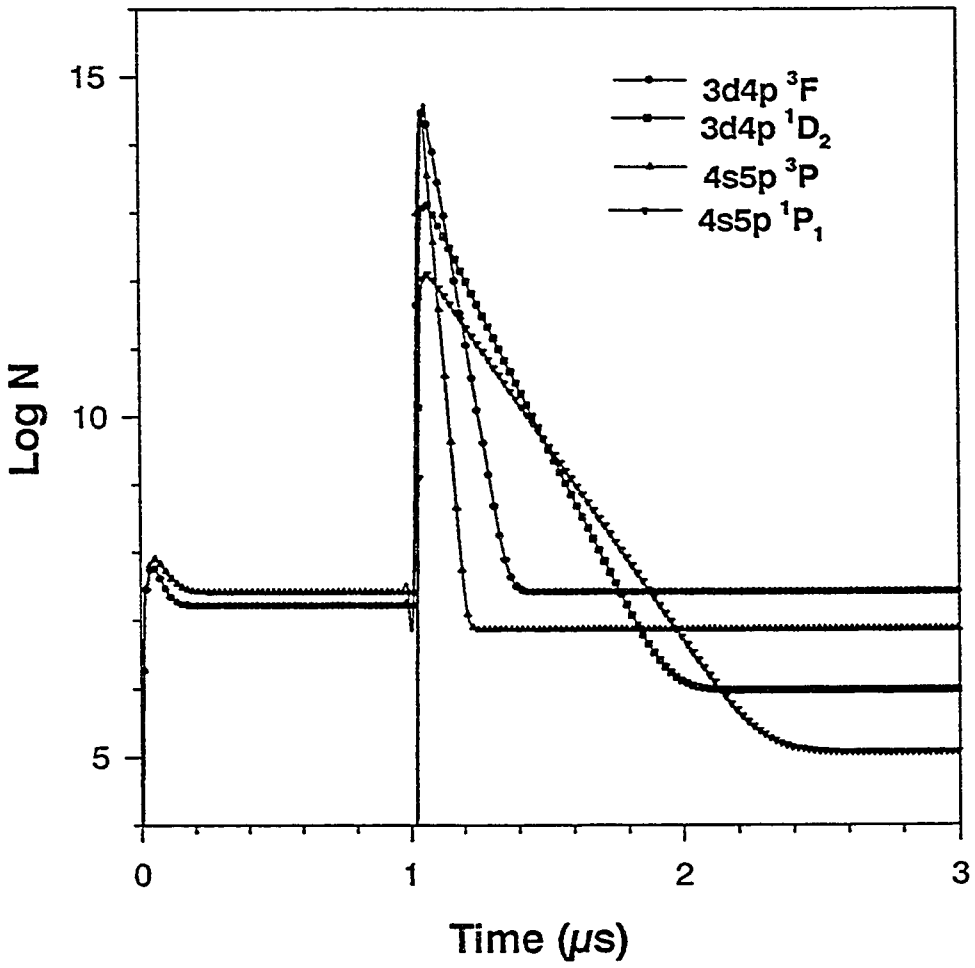

Figure 5.6: Variation of population density of some selected states of Ca with time. Here the parent state is the 4s5p ^{3}P state of Ca.

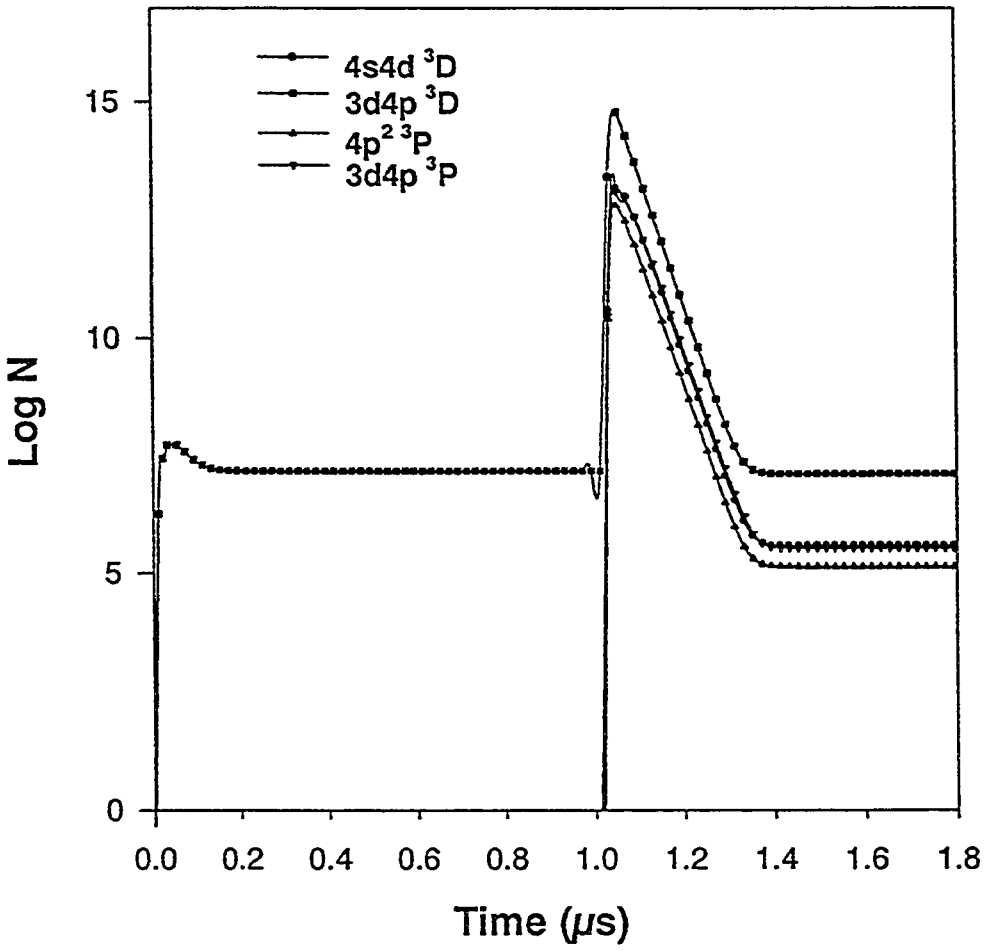

Figure 5.7: Variation of population density of some selected states of Ca with time. Here the parent state is the 3d4p ^{3}D state of Ca.

5.6 Results on Line Intensity Ratios and Calculation of Rate Constants

5.6.1 Parent State 3d4p $^1D_2$

Figure 5.8 and 5.9 have been obtained by converting the population densities discussed above (Figures 5.4, 5.5, 5.6 and 5.7) into line intensities with the help of equation 5.16. The area under each curve is then taken as the line intensity. The intensity ratios are then obtained for suitable line pairs and are subsequently compared with the experimentally obtained intensity ratios. The rates of collisional processes are adjusted through the weight factors to make the calculated values match the corresponding experimental data. Here, the rate coefficient for energy pooling collision (K_{ep2}) to state 7 had to be increased to $10^{-10}\ cm^3\,\mathrm{sec}^{-1}$ to get the required intensity ratios. The final results are shown in Table 5.2.

Transition	λ (Å)	Exp. Int. Ratios	Calculated Intensity Ratios	k_{1j} $cm^3\ s^{-1}$	Q
$3d4p\ ^3F_2 \rightarrow 4s3d\ ^1D_2$	7202 (ℓ_1)	-	-	14.81×10^{-11}	1.34
$4s5p\ ^3P_2 \rightarrow 4s3d\ ^3D_2$	6169 (ℓ_2)	0.811 $\left(\frac{\ell_1}{\ell_2}\right)$	0.816	2.373×10^{-11}	0.753
$4s5p\ ^1P_1 \rightarrow 4s3d\ ^1D_2$	6717 (ℓ_3)	5.58 $\left(\frac{\ell_1}{\ell_3}\right)$	5.56	0.74×10^{-11}	1.47

Table 5.2: Comparison of line intensity ratios obtained experimentally with those calculated by using the computer model. Parent state is the 3d4p $^1D_2$ state of Ca. Q is the multiplicative factor with k_{1j}.

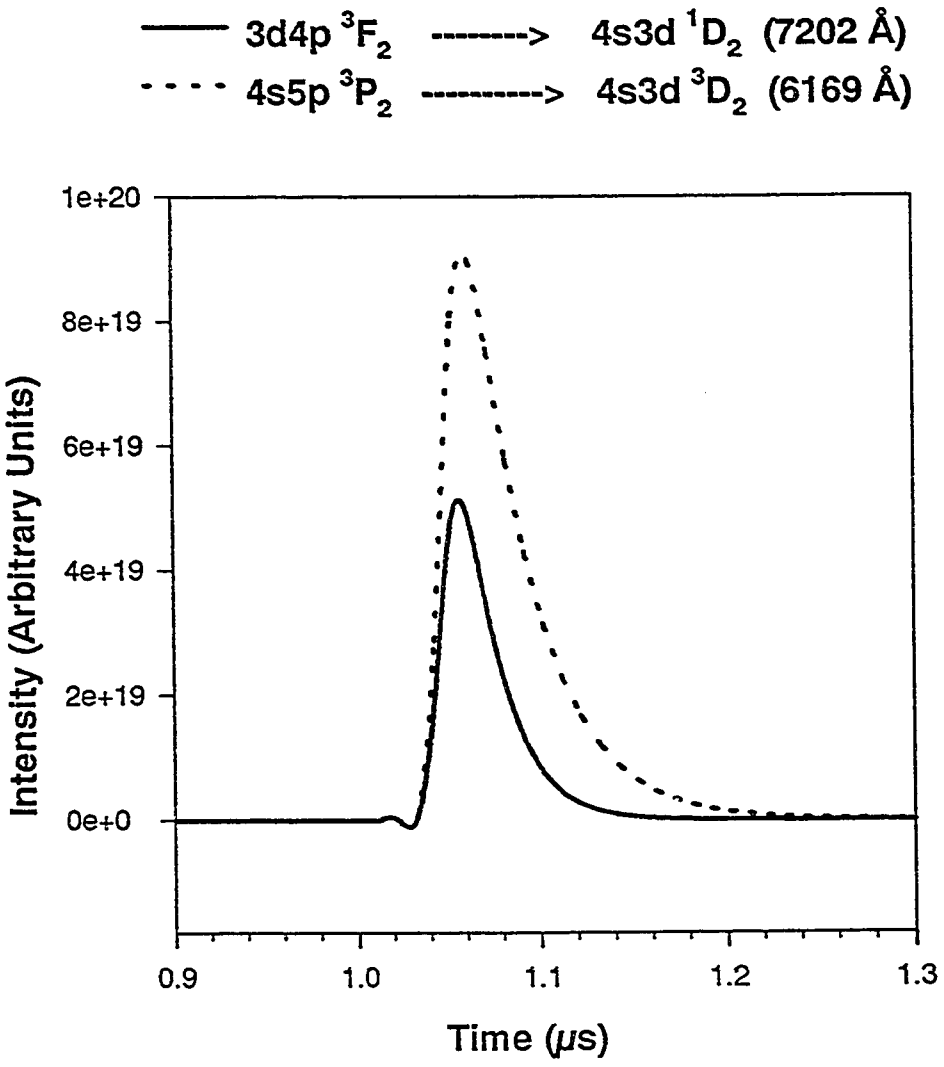

Figure 5.8: Computed line intensities of two transitions as obtained by the computer model. Parent state is 3d4p $^1D_2$.

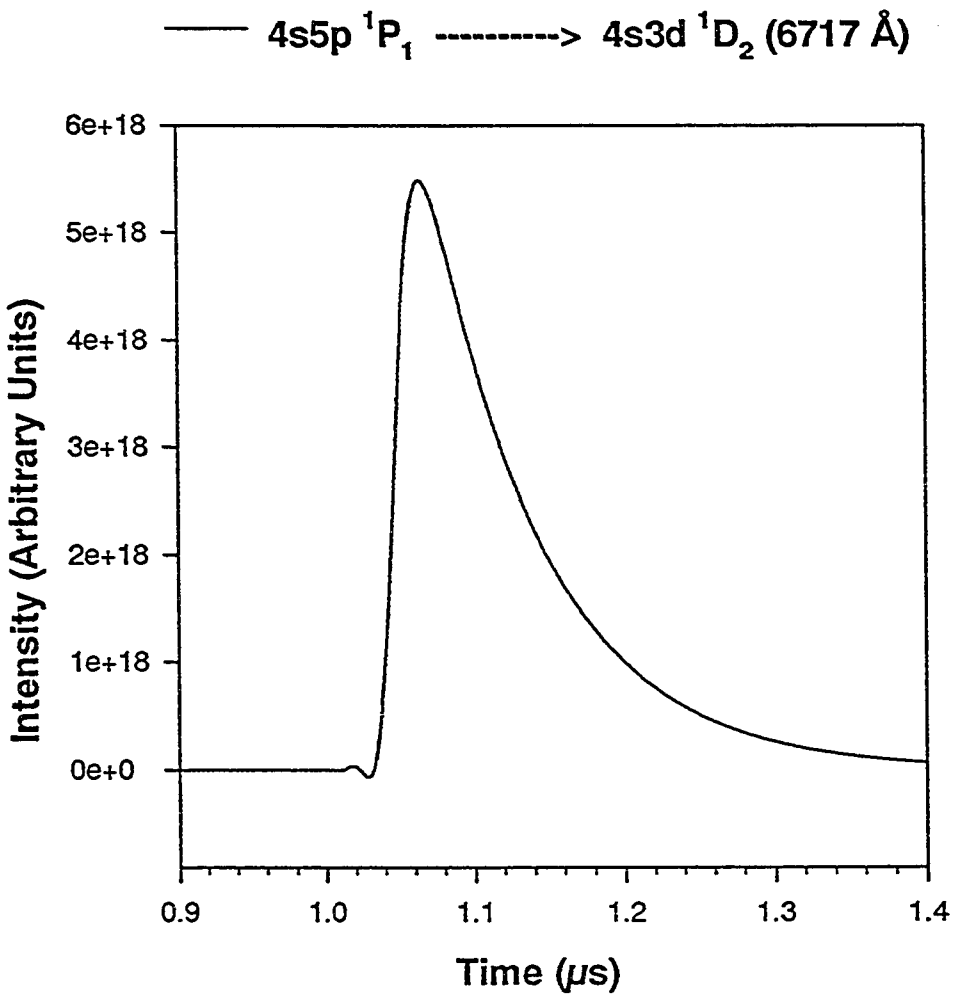

Figure 5.9: Computed line intensity of the transition as obtained by the computer model. Parent state is 3d4p $^1D_2$.

5.6.2 Parent State 4s5p ^{3}P

The line intensities obtained from the three selected calcium transitions,when the 4s5p ^{3}P parent state was prepared by the lasers are shown in Figure 5.10. The area under these curves is computed and the intensity ratios obtained are compared with the experimentally obtained intensity ratios. Here, the rate coefficient for energy pooling collision (K_{ep2}) to state 7 was again set at 10^{-10} $cm^3\,\mathrm{sec}^{-1}$. The results are displayed in Table 5.3.

Transition	λ (Å)	Exp. Int. Ratios	Calculated Intensity Ratios	k_{1j} $cm^3\ s^{-1}$	Q
$3d4p\ ^1D_2 \rightarrow 4s3d\ ^1D_2$	7148 (ℓ_1)	-	-	13.95×10^{-11}	1.8
$3d4p\ ^3F_2 \rightarrow 4s3d\ ^1D_2$	7202 (ℓ_2)	2.339 $\left(\frac{\ell_1}{\ell_2}\right)$	2.378	26.95×10^{-11}	0.557
$4s5p\ ^1P_1 \rightarrow 4s3d\ ^1D_2$	6717 (ℓ_3)	4.607 $\left(\frac{\ell_1}{\ell_3}\right)$	4.591	*2.5×10^{-11}	1.03

Table 5.3: Comparison of line intensity ratios obtained experimentally with those calculated by using the computer model. Parent state is the 4s5p ^{3}P state of Ca. Q is the multiplicative factor with k_{1j}. *Rate constant calculated via detailed balance using results of Hale and Leone (see Chap 4).

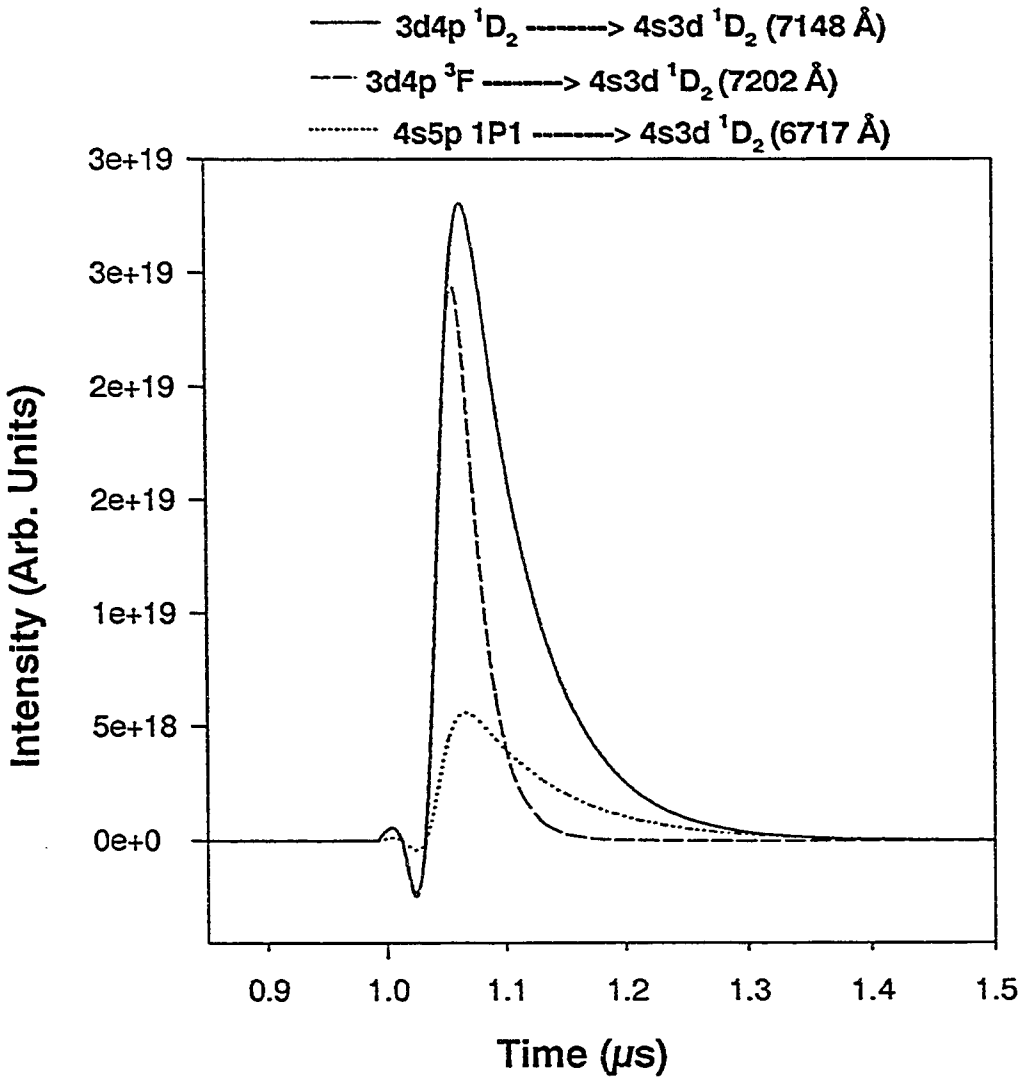

Figure 5.10: The computed line intensities of various transitions as obtained by the computer model. Parent state is the 4s5p ^3P state of Ca.

5.6.3 Parent State 3d4p ^{3}F

A similar procedure was followed for the line intensities obtained from the three calcium transitions indicated in Figure 5.11 when the 3d4p ^{3}F parent state was prepared by the lasers. We could not find suitable line pairs for calculating the population transfer rates, using the kinetic model of chapter 2. Here we had to rely on our computer model . Indeed we have sufficient confidence in our model in that it is quite reliable in predicting the level populations and line intensities etc. The rate coefficients from the parent state to the two product states 4s5p ^{3}P and 4s5p ^{1}P$_1$ have been calculated with the help of the computer model are shown in Table 5.4.

Transition	λ (Å)	Exp. Int. Ratios	Calculated Intensity Ratios	k_{1j} cm^3 s^{-1}	Q
$4s5p\ ^3P \rightarrow 4s3d\ ^3D$	6169 (ℓ_1)	-	-	3×10^{-11}	-
$3d4p\ ^1D_2 \rightarrow 4s3d\ ^1D_2$	7148 (ℓ_2)	2.23 $\left(\frac{\ell_1}{\ell_2}\right)$	2.25	4.29×10^{-11}	1.58
$4s5p\ ^1P_1 \rightarrow 4s3d\ ^1D_2$	6717 (ℓ_3)	17.7 $\left(\frac{\ell_1}{\ell_3}\right)$	17.72	0.33×10^{-11}	-

Table 5.4: Comparison of line intensity ratios obtained experimentally with those calculated by using the computer model. Parent state is the 3d4p ^{3}F state of Ca. Q is the multiplicative factor with k_{1j}.

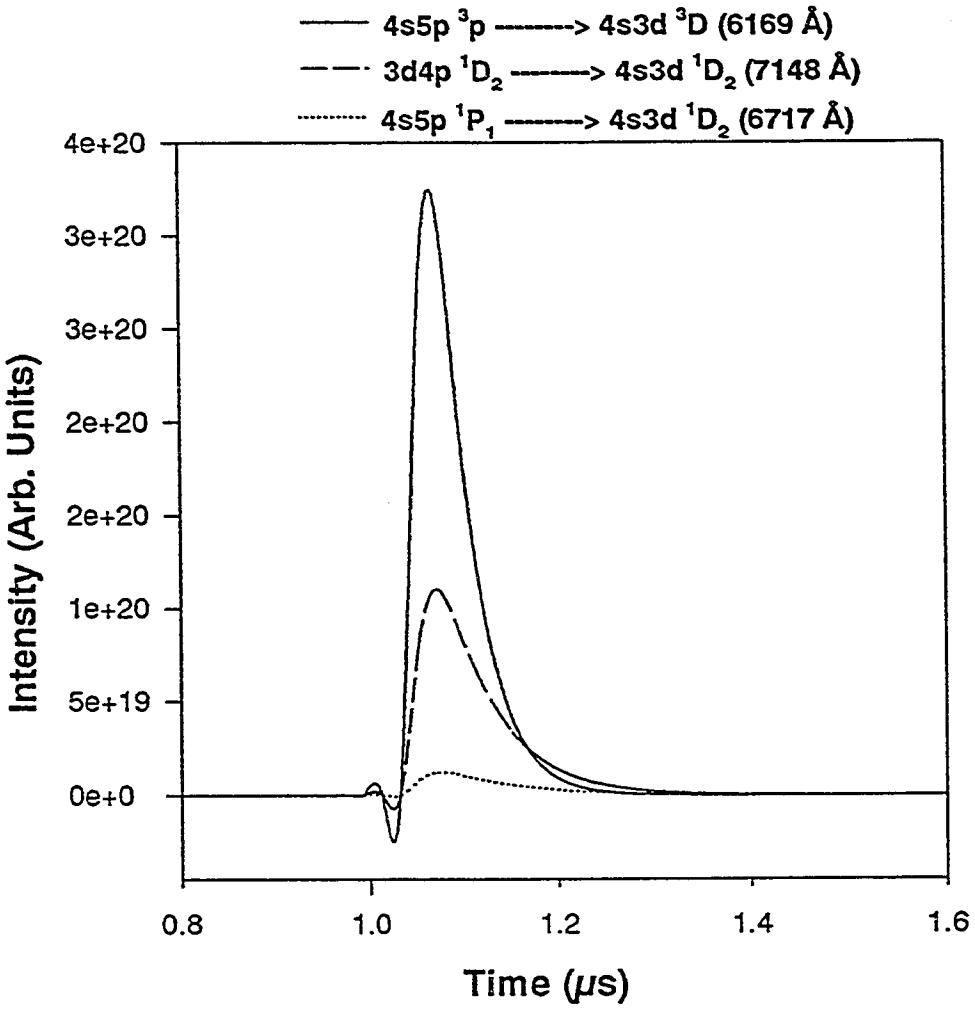

Figure 5.11: The computed line intensities of various transitions as obtained by the computer model. Parent state is the 3d4p ^{3}F state of Ca.

5.6.4 Parent State 3d4p ^{3}D

Likewise, the intensities of the three selected calcium transitions, when the 3d4p ^{3}D parent state was prepared are shown in Figure 5.12.The comparison between the intensity ratios obtained experimentally to that of the computed values are shown in Table 5.5. In this case also the rate coefficients from the 3d4p ^{3}D parent state to the three product states 4s4d ^{3}D, 3d4p ^{3}P and 4p^2 ^{3}P have been calculated with the help of the computer model as shown in Table 5.5.

Transition	λ (Å)	Exp. Int. Ratios	Calculated Intensity Ratios	k_{1j} cm^3 s^{-1}	Q
$4s4d\ ^3D \rightarrow 4s4p\ ^3P$	4454 (ℓ_1)	-	-	2.8×10^{-11}	-
$3d4p\ ^3P \rightarrow 4s3d\ ^3D$	5270 (ℓ_2)	2.14 $\left(\frac{\ell_1}{\ell_2}\right)$	2.00	2.1×10^{-11}	-
$4p^2\ ^3P \rightarrow 4s4p\ ^3P$	4302 (ℓ_3)	1.198 $\left(\frac{\ell_1}{\ell_3}\right)$	1.10	1.9×10^{-11}	-

Table 5.5: Comparison of line intensity ratios obtained experimentally with those calculated by using the computer model. Parent state is the 3d4p ^{3}D state of Ca. Q is the multiplicative factor with k_{1j}.

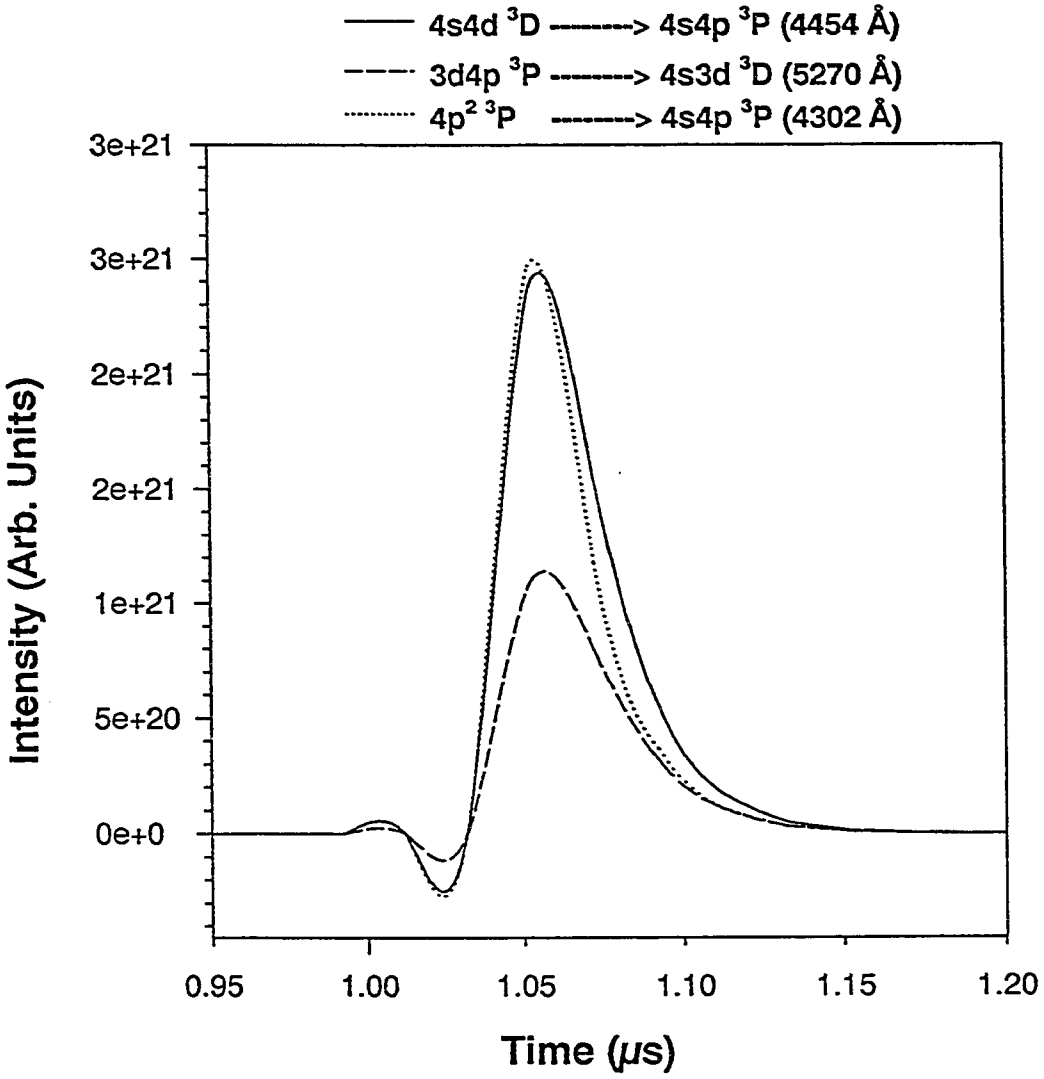

Figure 5.12: The computed line intensities of various transitions as obtained by the computer model. Parent state is the 3d4p ^{3}D state of Ca.

Chapter 6

Conclusion and Discussions

We have prepared several highly excited states of calcium, specifically the 3d4p ($^1D_2$, ^3F, ^3D), 4s5p ^3P and 4s5s ^3S states with the help of the resonant step-wise laser excitation method. Subsequently transfer of population to nearby states resulting from collisions with Ar was investigated through a systematic study of fluorescence from these nearby states. Then the corresponding state-to-state rate coefficients were determined. In the case of the 4s5s ^3S parent state however, we found that the rate of population transfer to nearby states was negligible. This is due to the large energy defect between this state and the nearby product states (see Table 4.1). In the case of 3d4p $^1D_2$ parent state, the collisional population transfer to nearby states (4s5p ^3P, 3d4p ^3F, 4s5p $^1P_1$) have been recorded with the help of a series of systematic time-resolved and spectrally-resolved fluorescence measurements. Utilizing these signals and the data published on Einsteins A coefficients, total radiative rates etc., we were able to calculate the rate-constants by using the simple kinetic model scheme discussed inside chapter 2. The same technique was used to calculate rate coefficient from the other parent states (3d4p ^3F, 3d4p ^3D and 4s5p ^3P) to the nearby product states. Similar measurements on different other states of Ca as well as other atoms

were performed in previous publications [20, 21, 22] on the rate coefficients, and the results on the state-to-state rate constants and total quenching rates agree well with those calculated in this thesis.

A more detailed time-dependent computer model was developed to investigate the population transfer through thermal collisions with Ar. The instantaneous populations were calculated and the intensities of fluorescence from transitions of interest were mapped out. These instantaneous populations were converted into line intensities with the help of equation 5.16. The ratios of these time integrated intensities for some line pairs were calculated and compared with those observed experimentally. The appropriate rates were adjusted to obtain the same intensity ratios as observed experimentally. The rate constants thus calculated were subsequently compared with the experimentally derived information. The zero-density intercepts of the linear back-extrapolated rate constants were derived from the simple kinetic model. These are cross-checked with the values K_{1i} predicted by the detailed computer model and agree within a factor of 2. Here, we have to keep in mind that the principal limitations on the detailed time-dependent computer model are the rates used for other processes such as electron collision processes, ionization and recombination. However, looking at the quality of agreement, we can say that our rate constant data give a reasonably good estimate of the true state-to-state rate constants, K_{1i}.

Some additional rate coefficients which could not be derived by experimental means, were calculated with the help of the computer model as was outlined in chapter 5. This was based on our confidence in the computer model in that it provided a reasonably realistic description of the physical processes occuring in the Ca vapor.

6.1 Some Suggestions for Future Work

In the computer model we assumed our triplet state to be a singlet state. We could modify it to include each state individually and indeed some other states also which were not considered before. In this way we can accurately predict the rates for thermal collisions with argon atoms for these states. On the experimental side, using some other dyes, data on many other states could also be obtained.

Bibliography

[1] J. Coutts, S. K. Peck, and J. Cooper. *J. Appl. Phys.*, 64(3):977–981, 1988.

[2] M. A. Khan, M. A. Gondal, and M. H. Rais. *Appl. Phys. B*, 57:123–130, 1993.

[3] M. A. Khan, E E Khwaja, and M. F. Al-Kuhaili. *J. Phys. D: Appl. Phys.*, 26:1614–1621, 1993.

[4] M. A. Khan and E E Khawaja. *Optics Communications*, 86:386–392, 1991.

[5] M. A. Khan, E E Khwaja, and H. A. Al-Juwair. *At. Mol. Opt. Phys*, 23:L533–L539, 1990.

[6] M. A. Khan, M. A. Gondal, and M. H. Rais. *Appl. Phys. B.*, 61:391–399, 1995.

[7] M. A. Khan, M. A. Gondal, and M. H. Rais. *J. Phys. B*, 28:845–857, 1995.

[8] M. A. Khan, M. A. Gondal, and M. H. Rais. *J. Phys. B*, 27:2889–2904, 1994.

[9] M. A. Gondal, M. A. Khan, and M. H. Rais. *Il Nuovo Cimento*, 17D(1):9–16, 1995.

[10] M. A. Gondal, M. A. Khan, and M. H. Rais. *Plasma Sources Sci. Technol.*, 4:137–141, 1995.

[11] M. A. Gondal, M. A. Khan, and M. H. Rais. *Chemical Physics Letters*, 243:94–101, 1995.

[12] R. A. J. Borg, E. R. Waclawik, and W. D. Lawrence. *Chem. Phys. Lett.*, 199:320–324, 1992.

[13] N. Bras and J. C. Jeannet. *J. Chem. Phys.*, 101(9):7531–7537, 1994.

[14] B. Dubreuil. *Physical Review A*, 27:2479–2484, 1983.

[15] C. Gabbanini, A Lucchesini, and S Gozzini. *J. Phys. B: At. Mol. Opt. Phys.*, 27:4643–4651, 1994.

[16] B. Dubreuil and C. Chaleard. *Physical Review A*, 29(2):958–961, 1984.

[17] Breckenridge W H and Merrow C N. *J. Chem. Phys.*, 88:2320–8, 1988.

[18] Y. C. Chan and J. A. Gelbwachs. *Chem. Phys. Lett.*, 178:523–7, 1991.

[19] Wright J J and Balling L C. *J. Chem. Phys.*, 73:1617–9, 1980.

[20] J. E. Smedley, D. F. Marran, M. R. Peabody, and C. N. Marquis. *J. Chem. Phys.*, 98(2):1093–1100, 1993.

[21] J. E. Smedley and D. F. Marran. *Physical Review A*, 47 (1):126–131, 1993.

[22] Michael O. Hale and Stephen R. Leone. *J. Chem. Phys.*, 79(7):3353–3362, 1983.

[23] M. O. Hale and S. R. Leone. *Phys. Rev. A*, 31(1):103–112, 1985.

[24] R. W. Schwenz and Stephen R. Leone. *Chem. Phys. letters*, 133 (5):433–439, 1987.

[25] M. A. Khan and M. Rafique. *Applied Physics B*, 61:559–568, 1995.

[26] Jing-Yuan Zhang, Hai-Tian Zhou, Qiong-Ru Li, Jian Yang, Li-Zeng Zhao, and Yu-Xin Nie. *J. Phys. B*, 21:589–602, 1988.

[27] N. Omenetto, T. Berthoud, P. Cavalli, and G. Rossi. *Appl. Phys. B*, 39:500–503, 1985.

[28] I. I. Vlasov and N. V. Chekalin. *Spechtrochimica Acta*, 48B:597–603, 1993.

[29] O. Axner, P. Ljungberg, and Y. Malmsten. *Appl. Phys. B*, 54:144–155, 1992.

[30] J. A. Armstrong, P. Esherick, and J. J. Wynne. *Phys. Rev. A*, 15(1):180–196, 1977.

[31] C. Brechignac, Ph. Cahuzac, and A. Debarre. *Phys. Rev. A*, 31(5):2950–2956, 1985.

[32] Bingying Cheng, Zhaolin Li, Yongwu Yang, Junkong Zhu, and Daozhong Zhang. *Optics Communications*, 86:465–468, 1991.

[33] H. G. Kuhn. *Atomic Spectra*, page 308. Academic Press Inc., second edition, 1969.

[34] R. Okasaka and K. Fakuda. *J. Phys. B*, 15:357–370, 1982.

[35] L. Krause. *Adv. Chem. Phys.*, 28:267–316, 1982.

[36] W. H. Breckenridge and Umemoto. *Adv. Chem. Phys.*, 50:325, 1982.

[37] A. Kallenbach and M. Kock. *J. Phys. B*, 22:1705–1720, 1989.

[38] I. Jackowska and Lukaszewski. *J. Phys. B*, 23:2097–2104, 1990.

[39] C. H. Greene and M. Aymar. *Phys. Rev. A*, 44(3):1773–1790, 1991.

[40] A. Kumarakrishan and X. L. Han. *Optics Communication*, 109:348–360, 1994.

[41] K. S. Bhatia. *Can. J. Phys.*, 65:379–381, 1987.

[42] Charles W Bauschlicher, Stephen R Langhoff, and Harry Partridge. *J. Phys. B*, 18:1523–1532, 1985.

[43] R. N. Gosselin, E. H. Pinnington, and W. Ansbacher. *Phys. Rev. A*, 38(9:4887–4889, 1988.

[44] G. V. Zhuvikin, N. P. Penkin, and L. N. Shabanova. *Opt. Spectrosc. (USSR)*, 58(6):750–755, 1985.

[45] K. Ueda and K. Fakuda. *J. Phys. Chem.*, 86:678–681, 1982.

[46] Kiyoshi Ueda, Yasuo Ashizawa, and Kuniya Fukuda. *Journal of Physical Society of Japan*, 50(2):623–631, 1981.

[47] Kiyoshi Ueda, Takashi Fujimoto, and Kuniya Fukuda. *J. Phys. Soc. Japan*, 48(1):343–344, 1980.

[48] Bethe, H. A., and Salpeter. *E. E. Quantum Mechanics of One- and Two-electron Atoms.* Springer-Verlag, 1957.

[49] Phelps, A. V., and McCoubry. *A. O. Phys. Rev.*, 118:1561, 1960.

[50] Lei Xu, You-Yuan Zhao, Guo-Yi Wang, Mao-Qi He, and Zhao-Yong Wang. *J. Opt. Soc. Am. B*, 9(7):1017–1019, 1992.

[51] Holstein. *T. Phys. Rev.*, 83:1159, 1951.

[52] Holstein. *T. Phys. Rev.*, 72:1212, 1947.

[53] J. B. Hasted. *Physics of Atomic Collisions*, pages 659–691. Butterworth and Co., second edition, 1972.

[54] K K Rohatgi-Mukherjee. *Fundamentals of Photochemistry*, pages 165–179. Wiley Eastern Limited, revised edition, 1986.

[55] Harvey Elliott White. *Introduction to Atomic Spectra*, pages 171–183. McGraw-Hill Book Company, Inc., 1934.

[56] M. A. Lesnoi. *Sov. J. Quantum Electron.*, 18(7):876–878, 1988.

[57] B. Gellert. *J. Phys. D*, 21:710–717, 1988.

[58] I. S. Zeilikovich, S. A. Pulkin, and L. S. Gaida. *Sov. J. Quantum Electron.*, 18(2):164–166, 1988.

[59] M. A. Bouchiat, J. Guena, Ph. Jacquier, and M. Lintz. *Z. Phys. D*, 24:335–337, 1992.

[60] H. M. Pask and J. A. Piper. *IEEE Journal of Quantum Electronics*, 29(9):2540–2546, 1993.

[61] R. J. Malins, A. David Logan, and D. J. Benard. *Chem. Phys. Lett.*, 83(3):605–609, 1981.

[62] Orazio Svelto. *Principles of Lasers*, pages 287–371. Plenum Press, New York and London, third edition, 1989.

[63] Franck. *J. Z. Phys.*, 9:259, 1922.

[64] Cario. *Z. Phys.*, 10:185, 1922.

[65] Cario, G., and Franck. *Z. Phys.*, 17:202, 1923.

[66] A. A. Isaev, V. V. Kazakov, M. A. Lesnoi, S. V. Markova, and G. G. Petrash. *Sov. J. Quantum Electron.*, 16(11):1517–1522, 1986.

[67] A. A. Isaev, G. G. Petrash, and I. V. Ponomarev. *Sov. J. Quantum Electron.*, 16(11):1512–1516, 1986.

[68] D.A. Miller, L. You, J. Cooper, and A. Gallagher. *Phys. Rev. A*, 46(3):1303–1309, 1992.

[69] J. F. Kelly, M. Harris, and A. Gallagher. *Phys. Rev. A*, 37(7):2354–2360, 1988.

[70] W. J. Alford. *J. Chem. Phys.*, 96(6):4330–4340, 1992.

[71] Ch. K. Rhodes, editor. *Excimer Lasers*, pages 87–133. Springer-Verlag, second edition, 1984.

[72] J. Tellinghuisen, J. M. Hoffman, and G. C. Tisone. *J. Chem. Phys.*, 64(6):2484–2490, 1976.

[73] J. E. Velazco, J. H. Kolts, and D. W. Setser. *J. Chem. Phys.*, 65(9):3468–3480, 1976.

[74] G. E. Caledonia. *Chem. Rev.*, 75(3):333–351, 1975.

[75] L. G. Christophorou. *Atomic and molecular Radiation Physics*, pages 63–146. Wiley and Sons, London, 1971.

[76] J. D. Daugherty, J. A. Mangano, and J. H. Jacob. *Appl. Phys. Lett.*, 28(10):581–583, 1976.

[77] M. A. Khan, M. A. Gondal, and M. H. Rais. *Optics and Laser Technology*, 27:379–382, 1995.

[78] M. Harris, D.R. McHugh, E.L. Lewis, I. Shannon, and M. Zakai. *J. Phys. B*, 20:5575–5583, 1987.

[79] D. Husain and G. Roberts. *J. Chem. Soc. Faraday Trans.*, II 82:1921, 1986.

[80] J. F. Kelley, M. Harris, and A. Gallagher. *Phys. Rev. A*, 38(3):1225–1229, 1988.

[81] H. G. Werij, M. Harris, J. Cooper, A. Gallagher, and J.F. Kelly. *Phys. Rev. A*, 43(5):2237–2249, 1991.

[82] N. Bras, J. C. Jeannet, and D. Perrin. *J. Phys. B*, 26:2289–2302, 1993.

[83] P. Bicchi, C. Marinelli, E. Mariotti, M. Meucci, and L. Moi. *J. Phys. B*, 26:2335–2344, 1993.

[84] F. Roussel, B. Carre, P. Berger, and G. Speiss. *J. Phys. B*, 16:1749–1765, 1983.

[85] S. Majetich, E.M. Boczar, and J.R. Wiesenfeld. *J. Appl. Phys.*, 66(2):475–481, 1989.

[86] J. H. Goble, W.E. Hollingsworth, and J. Winn. *Phys. Rev. Lett.*, 47:1881, 1981.

[87] L. Barbier and M. Cheret. *J. Phys. B*, 20:1229–1248, 1987.

[88] R.J. Malins and D.J. Benard. *Chem. Phys. Lett.*, 74:321, 1980.

[89] J. Sugar and C. Corliss. *J. Phys. Chem. Ref. Data*, 14 (Suppl. 2):51–56, 1985.

[90] W. E. Wiese, M. W. Smith, and B. M. Miles. *Atomic Transition probabilities*, volume II, pages 245–255. NSRDS - NBS22 (Washington,DC: US Government Printing Office).

[91] G. Smith and D. St. J. Raggett. *J. Phys. B*, 14:4015–4024, 1981.

[92] P. Hafner and W.H.E. Schwarz. *J. Phys. B*, 11:2975–2999, 1978.

[93] J. Coutts, S. K. Peck, R. Stoner, and J. Cooper. *J. Appl. Phys.*, 62(9):3514–3521, 1987.

[94] M. A. Khan, J. P. Connerade, and M. Rafique. *J. Phys. B*, 27:L563–L569, 1994.

[95] E. E. Khwaja, M. A. Khan, and H. A. Al-Juwair. *Int. J. Electronic*, 71:991–996, 1991.

[96] K. Niemax. *Appl. Phys. B*, 38:147, 1985.

[97] R. C. Elton. In H. R. Griem and R. H. Lovberg, editors, *Methods of Experimental Physics*, volume 9. Academic, New York, 1969.

[98] M. J. Seaton. In D. R. Bates, editor, *Atomic and Molecular Processes*. Academic, New York, 1962.

[99] D. L. Book. In H. L. Anderson, editor, *Physics Vade Mecum*. AIP, New York, 2nd edition, 1989.

[100] P. Kowalczyk. *J. Phys. B*, 17:817, 1984.

[101] V. M. Borodin and I. M. Komorov. *Opt. Spectrosc.*, 36:145, 1974.

[102] L. Barbier and M. Cheret. *J. Phys. B*, 16:3213, 1983.

[103] J. H. Nijland, J. A. De Gouw, H. A. Dijkerman, and H. G. M. Heideman. *J. Phys. B*, 25:2841, 1992.